

Contents lists available at ScienceDirect

# Journal of Computational Physics

journal homepage: www.elsevier.com/locate/jcp





# A robust compact finite difference framework for simulations of compressible turbulent flows

Hang Song <sup>a,\*</sup>, Aditya S. Ghate <sup>b</sup>, Kristen V. Matsuno <sup>a,c</sup>, Jacob R. West <sup>a</sup>, Akshay Subramaniam <sup>b</sup>, Sanjiva K. Lele <sup>a,b</sup>

- <sup>a</sup> Department of Mechanical Engineering, Stanford University, Stanford, CA, 94305, USA
- b Department of Aeronautics & Astronautics, Stanford University, Stanford, CA, 94305, USA
- <sup>c</sup> Systems Analysis Office, NASA Ames Research Center, Moffett Field, CA, 94035, USA

#### ARTICLE INFO

# Keywords: Compact finite difference Curvilinear meshes Compressible flows Direct numerical simulations Large-eddy simulations Robustness to aliasing errors

#### ABSTRACT

A robust high-order compact finite difference framework is proposed for simulations of compressible turbulent flows with high spectral resolution using a fully collocated variable storage paradigm. Both inviscid and viscous fluxes are assembled at the edge-staggered grid locations. Nonlinear robustness is attained as a consequence of the intrinsic reduction of aliasing errors in the inviscid fluxes due to the spectral behavior of the compact interpolation schemes. Additional robustness is provided by enhancing the spectral resolution of the viscous flux and its divergence at small scales using purely staggered numerical differentiation. Demonstrative simulations have shown numerical stability of the compact finite difference discretization without any type of solution filtering on both Cartesian and curvilinear meshes. For simulations on a curvilinear mesh, a general metric evaluation approach that satisfies the geometric conservation law is proposed. Additional approaches to combining the proposed scheme with approximate Riemann solvers and artificial diffusivities for shock-capturing are also discussed. Along with theoretical analysis, rigorous evaluation and validation of the methodology on canonical tests, including classic two-dimensional simulations, direct numerical simulations, and large-eddy simulations, are used to confirm robustness and accuracy.

#### 1. Introduction

High-order numerical schemes are an economical strategy used in conducting high-resolution numerical simulations of turbulent flows. They are widely applied for their rapid grid convergence accompanied by an affordable increase in computational cost. In turbulent flows, the structure of turbulent eddies spans a wide range of length scales. Additionally, in compressible flows, the thermodynamic behavior of a fluid is strongly coupled with the flow. As a result, acoustic waves [1], shocks [2] and eddy shocklets [3], and fluctuations of transport properties [4,5] commonly exist as flow features. Such wave structures need to be resolved or captured while maintaining the spatio-temporal accuracy of turbulent vortical structures at various scales and enforcing numerical conservation. Meanwhile, due to the energy cascade in turbulent flows, the turbulent kinetic energy is transferred from large scales to smaller and smaller scales successively until it is dissipated by molecular viscosity at the Kolmogorov length scale,  $\eta$ . The Kolmogorov length

https://doi.org/10.1016/j.jcp.2024.113419

Received 6 February 2024; Received in revised form 25 July 2024; Accepted 5 September 2024

<sup>\*</sup> Corresponding author.

E-mail address: songhang@stanford.edu (H. Song).

scale is known as the smallest length scale of turbulent eddies [6]. For direct numerical simulations (DNS), the Kolmogorov length scale is fully resolved by the computational mesh. However, considering computational cost, the Kolmogorov length scale is often set close to the limit of the mesh resolution,  $k_{\text{max}} \eta \sim \mathcal{O}(1)$  [7,8], where  $k_{\text{max}}$  is the maximum wavenumber supported by the computational mesh. For inhomogeneous turbulent flows, local mesh refinement or mesh stretching may be required to adapt to the local Kolmogorov length scale and, for wall-bounded turbulence in particular, the viscous length scale imposed by the wall [9–11]. In large-eddy simulations (LES), the mesh resolution is usually configured within the inertial subrange where the local turbulent motion shows statistically universal behavior and can be modeled. The solution of an LES is interpreted as a set of filtered quantities that resolves the large turbulent eddies carrying most of the turbulent kinetic energy. The residual effects beyond the mesh-supported resolution are represented by a subgrid-scale (SGS) model. Due to the nature of turbulence, the SGS model imposes mesh-adaptive dissipation, and many popular SGS models are formulated as eddy viscosity models [12–15] based on the Boussinesq approximation [16]. Both viscous dissipation and SGS model dissipation are predominately associated with the most finely resolved flow structures.

Capturing or resolving features at small scales requires numerical schemes to have satisfactory spectral behavior in addition to high-order grid convergence. Spectral methods and pseudo-spectral methods are widely used in computational fluid dynamics [17]. For an infinitely differentiable profile, the spectral representation converges faster than any power of the grid size [18]. The numerical errors are mainly ascribed to the Gibbs phenomenon for an insufficiently smooth profile and potential aliased interactions in nonlinear operations. Alternatively, compact finite difference methods [19] provide a more flexible approach to addressing complexities in boundary conditions and can be applied in combination with a variety of numerical schemes such as shock-capturing schemes. Compact numerical schemes are implicitly formulated to access more information across the entire domain. As a result, the leading-order truncation error is much smaller than that of explicit schemes [19]. Compact finite difference methods have demonstrated remarkable successes in DNS and LES of incompressible and compressible turbulent flows [8,20–22], computational aeroacoustics [1,23], and simulations of multiphysics flows and nonlinear wave propagation [24,25].

Preserving numerical stability while maintaining high-order accuracy and spectral resolution has become a major challenge in simulating compressible turbulent flows. One of the primary contributors to numerical instability is the aliasing error. The dynamics of compressible turbulence are highly nonlinear over a broad-band spectrum. Given a finite grid resolution, the nonlinear interactions associated with high-wavenumber modes will cause aliasing errors that are more significant for higher-order numerical schemes [26]. Therefore, dealiasing treatments are required in flux assembly. A reformulation of the nonlinear advection terms, known as the skewsymmetric form, has been proposed and demonstrated to effectively reduce aliasing errors [27,28]. Significant efforts have been made to further establish numerical conservation with higher-order and non-dissipative schemes [29-31]. For simulations of high-speed flows, the skew-symmetric form has been successfully and widely used [32]. The aliasing error of a product term can be analytically quantified from Fourier analysis, and the exact solution to calculating a product in Fourier space involves conducting a dealiased convolution. Nevertheless, this is impractical for large-scale simulations due to the high computational cost. The product should be directly computed in physical space with the aliasing error reduced or removed. A phase-shift method has been attempted in simulations of turbulent flows using the Fourier spectral method [33], where a shift in physical space of the multiplier fields is conducted to partially or completely cancel the aliasing error in quadratic term calculations. The zero-padding approach is equivalent to the dealiased convolution where the product is computed with sufficiently upsampled resolution, and the result is then downsampled back to the original resolution. As a consequence, all aliasing errors are projected to the extended high-wavenumber modes and eventually truncated after downsampling. However, the increase in the memory footprint of this approach makes it relatively inefficient in large-scale computations. An approach analogous to zero-padding involves filtering the high-wavenumber components that cause aliasing interactions before calculating the product [34]. For spectral methods, this treatment is equivalent to applying zero-padding on a coarser resolution without final downsampling. The aliasing error produced by multiplication can be completely removed, although some unaliased nonlinear interactions are also inevitably excluded by filtering. This approach does not require changing the grid resolution and thus can be conducted at a relatively low cost. As an extra advantage, it preserves the conservation form of the nonlinear fluxes.

Another critical contributor to numerical instability is the numerical discretization of diffusive fluxes. This issue particularly exists in simulations of turbulent flows with collocated finite difference methods. Collocated central difference schemes for first derivatives have a trivial response to the mode at the Nyquist wavenumber and have poor spectral behavior close to the Nyquist wavenumber. As a result, the dispersion error from the divergence of advective fluxes occurs as spurious high-wavenumber, including grid-to-grid, oscillations. These oscillations are supposed to be dissipated by the diffusion mechanism. However, due to the insufficient spectral resolution in the high-wavenumber regime of collocated central difference schemes, by applying the first derivative scheme twice, these oscillations will pile up. Some improvements have been made by evenly appending more grid points to the stencil to optimize the dispersion relation in the high-wavenumber regime [35,36]. It can be proved, however, that the trivial Nyquist wavenumber response is unavoidable in collocated central difference schemes [19]. One treatment of the diffusion term is to reformulate the flux divergence using the differentiation product rule to recover the Laplacian term and inner product of the gradients of the diffusivity coefficients and flow variables such as velocity and temperature; this has a much improved spectral response in high-wavenumber regimes including at the Nyquist wavenumber. Nevertheless, the conservation form is broken. Numerical filters have also been utilized in LES and under-resolved simulations [22,37]. As an extra note, this type of filtering is directly applied to the solution variables for the sake of robustness and should be distinguished from the dealiasing filtering for the calculation of nonlinear terms [34], the explicit filtering in grid-independent LES [38], or test filters in numerical models [13,39]. Based on the transfer function behavior, a practical filtering operation can completely remove grid-to-grid oscillations and largely weaken near-Nyquist high-wavenumber features while preserving the low-wavenumber and moderate-wavenumber features. Serious evaluation of the impact of solution filtering is required to establish the accuracy of the method [22,37,40].

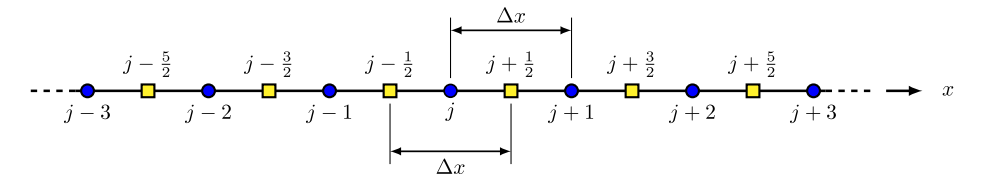


Fig. 1. Schematic of one-dimensional discretization with a uniform mesh.

Staggered grids, on the other hand, have considerably enhanced behavior in high-wavenumber feature capturing. The staggered first derivative scheme used in the divergence operator has a non-trivial response to the Nyquist wavenumber mode due to phase shifting. The staggered grid approach was originally proposed for solving the pressure-velocity decoupling issue in incompressible flow simulations [41] and has been widely used as a standard approach [42]. An improvement in robustness has also been demonstrated in simulations of compressible turbulent flows using compact finite difference methods [43]. However, the storage of variables on a staggered grid can be complicated. Variables are stored at nodal points and edges along each direction to be consistent with flux assembly. Further variable transformations are needed in compressible flow simulations. Additionally, the fluxes have to be assembled at different locations for different governing equations in the system.

While finite difference methods are formulated on a structured mesh, problems involving complex geometries or local mesh refinement can be actualized via an invertible mapping [44]. A uniform Cartesian grid, known as the computational domain or reference domain, is generated and mapped to a curvilinear mesh, known as the physical domain or actual domain. The mapping is defined by a metric tensor and its inverse. The primitive variables are constructed using a basis in the physical domain, and the differential operations are conducted in the reference domain. Due to the metric tensor, extra nonlinear interactions are created. The analysis has shown that the calculation of the metric tensor must be consistent with the divergence operator to cancel the numerical error that causes numerical instability; this is also known as the geometric conservation law (GCL) [45]. Further works have shown GCL-consistent computations in conjunction with collocated compact finite difference methods and shock capturing schemes [46,47].

This work proposes an improved finite difference framework for simulations of compressible turbulent flows. The divergence operations are based on staggered schemes while all conservative variables are stored at collocated grid points. This framework is particularly favorable to high-order compact numerical schemes and reduces the aliasing error in nonlinear flux assembly and high-wavenumber viscous dissipation. The formulations on both uniform Cartesian mesh and curvilinear mesh are constructed. The metric generation approach is constructed in accordance with the numerical schemes and is proved to be GCL-consistent. The elementary numerical schemes are described in Sec. 2. The overall computational framework for the compressible Navier-Stokes system is described in Sec. 3. Lastly, some benchmark tests and demonstrative examples are provided in Sec. 4.

#### 2. Numerical schemes

In this section, the elementary numerical schemes used in the proposed computational framework and their properties are described. A uniform mesh is generated with grid spacing  $\Delta x$  as shown in Fig. 1. A smooth profile, f(x), is discretized on the given computational mesh with  $f_j = f(x_j)$  at the nodal grid points. Based on the derivations in Ref. [19] and Ref. [43], a family of tridiagonal collocated compact finite difference schemes for evaluation of the first derivative can be written as

$$\alpha f'_{j-1} + f'_j + \alpha f'_{j+1} = a \frac{f_{j+1} - f_{j-1}}{2\Delta x} + b \frac{f_{j+2} - f_{j-2}}{4\Delta x} \tag{1}$$

where  $f'_j$  represents the numerically evaluated first derivative of f(x) at  $x_j$ . This set of schemes is formally fourth-order accurate for a generic value of  $\alpha$  with the following constraints on the coefficients a and b.

$$a = \frac{2}{3}(\alpha + 2) \tag{2}$$

$$b = \frac{1}{3}(4\alpha - 1) \tag{3}$$

Additionally, as shown in Fig. 1, a set of edge grid points are located at a half grid-spacing offset and staggered from the nodal grid points. The smooth profile f(x) evaluated at the edge-staggered grid points can be denoted as  $f_{j\pm 1/2} = f(x_j \pm \Delta x/2)$ . A family of tridiagonal staggered compact finite difference schemes for the first derivative evaluation can be expressed as

$$\alpha f'_{j-1} + f'_j + \alpha f'_{j+1} = a \frac{f_{j+1/2} - f_{j-1/2}}{\Delta x} + b \frac{f_{j+3/2} - f_{j-3/2}}{3\Delta x}$$
(4)

where fourth-order accuracy is preserved for a generic value of  $\alpha$  with the following constraints on a and b.

$$a = \frac{3}{8}(-2\alpha + 3) \tag{5}$$

$$b = \frac{1}{8}(22\alpha - 1) \tag{6}$$

A family of tridiagonal compact staggered interpolation schemes can be written as

Table 1
Coefficients of the 6th-order compact schemes

Scheme	Equation	α	a	b
collocated finite difference	(1)	1/3	14/9	1/9
staggered finite difference	(4)	9/62	63/62	17/62
midpoint interpolation	(7)	3/10	3/2	1/10

$$\alpha f_{j-1}^{I} + f_{j}^{I} + \alpha f_{j+1}^{I} = a \frac{f_{j+1/2} + f_{j-1/2}}{2} + b \frac{f_{j+3/2} + f_{j-3/2}}{2}$$

$$(7)$$

where  $f_j^I$  denotes the numerically interpolated values of f(x) at  $x_j$ . The family of compact interpolations is formally fourth-order accurate if the following constraints are satisfied.

$$a = \frac{1}{8}(10\alpha + 9) \tag{8}$$

$$b = \frac{1}{8}(6\alpha - 1) \tag{9}$$

Due to the symmetry of the expression, Eq. (4) and Eq. (7) can be used to calculate corresponding results both from collocated (nodal) to edge-staggered points and from edge-staggered to collocated points with a shift of  $\pm 1/2$  in the grid index. A scheme degenerates to an explicit method upon choosing  $\alpha=0$ . For  $\alpha\neq 0$ , a tridiagonal linear system needs to be solved. For a large-scale computation, an effective parallel direct solution method is described in Ref. [48]. The leading-order truncation error can vanish if a specific value of  $\alpha$  is set in each scheme, and sixth-order schemes will be formulated with the most compact stencil. The coefficients of the sixth-order compact schemes are listed in Table 1.

The spectral response can be investigated from Fourier analysis. Assume that a one-dimensional periodic domain defined on  $x \in [0, L)$  is discretized on a uniform mesh with N grid points. The grid spacing is  $\Delta x = L/N$ , so that  $x_j = j\Delta x$  for  $j \in \{j \in \mathbb{N} \mid j < N\}$ . The discrete Fourier representation of  $f_j$  is given by

$$f_j = \sum_{n=-N/2}^{N/2-1} \hat{f}_n e^{2\pi i n j/N}$$
 (10)

where  $\widehat{f_n} \in \mathbb{C}$  is the discrete Fourier transform of f(x), and  $i = \sqrt{-1}$  is the imaginary unit. A wavenumber,  $k_n$ , is introduced as  $k_n = 2\pi n/L$ . For  $L = N\Delta x$  and  $n \in [-N/2, N/2)$ , it can be shown that  $k_n\Delta x \in [-\pi, \pi)$ . Additionally, the modes with respect to  $k_{\pm N/2}\Delta x = \pm \pi$  are equivalent, and such  $k_{\pm N/2}$  is known as the Nyquist wavenumber. The exponent on the right-hand side of Eq. (10) yields  $2\pi i n j/N = i k_n x_i$ .

The Fourier representation of the first derivative can be analytically written as

$$\frac{df}{dx}\Big|_{x_j} = \sum_{n=-N/2}^{N/2-1} ik_n \hat{f}_n e^{ik_n x_j}$$
(11)

and an identical expression can be formulated for the numerical calculation of the first derivatives.

$$f_j' = \sum_{n=-N/2}^{N/2-1} i k_n' \hat{f}_n e^{ik_n x_j}$$
 (12)

where  $k'_n$  is known as the modified wavenumber [49,19], and the spectral error is indicated by the discrepancy between  $k'_n$  and  $k_n$ . For simplicity, the subscript n is dropped while discussing the single-mode behavior, so that  $k \in \{k_n \mid n \in \mathbb{Z} \land n/N \in [-1/2, 1/2)\}$  and  $k' \in \{k'_n \mid n \in \mathbb{Z} \land n/N \in [-1/2, 1/2)\}$ . Substituting the expression in Eq. (10) into the finite difference schemes in Eq. (1) and Eq. (4), the modified wavenumbers can be obtained as

$$k'\Delta x = \frac{a\sin(k\Delta x) + \frac{1}{2}b\sin(2k\Delta x)}{1 + 2a\cos(k\Delta x)} \tag{13}$$

and

$$k'\Delta x = \frac{2a\sin\left(\frac{1}{2}k\Delta x\right) + \frac{2}{3}b\sin\left(\frac{3}{2}k\Delta x\right)}{1 + 2a\cos(k\Delta x)} \tag{14}$$

respectively. For central difference schemes, the modified wavenumbers are all real-valued,  $k' \in \mathbb{R}$ . As shown in Eq. (13), at the Nyquist wavenumber,  $k'\Delta x = 0$  holds for all collocated central difference schemes, while for staggered central difference schemes,  $k'\Delta x = \frac{7-10\alpha}{3-6\alpha}$  at the Nyquist wavenumber. The modified wavenumbers of the collocated and staggered sixth-order compact finite difference schemes are plotted in Fig. 2. For reference, the modified wavenumber profiles for the second-order, fourth-order, and sixth-order explicit central difference schemes are also plotted. By comparison, the staggered schemes have significantly improved

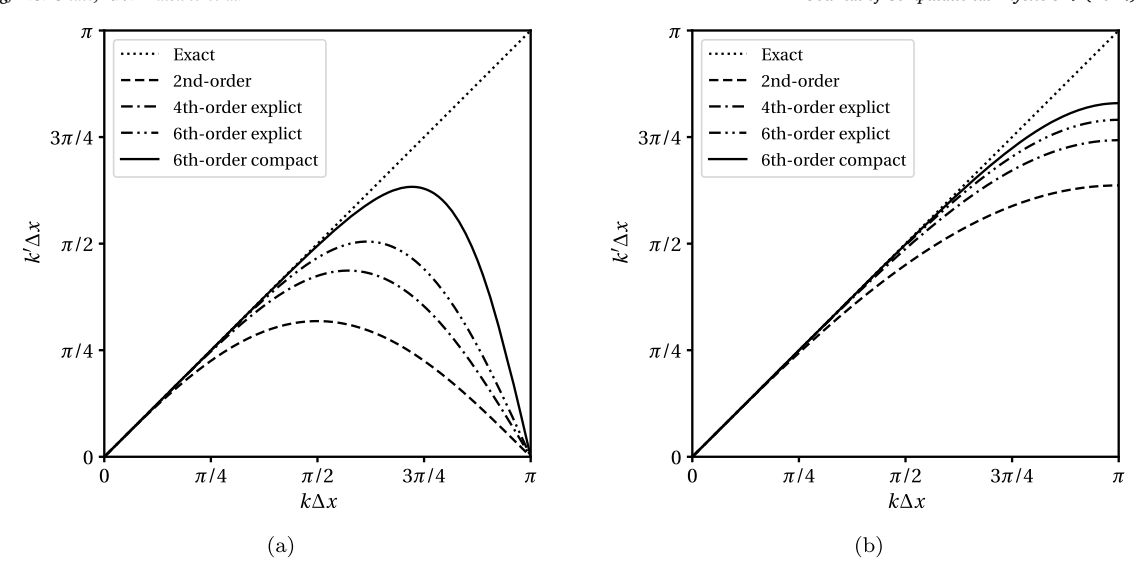


Fig. 2. Modified wavenumber profiles of some central difference schemes: (a) collocated schemes; (b) staggered schemes.

spectral behavior compared to the collocated schemes especially in the high-wavenumber regime. For both types of schemes shown in Fig. 2, the sixth-order compact difference schemes have the most accurate modified wavenumbers. The modified wavenumber of the collocated sixth-order compact scheme is relatively accurate for  $k\Delta x < \pi/2$ , and  $k'/k = \frac{28}{9\pi} \approx 0.990$  for  $k\Delta x = \pi/2$ . Beyond  $k\Delta x \approx 2.267$ , k' starts to decrease with k, and large discrepancies occur. The modified wavenumber of the staggered sixth-order compact scheme has a broader accurate wavenumber regime. k' monotonically increases with k over the entire spectral domain.  $k'/k = \frac{206\sqrt{2}}{93\pi} \approx 0.997$  for  $k\Delta x = \pi/2$ , and  $k'/k \approx 0.83$  at the Nyquist wavenumber. Using the discrete Fourier representation in Eq. (10), the exact value at a staggered grid point is

$$f_{j+1/2} = \sum_{n=-N/2}^{N/2-1} \hat{f}_n e^{2\pi i n(j+1/2)/N}$$
(15)

Analogously, substituting the Fourier representation in an interpolation scheme, an expression equivalent to the following form can be obtained.

$$f_{j+1/2}^{I} = \sum_{n=-N/2}^{N/2-1} T(k_n \Delta x) \hat{f}_n e^{2\pi i n(j+1/2)/N}$$
(16)

where  $T(k\Delta x)$  is known as the transfer function [19]. The subscript n is dropped for simplicity in the discussion of the transfer function, consistent with what is defined in the previous discussion so that k is an instantiation of the set of discrete wavenumbers,  $k \in \{k_n \mid n \in \mathbb{Z} \land n/N \in [-1/2, 1/2)\}$ . This indicates that a numerical interpolation is equivalent to the exact interpolation of a filtered profile. For a central interpolation scheme, the transfer function is also real valued,  $T(k\Delta x) \in \mathbb{R}$ . The analytical expression of the transfer function for the interpolation scheme formulated in Eq. (7) is given as follows.

$$T(k\Delta x) = \frac{a\cos\left(\frac{1}{2}k\Delta x\right) + b\cos\left(\frac{3}{2}k\Delta x\right)}{1 + 2a\cos(k\Delta x)} \tag{17}$$

and its profile is shown in Fig. 3 in comparison with the second-order, fourth-order, and sixth-order explicit central interpolation schemes. Comparing the three profiles for the transfer function, all interpolation schemes preserve the mean value, and the sixth-order compact interpolation shows the best spectral behavior in preserving the mode amplitude for  $k\Delta x < \pi/2$ . At  $k\Delta x = \pi/2$ , the values of the transfer functions for the second-order scheme, fourth-order explicit scheme, sixth-order explicit scheme, and sixth-order compact scheme are approximately 0.707, 0.884, 0.950 and 0.990, respectively. In the high-wavenumber regime, the transfer function profile decreases and eventually reaches zero at the Nyquist wavenumber. These filtering effects embedded in the numerical interpolation schemes favor flux dealiasing, which is fully discussed in Sec. 3.

The linear response of the numerical dispersion and dissipation is discussed using a model advection-diffusion equation, shown as follows:

$$\frac{\partial \phi}{\partial t} + \nabla \cdot [\nu(\theta)\phi] = \nabla \cdot [\nu\nabla\phi] \tag{18}$$

The model problem is defined on a two-dimensional periodic domain for  $\mathbf{x} = (x, y) \in [0, L_y) \times [0, L_y)$ .  $\phi(x, y, t)$  is the dependent variable.  $v(\theta) = V\left(\hat{e}_x \cos \theta + \hat{e}_y \sin \theta\right)$  is the advective velocity, where V and  $\theta$  are constant, and  $\hat{e}_x$  and  $\hat{e}_y$  form a constant orthogonal

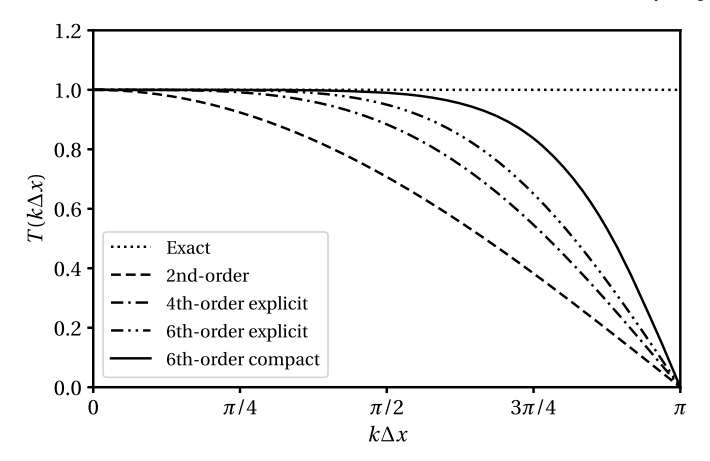


Fig. 3. Transfer functions of several central interpolation schemes.

basis of a Cartesian coordinate system. v is a constant diffusivity. Eq. (18) is expressed in conservation form, where  $v\phi$  is the linear advective flux, and  $v\nabla\phi$  is the linear diffusive flux. The computational domain is discretized with a uniform mesh containing  $N_x$  and  $N_y$  grid points in x and y dimensions respectively. A two-dimensional discrete Fourier transform can be denoted as

$$\phi(\mathbf{x}_{pq}, t) = \sum_{m = -N_{\chi}/2}^{N_{\chi}/2 - 1} \sum_{n = -N_{\chi}/2}^{N_{y}/2 - 1} \widehat{\phi}_{mn}(t) e^{i\mathbf{k}_{mn} \cdot \mathbf{x}_{pq}}$$
(19)

where  $\mathbf{x}_{pq} = x_p \hat{\mathbf{e}}_x + y_q \hat{\mathbf{e}}_y$  represents two-dimensional coordinates, and  $\mathbf{k}_{mn} = k_{xm} \hat{\mathbf{e}}_x + k_{yn} \hat{\mathbf{e}}_y$  is the wavenumber vector. The spatial coordinates can be calculated as  $x_p = L_x p/N_x$  and  $y_q = L_y q/N_y$  respectively, and the two components of the wavenumber vector are defined as  $k_{xm} = 2\pi m/L_x$  and  $k_{yn} = 2\pi n/L_y$  respectively. In the following discussion of single-mode behavior, the subscripts m and n are dropped as in previous discussions, so that without a subscript, a quantity can be interpreted as an instantiation of the set of all admissible values,  $k_x \in \{k_{xm} \mid m \in \mathbb{Z} \land m/N_x \in [-1/2, 1/2)\}, k_y \in \{k_{yn} \mid n \in \mathbb{Z} \land n/N_y \in [-1/2, 1/2)\},$   $\hat{\phi} \in \{\hat{\phi}_{mn} \mid m, n \in \mathbb{Z} \land m/N_x, n/N_y \in [-1/2, 1/2)\},$  and  $\mathbf{k} = k_x \hat{\mathbf{e}}_x + k_y \hat{\mathbf{e}}_y$ .

Considering the errors caused by the schemes, the numerical solution to a semi-discretized form of Eq. (18) is consistent with the following modified ordinary differential equation in Fourier space.

$$\frac{d\widehat{\phi}}{dt} + i\mathbf{k} \cdot \mathbf{v}'\widehat{\phi} = -\mathbf{v}'k^2\widehat{\phi} \tag{20}$$

where  $k^2 = \mathbf{k} \cdot \mathbf{k}$ , and  $\mathbf{v}'$  and  $\mathbf{v}'$  can be interpreted as the modified spectral advective velocity and modified spectral diffusivity respectively. According to the definition of the modified wavenumber in Eq. (12),  $\mathbf{v}'$  and  $\mathbf{v}'$  account for the effects of the modified wavenumber. Their expressions are given in the following equations.

$$\mathbf{v}'(\theta, \mathbf{k}) = V\left(\hat{e}_x \frac{k_x''}{k_x} \cos \theta + \hat{e}_y \frac{k_y''}{k_y} \sin \theta\right) \tag{21}$$

$$v'(k) = v\left(\frac{k_x'^2 + k_y'^2}{k^2}\right) \tag{22}$$

where  $k_x''$  and  $k_y''$  can be interpreted as the effective modified wavenumbers corresponding to the combination of all the discrete operations, including interpolation and differentiation, along the x- and y-directions respectively and treated as functions of  $k_x$  and  $k_y$  respectively, consistent with the one-dimensional analysis. For staggered differential operations, interpolation schemes are required to evaluate advective fluxes. Therefore, the effective modified wavenumbers should consider both the transfer function and the modified wavenumber from the staggered differentiation,  $k_x'' \Delta x = T(k_x \Delta x)k_x' \Delta x$  and  $k_y'' \Delta y = T(k_y \Delta y)k_y' \Delta y$ . For collocated differential operations, interpolation schemes are not needed. Accordingly, the effective modified wavenumbers of a collocated scheme are equal to its modified wavenumbers,  $k_x'' \Delta x = k_x' \Delta x$  and  $k_y'' \Delta y = k_y' \Delta y$ . Mapping to a polar coordinate system, the wavenumber vector can be written as  $\mathbf{k} = |k| \left(\hat{e}_x \cos \varphi + \hat{e}_y \sin \varphi\right)$ , where  $\varphi$  defines an angle of observation. Consistent with the scaling of the wavenumber compo-

nents in each dimension, the dimensionless wavenumber magnitude can be expressed as  $|k| \delta$ , where  $\delta(\varphi) = \sqrt{\Delta x^2 \cos^2 \varphi + \Delta y^2 \sin^2 \varphi}$ . If  $\Delta x = \Delta y$ , then  $\delta$  is independent of  $\varphi$ , and the wavenumber magnitude is scaled by the uniform grid spacing.

The two-dimensional spectral dispersion is characterized by the modified spectral advective velocity, v'. For an exact differentiation, v' = v for all resolved Fourier modes. For a numerical solution, v' has non-constant spectral behavior with respect to the advective direction,  $\theta$ , and the wave orientation,  $\varphi$ . If  $\theta = \varphi = 0$ , the model problem becomes one-dimensional. The numerical dispersion in the linear advection is shown in Fig. 4. It can be seen that among the listed collocated schemes, the sixth-order compact finite

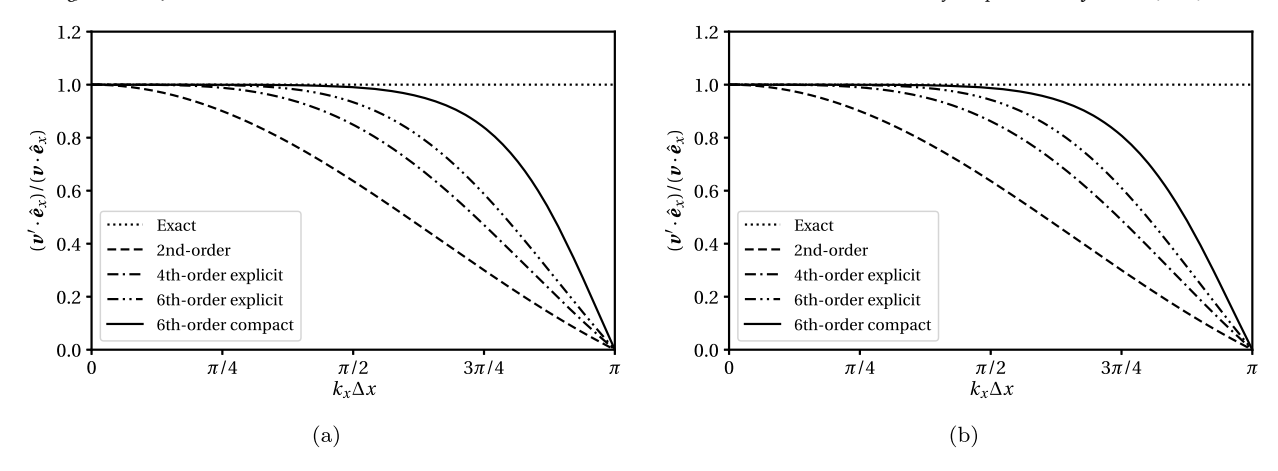


**Fig. 4.** Profiles of the modified spectral advection velocities in one-dimensional computations: (a) collocated difference schemes; (b) staggered difference schemes combined with central interpolation schemes. As  $k_{\gamma}\Delta x \rightarrow 0$ , the plots show their asymptotic behaviors.

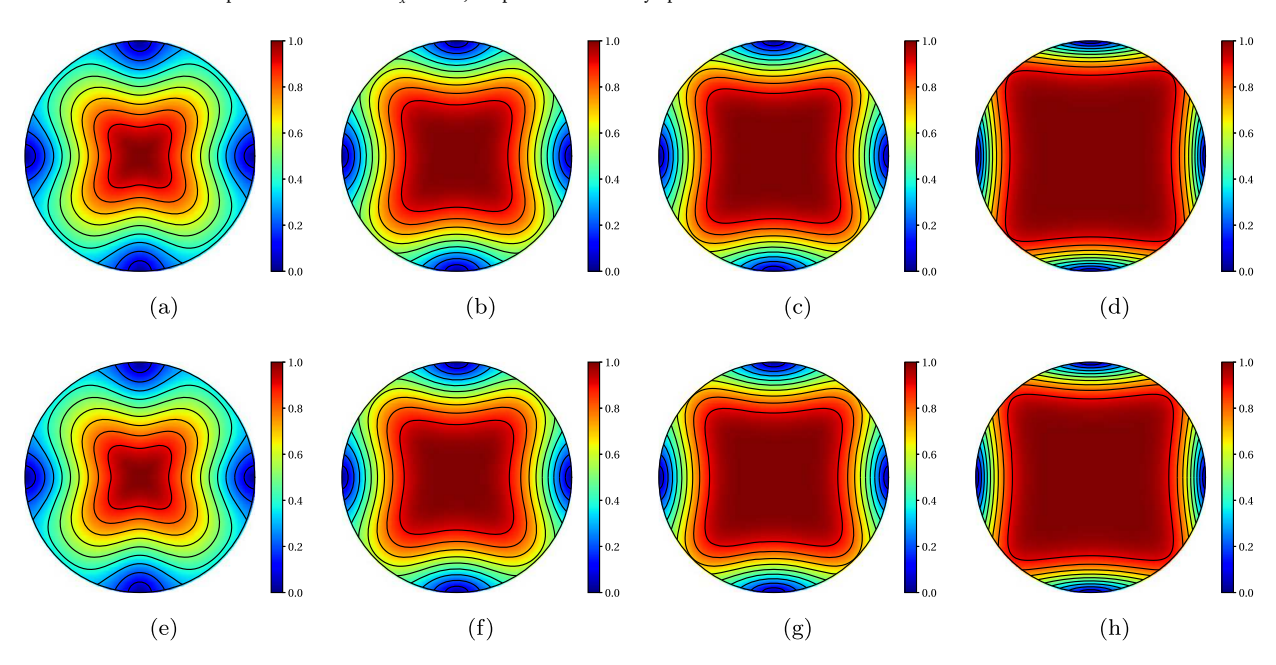


Fig. 5. Relative spectral advective speeds,  $(v' \cdot \hat{e}_l) / (v \cdot \hat{e}_l)$ , shown in  $|k|\delta - \varphi$  polar coordinate system, where  $\hat{e}_l = \hat{e}_x \cos \theta + \hat{e}_y \sin \theta$  and  $\varphi = \theta$ : (a) collocated second-order difference; (b) collocated fourth-order explicit difference; (c) collocated sixth-order explicit difference; (d) collocated sixth-order compact difference; (e) staggered second-order difference with interpolation; (f) staggered fourth-order explicit difference with interpolation; (g) staggered sixth-order explicit difference with interpolation; (h) staggered sixth-order compact difference with interpolation. The isocurves are generated based on a linear scale. As  $k \to 0$ , the contours show their asymptotic behaviors. (For interpretation of the colors in the figure(s), the reader is referred to the web version of this article.)

difference scheme best resolves the advection of the modes for  $k_x \Delta x < \pi/2$ . However, the advection of the Nyquist wavenumber mode cannot be resolved by the collocated central difference schemes, and the mode will become a standing wave. In comparison, for higher-order schemes, a staggered scheme has spectral behavior nearly identical to that of the collocated scheme of the same order even though the staggered numerical differential operations have significantly improved modified wavenumbers. For the second-order discretizations, the spectral behavior of the staggered and collocated schemes is completely identical. This is because the interpolation is also considered as a step of the staggered calculation that suppresses the overall high-wavenumber features. The leading-order truncation error for the model problem of each scheme is derived in Appendix A and listed in Table A.3 to quantify the response of numerical errors with respect to the local solution features in physical space. For a two-dimensional configuration, the anisotropy is shown in Fig. 5 and Fig. 6. For the linear system, without loss of generality, let  $\theta = \varphi$  and  $\Delta x = \Delta y$ . Accordingly, the contours in Fig. 5 are equivalent to |v'|/|v|. Most of the contours in Fig. 5 present square-like shapes. This is because a Cartesian mesh only defines a rectangular domain and is not perfectly isotropic. As a result, the corresponding spectral domain is also rectangular. As a fair comparison, only  $|k| \delta \le \pi$  is considered. Due to the spectral behavior of the collocated finite difference schemes and central interpolation schemes, |v'| = 0 is unavoidable. This limits the isotropy of the evaluation in the high-wavenumber regime. Comparing the two-dimensional spectral behaviors, the collocated schemes and staggered schemes are still nearly identical. As the formal order

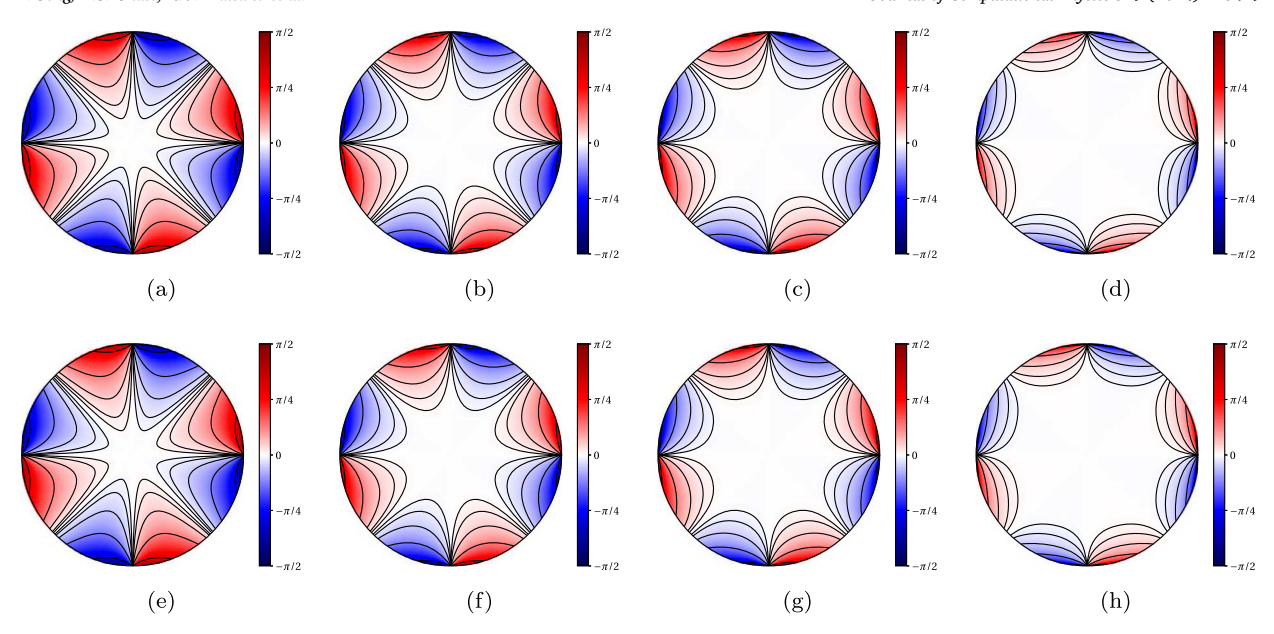


Fig. 6. Errors of the modified spectral advective velocity angles,  $\theta' - \theta$  where  $\theta'(k)$  is the polar angle of the modified spectral advective velocity, v', i.e.,  $v' = |v'| (\hat{e}_x \cos \theta' + \hat{e}_y \sin \theta')$ . The errors are shown in  $|k|\delta - \varphi|$  polar coordinate system with  $\varphi = \theta$ : (a) collocated second-order difference; (b) collocated fourth-order explicit difference; (c) collocated sixth-order explicit difference with interpolation; (f) staggered fourth-order explicit difference with interpolation; (g) staggered sixth-order explicit difference with interpolation; (h) staggered sixth-order compact difference with interpolation. The isocurves are generated based on a logarithmic scale. As  $|v'| \to 0$ , the contours show their asymptotic behaviors.

of accuracy increases, the isotropy successively improves, and the sixth-order compact schemes similarly show the best performance among all listed schemes. A consistent observation can also be obtained by comparing the error of the advective directions in Fig. 6. Along the x- and y-directions, the advection degenerates to a one-dimensional problem. The numerical schemes along the advection do not affect the advective direction, and the numerical schemes in the orthogonal direction make no contribution to the results. Along the domain-diagonal direction, the errors of the numerical schemes in the x- and y-directions are canceled. Therefore, for both cases, there is no error in resolving the advective direction. However, other than the axial and domain-diagonal directions, the numerical error in the advective velocity direction occurs as imbalanced errors in the evaluation of the projected advective speeds.

The spectral dissipation can be investigated from the modified spectral diffusivity, v'. For the one-dimensional advection, the relative values of v' are shown in Fig. 7. The exact differentiation should preserve v for all resolved wavenumbers. Compared to Fig. 4, the effects of the modified wavenumber reduction are worse in the diffusion term, since two derivative operations are applied. The collocated schemes do not resolve the Nyquist wavenumber damping mechanism, which adversely affects the numerical stability in nonlinear problems. In contrast, the staggered schemes have a much enhanced high-wavenumber damping performance, which will make nonlinear systems more robust. This property is also supported by the amplitude of the leading-order truncation error which is derived in Appendix A and provided in Table A.3 for each of the schemes. By comparison, the staggered differential schemes significantly improve the solution accuracy by reducing the amplitude of the leading-order truncation error in the calculation of the viscous term. The anisotropy is shown in Fig. 8. As  $\varphi$  varies, the collocated second-order scheme only shows isotropic behavior at low wavenumbers. The collocated sixth-order schemes have a much improved isotropy compared to the second-order schemes. Nevertheless, the most significant improvement is observed by using staggered schemes. An alternative way to improve the performance of the diffusion term in damping high-wavenumber modes is to use second derivative operators [19,43]. However, this treatment is at the cost of sacrificing the conservation form. The approach can be derived based on the product rule of calculus,  $\nabla \cdot [v\nabla \phi] = \nabla v \cdot \nabla \phi + v\nabla^2 \phi$ , where the calculation of  $\nabla^2 \phi$  is based on second partial derivative operators.

#### 3. Computational framework

In this section, the computational framework is fully described. The framework requires midpoint interpolation and collocated and staggered central schemes for the calculation of first derivatives. It is compatible with schemes of an arbitrary order of accuracy. In particular, the proposed framework is favorable to applications of high-order compact schemes.

#### 3.1. Governing equations

The compressible Navier-Stokes equations, including conservation of mass, momentum, and total energy, are formulated as

$$\frac{\partial \rho}{\partial t} + \frac{\partial}{\partial x_j} \left( \rho u_j \right) = 0 \tag{23}$$

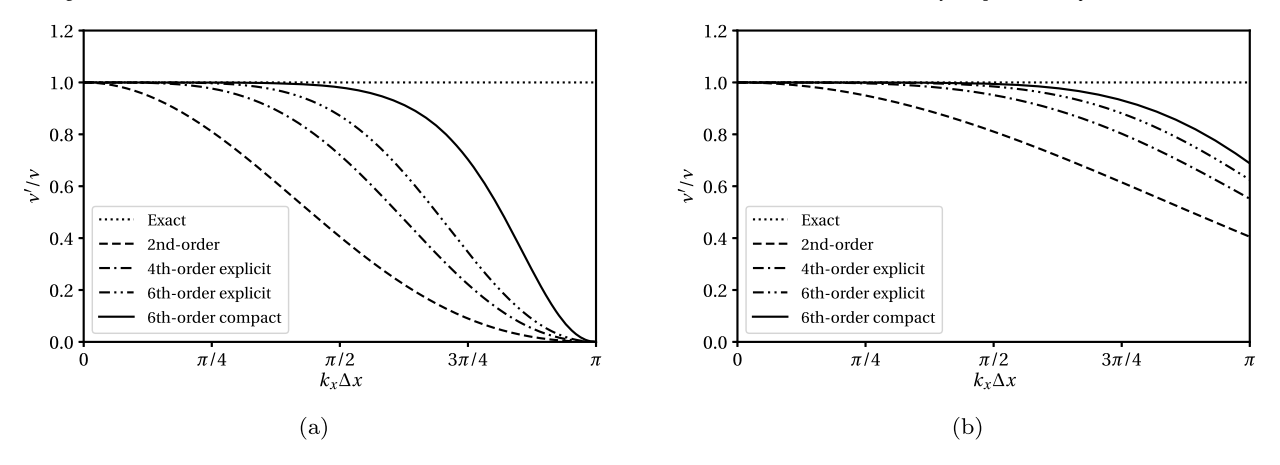


**Fig. 7.** Profiles of the modified spectral diffusivities in one-dimensional computations: (a) collocated difference schemes; (b) staggered difference schemes. As  $k_x \Delta x \to 0$  the plots show their asymptotic behaviors.

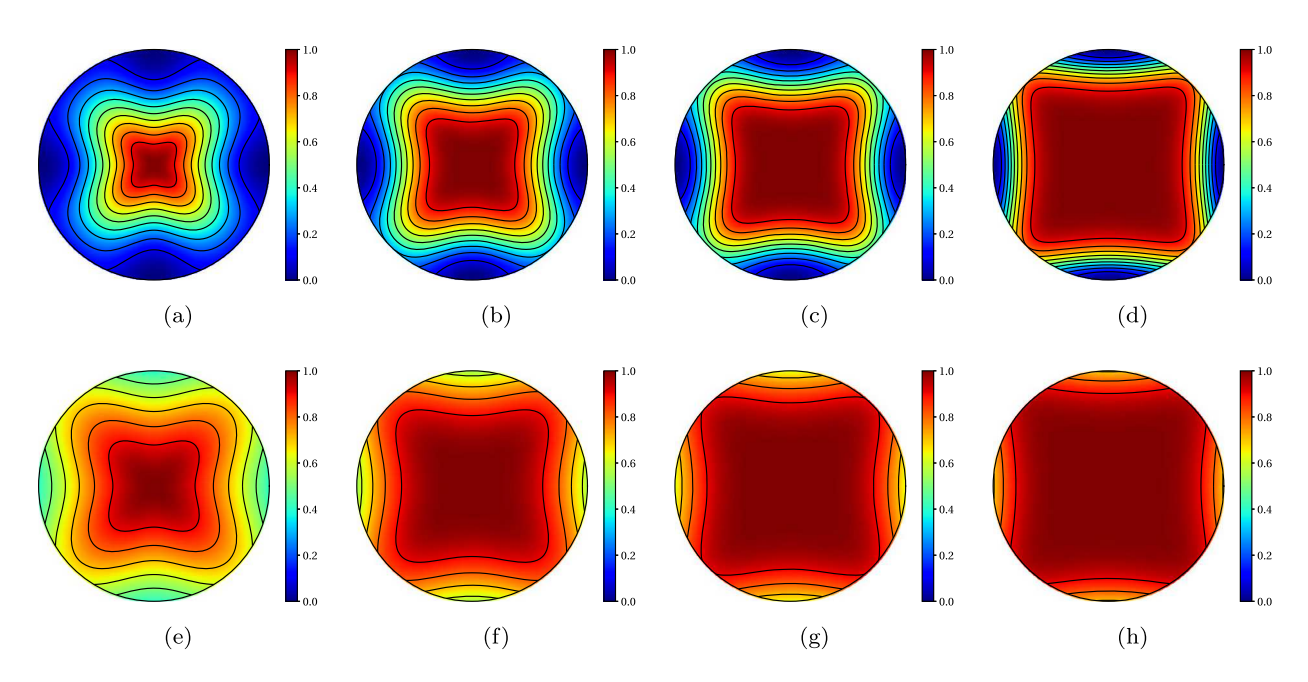


Fig. 8. Relative modified spectral diffusivities v'(k)/v shown in  $|k|\delta-\varphi$  polar coordinate system: (a) collocated second-order difference; (b) collocated fourth-order explicit difference; (c) collocated sixth-order explicit difference; (d) collocated sixth-order compact difference; (e) staggered second-order difference; (f) staggered fourth-order explicit difference; (g) staggered sixth-order explicit difference; (h) staggered sixth-order compact difference. The isocurves are generated based on a linear scale. As  $k \to 0$ , the contours show their asymptotic behaviors.

$$\frac{\partial \rho u_i}{\partial t} + \frac{\partial}{\partial x_i} \left( \rho u_i u_j + p \delta_{ij} \right) = \frac{\partial \sigma_{ij}}{\partial x_i} \tag{24}$$

$$\frac{\partial \rho e}{\partial t} + \frac{\partial}{\partial x_i} \left( \rho h u_j \right) = \frac{\partial}{\partial x_i} \left( u_i \sigma_{ij} - q_j \right) \tag{25}$$

where the expressions are given in index notation [50] with an independent spatial dimension denoted by each free index and a summation over all spatial dimensions implied by each pair of repeated indices. In the equations,  $\rho$  is the density;  $u_i$  is the velocity vector; p is the pressure;  $\delta_{ij}$  is the Kronecker delta characterizing an identity tensor;  $\sigma_{ij}$  is the viscous stress tensor; e is the specific total energy; h is the specific total enthalpy; and  $q_j$  is the heat flux vector. The governing equations are given in conservation form. The fluxes on the left-hand side of each equation are known as the inviscid fluxes, and the fluxes on the right-hand side are the viscous fluxes. If all the viscous fluxes are dropped, the governing equations will degenerate to an Euler system.  $\sigma_{ij}$  and  $q_j$  are formulated based on the constitutive relations of the fluid. For a Newtonian fluid, the viscous stress tensor is calculated as

$$\sigma_{ij} = 2\mu S_{ij} + \left(\beta - \frac{2}{3}\mu\right) \frac{\partial u_k}{\partial x_k} \delta_{ij} \tag{26}$$

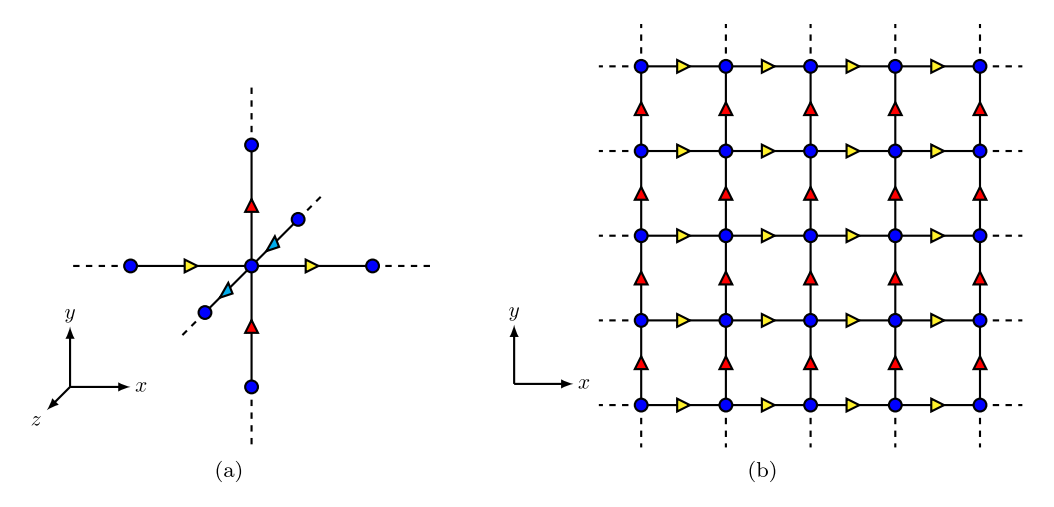


**Fig. 9.** Uniform Cartesian mesh: (a) detailed view of the three-dimensional structure; (b) projected view on x-y plane. The blue circles indicate the collocated grid points, and yellow, red and cyan triangles mark the edge-staggered grid points in the x-, y- and z-directions respectively.

where  $\mu$  and  $\beta$  are the dynamic shear viscosity and bulk viscosity respectively, and  $S_{ij}$  is the strain rate tensor, defined as

$$S_{ij} = \frac{1}{2} \left( \frac{\partial u_i}{\partial x_j} + \frac{\partial u_j}{\partial x_i} \right) \tag{27}$$

The heat flux vector,  $q_i$ , is modeled by the Fourier's law of heat conduction:

$$q_j = -\kappa \frac{\partial T}{\partial x_j} \tag{28}$$

where  $\kappa$  is the thermal conductivity, and T is the temperature. The specific total energy, e, is defined as

$$e = e_{\text{th}} + \frac{1}{2}u_j u_j \tag{29}$$

where  $e_{\mathrm{th}}$  is the specific internal energy. The specific total enthalpy, h, is defined as

$$h = e + p/\rho \tag{30}$$

The internal energy,  $e_{\rm th}$ , and the pressure, p, are calculated based on an equation of state (EOS). For a pure substance, they can be expressed as functions of  $\rho$  and T in general. For a calorically perfect gas, they can be calculated as

$$p = \rho RT \tag{31}$$

and

$$e_{\rm th} = \frac{RT}{\gamma - 1} \tag{32}$$

where R is the specific gas constant, and  $\gamma$  is the ratio of specific heats. The system is finally closed by giving the expressions for all the transport properties,  $\mu$ ,  $\beta$ , and  $\kappa$ . For LES or DNS with shock-capturing schemes active at a separated scale, these transport properties may also contain modeled components [12,14,15,37]. The detailed description of the LES formulation used in this work is provided in Appendix B.

# 3.2. Numerical discretization on uniform Cartesian mesh

Consider a uniform Cartesian mesh generated in three-dimensional space. The computational mesh contains collocated grid points and edge-staggered grid points as shown in Fig. 9. During time advancement, all conservative variables evolve only at the collocated grid points, and all fluxes are assembled at the corresponding edge-staggered grid points. The divergence operations are performed by staggered central difference methods using input values at the edge-staggered grid points and generating the results at the collocated grid points. The schematic of the time advancement step is shown in Fig. 10.

The inviscid fluxes are assembled using the primitive variables,  $u_i$ , T and p, that are first calculated from the conservative variables at the collocated grid points and then interpolated to the staggered grid points. The choice of the thermodynamic variables used for interpolation provides flexibility in numerically imposing the boundary conditions in a simulation. Using the interpolated p and T, all other required thermodynamic quantities are recalculated at the staggered grid points based on the EOS. According to the spectral behavior of the interpolation operator, shown in Fig. 3, all interpolated variables have damped high-wavenumber modes. As the

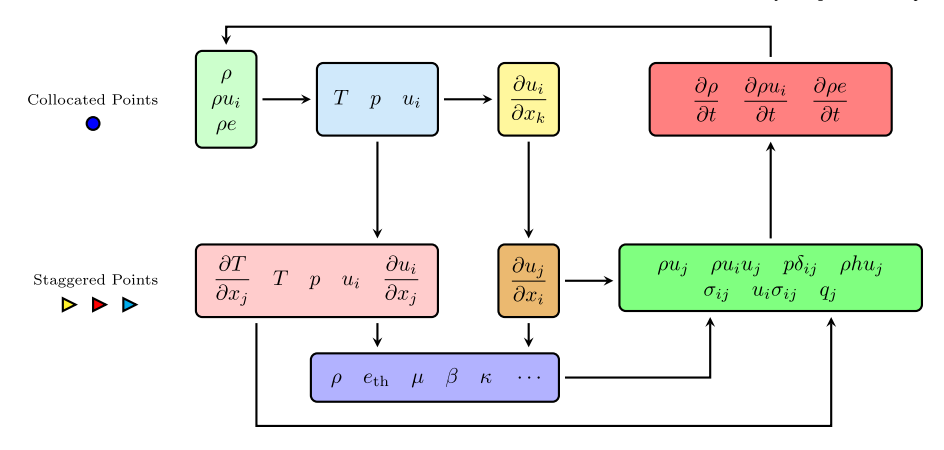


Fig. 10. Schematics of time advancement step.

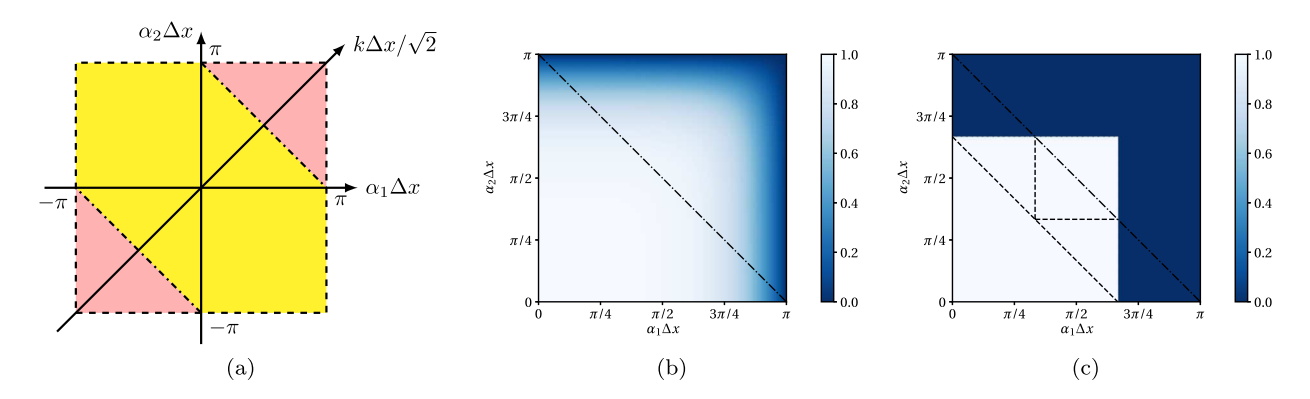


Fig. 11. Quadratic interaction between two fields: (a) schematics; (b) fields are interpolated using the compact sixth-order central scheme. The regions beyond the dash-dotted lines characterize the aliased interactions; (c) fields are preprocessed by a spectrally sharp low-pass filter with cut-off wavenumber at  $2\pi/3$ . The pseudocolor in (b) and (c) are the joint transfer function for each interacted mode.

nonlinear fluxes are assembled, aliasing interactions among high-wavenumber modes in the operands are reduced. The quadratic nonlinear interaction, as an example, is investigated in the following context and shown in Fig. 11. Assuming Q(x) = u(x)v(x) in one-dimensional space, the discrete Fourier representation of the direct numerical product can be written as

$$\sum_{n=-N/2}^{N/2-1} \widehat{Q}_n e^{ikx_j} = \sum_{|l+m| \le N/2} \widehat{u}_l \widehat{v}_m e^{i(\alpha_1 + \alpha_2)x_j} + \sum_{|l+m| > N/2} \widehat{u}_l \widehat{v}_m e^{i(\alpha_1 + \alpha_2)x_j}$$
(33)

where  $\alpha_1(l) = 2\pi l/L$  and  $\alpha_2(m) = 2\pi m/L$  are the wavenumbers for  $l, m \in \{n \in \mathbb{Z} \mid -N/2 \le n < N/2\}$ . The first term on the right-hand side of Eq. (33) represents the resolved interactions, and the second term on the right-hand side represents the aliased interactions. For the resolved interactions, n = l + m and  $k = \alpha_1 + \alpha_2$ , while for the aliased interactions,  $n = l + m \pm N$  for the negative and positive wavenumber modes respectively, and correspondingly,  $k = \alpha_1 + \alpha_2 \pm 2\pi$ . Combined with the schematic shown in Fig. 11a, each location in the two-dimensional plane represents a quadratic interaction between the modes corresponding to wavenumbers  $\alpha_1$  and  $\alpha_2$ . Among all quadratic interactions within the dashed-line box, the regions of aliased interactions are marked in red. The aliased interactions will fold back to the resolved modes colored by yellow. Considering the transfer functions, the numerical product of the interpolated factors can be expressed as

$$\sum_{n=-N/2}^{N/2-1} \widehat{Q}_n^F e^{ikx_j} = \sum_{|l+m| \le N/2} T_{lm} \widehat{u}_l \widehat{v}_m e^{i(\alpha_1 + \alpha_2)x_j} + \sum_{|l+m| > N/2} T_{lm} \widehat{u}_l \widehat{v}_m e^{i(\alpha_1 + \alpha_2)x_j}$$
(34)

where  $\hat{Q}_n^F$  is the discrete Fourier transfer of the numerical product, and  $T_{lm} = T(\alpha_1 \Delta x) T(\alpha_2 \Delta x)$  can be interpreted as the joint transfer function. Although the magnitude of the aliasing error depends on the factors, the amount of reduction can be quantified by the profile of  $T_{lm}$ . For the sixth-order compact interpolation, the profile of the joint transfer function is shown in Fig. 11b. As a reference, the "2/3-rule," which identifies the necessary filtered modes to eliminate the aliasing error in a quadratic interaction [34], is shown in Fig. 11c. With the interpolation of the primitive variables, although the aliasing error cannot be perfectly eliminated, the aliased interactions are largely reduced to improve the robustness. Additionally, in the compressible Navier-Stokes system, the inviscid fluxes

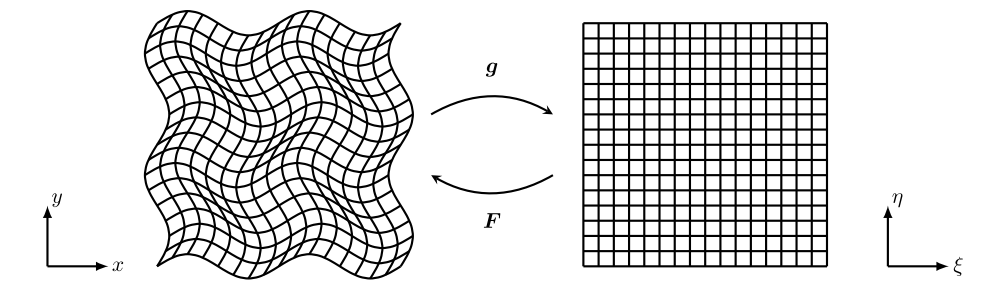


Fig. 12. Invertible mapping between a curvilinear mesh in the physical domain (left) and a uniform Cartesian mesh in a reference domain (right).

involve cubic and quartic (in the formulation for a curvilinear coordinate system) interactions. For products involving more than two factors, the schematics are similar but need to be shown using a hyperplane in a higher-dimensional space.

Besides the primitive variables, the velocity and temperature gradients are needed for the viscous fluxes. In order to maximize the performance of high-wavenumber dissipation, the gradient component aligned with the flux direction and the divergence operation are evaluated by the staggered difference schemes. For the Navier-Stokes equations, the diffusion term in Eq. (24) can be rearranged as

$$\frac{\partial \sigma_{ij}}{\partial x_i} = \frac{\partial}{\partial x_j} \left( \mu \frac{\partial u_i}{\partial x_j} \right) + \frac{\partial}{\partial x_i} \left[ \mu \frac{\partial u_j}{\partial x_i} + \left( \beta - \frac{2}{3} \mu \right) \frac{\partial u_k}{\partial x_k} \delta_{ij} \right]$$
(35)

where the numerical operator,  $\partial_{x_j}$ , uses the staggered central difference scheme, and  $\partial_{x_i}$ , for  $i \neq j$ , is conducted via the collocated central difference scheme in a direction orthogonal to the flux component and interpolated to the staggered grid locations. Numerically, for  $\mu > 0$ , the first term on the right-hand side of Eq. (35) imposes the dominant dissipation. Based on the analysis shown in Fig. 2b and Fig. 7b, the spectral dissipation can be well represented by the staggered central difference schemes especially in the high-wavenumber regime. The Nyquist wavenumber features caused by the dispersion error and aliased interaction can be effectively damped following the diffusion mechanism in the governing equations. Similarly, the viscous flux in Eq. (25) can be rearranged to

$$\frac{\partial}{\partial x_j} \left[ u_i \sigma_{ij} - q_j \right] = \frac{\partial}{\partial x_j} \left( \mu u_i \frac{\partial u_i}{\partial x_j} + \kappa \frac{\partial T}{\partial x_j} \right) + \frac{\partial}{\partial x_j} \left[ \mu u_i \frac{\partial u_j}{\partial x_i} + \left( \beta - \frac{2}{3} \mu \right) \frac{\partial u_k}{\partial x_k} u_j \right]$$
(36)

where the term  $\mu u_i u_{i,j}$  can be interpreted as an alternative evaluation of  $\mu(u_i u_i/2)_{.j}$ . The advantage of the staggered formulation can be observed from the first term on the right-hand side of Eq. (36). Additionally, the remaining terms, particularly the ones associated with the bulk viscosity,  $\beta$ , in Eq. (35) and Eq. (36) partially benefit from the high-wavenumber spectral behavior of the staggered central difference schemes.

#### 3.3. Formulations on curvilinear meshes

The numerical differential operations on a curvilinear mesh are conducted based on an invertible mapping taking the coordinates on the curvilinear mesh to coordinates on a uniform Cartesian mesh. In this work, the mapping is assumed to be time-independent. The space where the curvilinear mesh is defined is known as the physical domain or actual domain, while the space where the Cartesian mesh is established is known as the reference domain or computational domain. In a three-dimensional physical domain, the orthonormal basis is defined using  $\hat{e}_x$ ,  $\hat{e}_y$  and  $\hat{e}_z$ , and the coordinates can be expressed as  $\mathbf{x} = x\hat{e}_x + y\hat{e}_y + z\hat{e}_z$ . Correspondingly, in the reference domain, the orthonormal basis is defined as  $\hat{e}_\xi$ ,  $\hat{e}_\eta$  and  $\hat{e}_\zeta$ , and the coordinates can be expressed as  $\boldsymbol{\xi} = \xi\hat{e}_\xi + \eta\hat{e}_\eta + \zeta\hat{e}_\zeta$ . During the solution process, the governing equations formulated in the physical domain are first mapped to the reference domain so that the numerical differential operations can be applied. Then, the evaluated results are mapped back to the physical domain. The mapping of the differential operations between the paired physical and reference domains are established by the metric tensors that are defined as follows.

$$F_{iA} = \frac{\partial x_i}{\partial \xi_A}$$
 and  $g_{Ai} = \frac{\partial \xi_A}{\partial x_i}$  (37, 38)

where the uppercase subscript represents the dimension in the reference domain, and the lowercase subscript represents the dimension in the physical domain [51]. It can be seen from the definitions that both  $F_{iA}$  and  $g_{Ai}$  are "two-leg" tensors.  $g_{Ai}$  maps the differential operation from the physical domain to the reference domain,  $d\xi_A = g_{Ai} dx_i$ , and  $F_{iA}$  maps the differential operation from the reference to the physical domain,  $dx_i = F_{iA} d\xi_A$ . A schematic is shown in Fig. 12. The Jacobian of the metrics, J, is defined as the determinant of the metric tensor F.

$$J = \det(F) \tag{39}$$

which characterizes the volume mapping from the reference domain to the physical domain,  $dxdydz = Jd\xi d\eta d\zeta$ . Since the mapping is invertible, the identity  $F = g^{-1}$  holds. In addition, for a valid computational mesh, the condition J > 0 must be satisfied.

Consider the following weak scalar conservation law formulated in the physical domain.

$$\frac{\partial \phi}{\partial t} + \frac{\partial G_j}{\partial x_i} = \omega \tag{40}$$

where  $\phi$  is a scalar conservative variable;  $G_j$  is the physical flux; and  $\omega$  is the source / sink. The mapped flux divergence in the reference domain is

$$J\frac{\partial G_j}{\partial x_j} = \frac{\partial G_j F_{jA}^*}{\partial \xi_A} \tag{41}$$

where  $F^* = JF^{-T}$  is the cofactor tensor of F. Therefore, an equivalent formulation of Eq. (40) in the reference domain is

$$\frac{\partial J\phi}{\partial t} + \frac{\partial \hat{G}_A}{\partial \xi_A} = J\omega \tag{42}$$

where  $\widehat{G}_A$  is known as the contravariant flux, defined as

$$\hat{G}_A = G_j \tilde{g}_{jA}^{\mathrm{T}} \tag{43}$$

The notation  $(\widetilde{\cdot}) = J(\cdot)$  in Eq. (43) is introduced for shorthand such that  $\widetilde{g}_{jA}^T = Jg_{jA}^T$ . Also, in accordance with the definitions, the identity  $F^* = \widetilde{g}^T$  holds. Analogously, the compressible Navier-Stokes equations, Eq. (23), Eq. (24) and Eq. (25), can be reformulated as follows.

$$\frac{\partial J\rho}{\partial t} + \frac{\partial}{\partial \xi_A} \left( \rho \widehat{U}_A \right) = 0 \tag{44}$$

$$\frac{\partial J \rho u_i}{\partial t} + \frac{\partial}{\partial \xi_A} \left( \rho u_i \hat{U}_A + p \tilde{g}_{iA}^{\mathrm{T}} \right) = \frac{\partial}{\partial \xi_A} \left( \sigma_{ij} \tilde{g}_{jA}^{\mathrm{T}} \right) \tag{45}$$

$$\frac{\partial J\rho e}{\partial t} + \frac{\partial}{\partial \xi_A} \left( \rho h \widehat{U}_A \right) = \frac{\partial}{\partial \xi_A} \left[ \left( u_i \sigma_{ij} - q_j \right) \widetilde{g}_{jA}^{\mathrm{T}} \right] \tag{46}$$

where  $\widehat{U}_A$  is known as the contravariant velocity defined as

$$\hat{U}_A = u_i \tilde{g}_{iA}^{\mathrm{T}} \tag{47}$$

The numerical evaluation of the contravariant fluxes follows an approach similar to that used for the uniform Cartesian mesh described in Sec. 3.2. The primitive variables,  $u_i$ , p and T, are interpolated from the collocated grid points to the staggered grid points to assemble the inviscid contravariant fluxes that appear on the left-hand sides of Eq. (44), Eq. (45) and Eq. (46). The transfer function of the interpolation schemes still contributes to the robustness by reducing high-wavenumber oscillations before any nonlinear interactions. The viscous contravariant fluxes that appear on the right-hand sides of Eq. (44), Eq. (45), and Eq. (46) are assembled based on the interpolated primitive variables and gradient fields with respect to the physical coordinate system that are evaluated using chain rule,  $\partial_{x_j} = \left(\partial_{\xi_B}\right) g_{Bj}$  or  $\partial_{x_j} = g_{jB}^T \partial_{\xi_B}$ . The divergence operations in the reference domain are conducted using the staggered difference schemes. The gradient components in the reference domain aligned with the contravariant flux direction are also evaluated using the staggered difference schemes. As a result, substituting the expressions of  $\sigma_{ij}$  and  $q_j$ , the viscous contravariant fluxes in Eq. (46) are evaluated as follows.

$$\frac{\partial}{\partial \xi_{A}} \left( \sigma_{ij} \widetilde{g}_{jA}^{\mathrm{T}} \right) = \frac{\partial}{\partial \xi_{A}} \left( \mu \frac{\partial u_{i}}{\partial \xi_{B}} g_{Bj} \widetilde{g}_{jA}^{\mathrm{T}} \right) + \frac{\partial}{\partial \xi_{A}} \left[ \mu g_{iB}^{\mathrm{T}} \frac{\partial u_{j}}{\partial \xi_{B}} \widetilde{g}_{jA}^{\mathrm{T}} + \left( \beta - \frac{2}{3} \mu \right) \frac{\partial u_{k}}{\partial \xi_{B}} g_{Bk} \widetilde{g}_{iA}^{\mathrm{T}} \right]$$

$$(48)$$

$$\frac{\partial}{\partial \xi_{A}} \left[ \left( u_{i} \sigma_{ij} - q_{j} \right) \widetilde{g}_{jA}^{\mathrm{T}} \right] = \frac{\partial}{\partial \xi_{A}} \left[ \left( \mu u_{i} \frac{\partial u_{i}}{\partial \xi_{B}} + \kappa \frac{\partial T}{\partial \xi_{B}} \right) g_{Bj} \widetilde{g}_{jA}^{\mathrm{T}} \right] + \frac{\partial}{\partial \xi_{A}} \left[ \mu u_{i} g_{iB}^{\mathrm{T}} \frac{\partial u_{j}}{\partial \xi_{B}} \widetilde{g}_{jA}^{\mathrm{T}} + \left( \beta - \frac{2}{3} \mu \right) \frac{\partial u_{k}}{\partial \xi_{B}} g_{Bk} u_{i} \widetilde{g}_{iA}^{\mathrm{T}} \right]$$

$$(49)$$

For a valid mapping,  $g_{Bj}\widetilde{S}_{jA}^T$  is symmetric and positive-definite in the reference domain. Using the staggered central difference schemes for  $\partial_{\xi_A}$ , the dissipation of high-wavenumber oscillations in the reference domain can still be effectively resolved. The differential operator,  $\partial_{\xi_B}$ , for  $B \neq A$ , is evaluated using the collocated central difference scheme and then interpolated to the staggered grid points.

#### 3.4. Generation of metrics

The metric tensor used to assemble the contravariant fluxes is  $\widetilde{g}$ . Analytically, it can be calculated by inverting F.

$$\widetilde{g}_{iA}^{T} = \left(\frac{1}{2}\epsilon_{ijk}\epsilon_{ABC}\right)\frac{\partial x_{j}}{\partial \xi_{B}}\frac{\partial x_{k}}{\partial \xi_{C}} \tag{50}$$

where  $\varepsilon_{ijk}$  and  $\varepsilon_{ABC}$  are Levi-Civita permutation tensors in the physical and reference domains respectively. However, Eq. (50) cannot be directly used to generate metrics for a numerical solver as noted in Ref. [45]. Consider a homogeneous steady-state solution to

Eq. (40), where  $\omega = 0$  and both  $\phi$  and  $G_j$  are constant in space and time. In the reference domain, Eq. (42), combined with Eq. (43), reduces to the following constraint.

$$\frac{\partial \widetilde{g}_{iA}^{\mathrm{T}}}{\partial \xi_{A}} = 0 \tag{51}$$

Eq. (51) is known as the GCL for a stationary curvilinear mesh [45]. In this work, the GCL is further discussed from an alternative perspective.

On one hand, the GCL indicates a consistency between the numerical divergence operator and the generation of the discrete metric tensor as described in many works [45–47]. On the other hand, it also reveals numerical enforcement of a compatibility condition of the metrics. The metric tensor F can be interpreted as a type of "deformation gradient" of the physical coordinates with respect to the reference coordinates, i.e.,  $F^T = \nabla_\xi x^T$ , where the gradient operator with respect to the reference coordinates is defined as  $\nabla_\xi = \partial_{\xi_A}$ . As an identity,  $F^T$  is "curl-free" on the reference domain, i.e.,  $\nabla_\xi \times F^T = 0$ . This is known as compatibility of the metric tensor. Taking a divergence operation with respect to the reference coordinates on both sides of Eq. (50), the following equation can be obtained.

$$\frac{\partial \widetilde{g}_{1A}^{T}}{\partial \xi_{A}} = \frac{1}{2} \varepsilon_{ijk} \left[ \frac{\partial x_{k}}{\partial \xi_{C}} \left( \varepsilon_{ABC} \frac{\partial}{\partial \xi_{A}} \frac{\partial x_{j}}{\partial \xi_{B}} \right) + \frac{\partial x_{j}}{\partial \xi_{B}} \left( \varepsilon_{ABC} \frac{\partial}{\partial \xi_{A}} \frac{\partial x_{k}}{\partial \xi_{C}} \right) \right]$$
(52)

where the expression in the brackets on the right-hand side yields  $F\left(\nabla_{\xi}\times F^{T}\right)-\left(\nabla_{\xi}\times F^{T}\right)^{T}F^{T}$ . The right-hand side of Eq. (52) is identically zero due to the compatibility if all differential operations are exact. However, for numerically-approximated derivative operations, the left-hand side and right-hand side of Eq. (52) are not discretely equivalent. The "curl-free" condition of  $F^{T}$  is weakly imposed in  $\widetilde{g}^{T}$ , which relies on numerical consistency and is achieved by grid convergence. This is due to the nonlinearity in evaluating  $\widetilde{g}^{T}$  from F. The product rule of calculus may not hold discretely to enforce a numerically equivalent form of the right-hand side in Eq. (52). As a result, a non-zero residual may be generated from the truncation errors of the numerical schemes. Such a residual is known as the GCL error and often contributes to numerical inaccuracy and instability in simulations of physical conservation laws [46,52].

For numerically-generated metrics, the commonly used approaches are equivalent to strongly imposing the compatibility condition in Eq. (50). In order to show this, append two terms that are analytically equal to zero,  $x_j \varepsilon_{ABC} F_{kC,B}$  and  $x_k \varepsilon_{ABC} F_{jB,C}$ , to the right-hand side of Eq. (50), so that the expression of  $\widetilde{g}_{jA}^T$  becomes compatibility-aware.

$$\widetilde{g}_{iA}^{T} = \left(\frac{1}{2}\varepsilon_{ijk}\varepsilon_{ABC}\right) \left[\frac{\partial x_j}{\partial \xi_B} \frac{\partial x_k}{\partial \xi_C} + wx_j \frac{\partial}{\partial \xi_B} \frac{\partial x_k}{\partial \xi_C} + (1 - w)x_k \frac{\partial}{\partial \xi_C} \frac{\partial x_j}{\partial \xi_B}\right]$$
(53)

where w is a weighting factor. Eq. (53) can be further analytically manipulated into the so-called conservation form [45].

$$\widetilde{g}_{iA}^{T} = \left(\frac{1}{2}\varepsilon_{ijk}\varepsilon_{ABC}\right) \left[ w \frac{\partial}{\partial \xi_{B}} \left( x_{j} \frac{\partial x_{k}}{\partial \xi_{C}} \right) + (1 - w) \frac{\partial}{\partial \xi_{C}} \left( x_{k} \frac{\partial x_{j}}{\partial \xi_{B}} \right) \right] \tag{54}$$

The effect of the weighting factor w is discussed in detail in Ref. [53]. For further discussion, rewrite Eq. (54) as

$$\widetilde{g}_{iA}^{T} = \left(\frac{1}{2} \varepsilon_{ijk} \varepsilon_{ABC}\right) \left[ w \frac{\partial}{\partial \xi_{R}} \left( x_{j} F_{kC} \right) - (1 - w) \frac{\partial}{\partial \xi_{R}} \left( x_{k} F_{jC} \right) \right]$$
(55)

Comparing Eq. (55) with Eq. (51), the GCL error can be expressed as

$$\frac{\partial \widetilde{g}_{iA}^{\mathrm{T}}}{\partial \xi_{A}} = \left(\frac{1}{2} \varepsilon_{ijk} \varepsilon_{ABC}\right) \left[ w \frac{\partial^{2}}{\partial \xi_{A} \partial \xi_{B}} \left( x_{j} F_{kC} \right) - (1 - w) \frac{\partial^{2}}{\partial \xi_{A} \partial \xi_{B}} \left( x_{k} F_{jC} \right) \right]$$
(56)

The GCL constraint, derived by imposing compatibility, is satisfied by fully relying on the commutativity of the differential operators used for divergence evaluation in the computational framework,  $\partial_{\xi_A}$ , and in the numerical calculation of  $\widetilde{g}^T$  from F,  $\partial_{\xi_B}$ . Accordingly, once  $x \otimes F$  is assembled, the GCL requires the remaining differential operations to calculate  $\widetilde{g}^T$  to be consistent and commutable. However, the GCL constraint does not put any restriction on the calculation of F. This implies that F can be either numerically evaluated in different ways or analytically provided. Similarly, prior to calculations of  $x \otimes F$ , there is no GCL constraint for the evaluation of x either if its components are needed at an abstract location. In practice, as an example,  $x \otimes F$  is evaluated at collocated grid points and then interpolated to the edge-staggered locations in Ref. [47], while in this work, F and F are evaluated from an interpolated F0 with F1 are evaluated from an interpolated F2 with F3 are evaluated by Eq. (55) should be interpreted as a GCL-consistent inversion of the metric tensor F3.

In this work, the metric tensor is fully calculated by numerical differentiation for all cases following Eq. (54) with w = 0.5. All numerical differential operations are conducted by the edge-to-node staggered finite difference methods. Assuming that the physical coordinates are initially provided at the collocated grid points during mesh generation, all coordinates are first interpolated along all three directions to a fully staggered location. In the reference domain, the fully staggered location is at the geometric center of the cube constructed by the neighboring collocated points as shown in Fig. 13. Starting from the fully staggered locations, all components in the metric tensor F are numerically evaluated at the corresponding face-staggered locations. Then, the corresponding components of  $x \otimes F$  are assembled at the face-staggered locations. Eventually, after the second differential operation, the GCL-consistent metrics

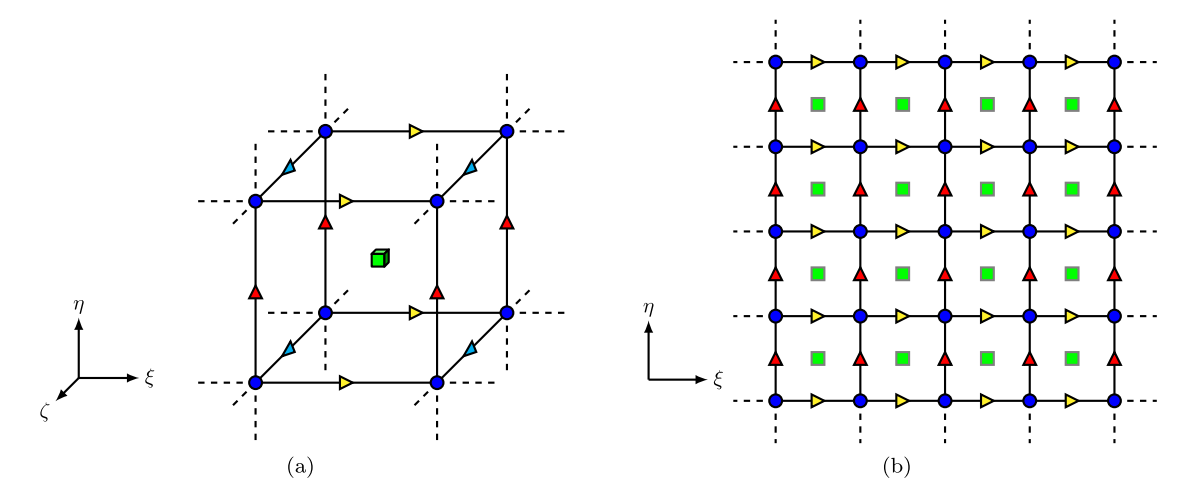


**Fig. 13.** Schematics of GCL metrics generation: (a) detailed isometric view of the three-dimensional structure; (b) projected view on the  $\xi - \eta$  plane where fully staggered locations do not belong to the collocated and edge-staggered plane. The mesh is shown in the reference domain. The collocated, edge-staggered and fully staggered points are marked by circle, triangle and square (cube) symbols, respectively.

are obtained at each edge-staggered location for the assembly of contravariant inviscid fluxes. At these locations, other components of  $\tilde{g}^T$  that are not involved in the GCL constraint are calculated via interpolations. For a periodic domain, specific details of metric evaluations using staggered compact finite difference and midpoint interpolation schemes are given in Appendix C.

#### 3.5. Shock-capturing methods

In simulations of flows where shock waves are present, the shock waves are often treated as under-resolved structures. For high-resolution simulations, high-order shock-capturing schemes are commonly applied [37,54,55]. These shock-capturing schemes impose sufficient numerical dissipation at shock locations so that the shock profiles are artificially thickened and well-captured discretely by the computational framework without causing numerical instability or strong spurious oscillations. The computational framework described in previous sub-sections is compatible with a wide variety of shock-capturing techniques. In this work, two common methods – the localized artificial diffusivity (LAD) method and the weighted essentially non-oscillatory (WENO) interpolation scheme combined with a projected approximate Riemann solver – are investigated.

For weak and moderate eddy shocklets in compressible turbulent flows, the LAD approach performs decently. The LAD approach is known to be less dissipative for simulations of turbulent flows when used with numerical operators that have high-spectral-resolution properties. For shock-capturing, only artificial bulk viscosity and artificial thermal conductivity are needed. The LAD model detects a shock based on local high-order derivatives. The detailed formulation is described in Ref. [37]. LAD can be easily applied to a computational system combined with diffusive fluxes. It does not require characteristic decomposition or a Riemann solver. Instead, according to Ref. [37], a low-pass filter is required to maintain numerical stability. However, in this computational framework, due to the robustness resulting from dealiasing effects and high-wavenumber viscous dissipation enhancement, the solution filtering, claimed to be necessary in previous applications of LAD models, can be avoided in capturing weak shocks. Furthermore, without solution filtering, the numerical dissipation due to the spatial discretization, exerted in the computational system can be easily quantified.

WENO-based nonlinear interpolation schemes divide a full stencil into several candidate sub-stencils. Each candidate sub-stencil interpolates the input field individually using a linear scheme whose order of convergence is supported by the width of the sub-stencil. The final interpolated results are determined via a convexly-weighted superposition of all results obtained from candidate sub-stencils. The weights are comprehensively determined by a set of smoothness indicators calculated on each candidate sub-stencil. In a smooth region, the weights tend to make the superposed coefficients converge to a high-order linear interpolation scheme. In a shock region, the weights impose the use of interpolations from locally smooth candidate sub-stencils only. Correspondingly, the formal order of convergence will be lower.

For better solution behavior, the nonlinear interpolation scheme is commonly applied in conjunction with an approximate Riemann solver [55]. A Riemann solver assumes a discontinuity at the flux assembly location and takes two states of conservative variables on both sides of the discontinuity to evaluate regularized fluxes as the Riemann problem develops in time. For a hyperbolic conservation system, Riemann fluxes can be calculated as  $\mathcal{F}_{\text{Riemann}}(U_L,U_R)$ , where  $\mathcal{F}_{\text{Riemann}}$  is the set of numerical fluxes evaluated by the Riemann solver, U is the set of conservative variables, and the subscripts "L" and "R" denote the "left" and "right" states respectively. In an actual simulation, each edge is assumed to formulate a projected local Riemann problem.  $U_L$  and  $U_R$  are obtained from the interpolated characteristic variables.

Even with nominally high-order methods, fully using nonlinear interpolation schemes may still result in overly dissipative solution profiles at small scales in simulations of turbulent flows; this phenomenon is shown in Sec. 4.4. Therefore, to conduct an LES or DNS at a comparable physical resolution, the computational mesh used for a simulation that fully relies on nonlinear interpolation schemes needs to be much finer than the mesh used for a simulation based on non-dissipative numerical methods. Nevertheless, shock-

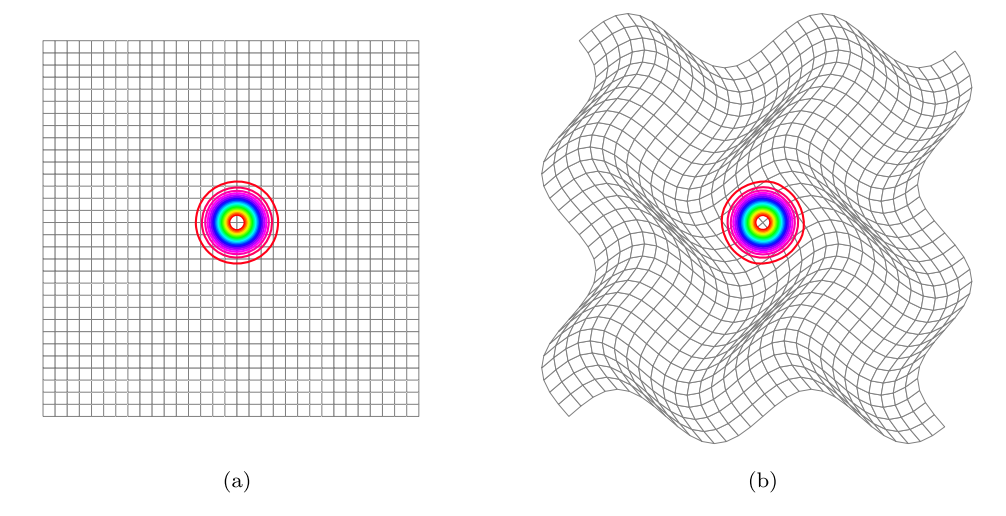


Fig. 14. Initial pressure distributions: (a) Cartesian mesh; (b) curvilinear mesh. The contours represent the pressure distributions for  $p \in [0.55, 0.71]$ .

capturing schemes must be active at shock locations. To address this issue, a hybrid approach can be applied [40]. Conceptually, the hybridization is controlled by a physics-based shock sensor. Ideally, the shock-capturing schemes are active and localized to the shock structures, and only non-dissipative schemes are used in shock-free regions. Accordingly, small-scale dynamics are fully governed by physical dissipation or physics-based SGS model dissipation, and this significantly enhances the simulation resolution.

The computational framework introduced in this study supports a variety of blending strategies. Among all feasible strategies, binary blending of primitive variables ( $\rho$ , u, T) is used in this work. Based on the compatibility constraint for approximate Riemann solvers, if  $U_L = U_R$ , then the Riemann solver does not introduce extra numerical dissipation. As a result, when both  $U_L$  and  $U_R$  are set to be variables interpolated by central schemes,  $\mathcal{F}_{\text{Riemann}}(U_L, U_R)$  is identical to directly assembled central fluxes. Details of the shock-capturing schemes are included in Appendix E.

## 4. Demonstrative numerical performance

In this section, demonstrative simulations are provided to investigate the numerical performance of the computational framework. The demonstrations are primarily selected to examine the capability of the framework to preserve large-scale flow structures, resolve turbulent structures at small scales, and support existing models for LES and shock capturing.

### 4.1. Advection of a homentropic swirl

A uniform background flow is prescribed along the *x*-direction at a Mach number of 0.5 on a two-dimensional periodic domain,  $(x, y) \in [-6, 6)^2$ . A swirling flow field is superposed as a homentropic perturbation. The flow is inviscid and without thermal diffusion. Assuming the perturbed region is sufficiently small relative to the overall physical domain, the swirl flow feature will advect following the freestream at a constant velocity. Considering the periodic boundaries, after a period, the initial flow profile should be asymptotically recovered. The initial homentropic perturbation profiles, denoted with a " $\delta$ " in front of each variable, are given as

$$\begin{cases} \delta \mathbf{u} = \epsilon r e^{\alpha(1-r^2)} \hat{\mathbf{e}}_I(\theta) \\ \delta T = -\epsilon^2 \frac{\gamma - 1}{4\alpha \gamma} e^{2\alpha(1-r^2)} \end{cases}$$
 (57)

where  $r^2 = x^2 + y^2$ ;  $\theta$  is the polar angle about (x,y) = (0,0);  $\hat{e}_l$  is a clock-wise tangential unit vector,  $\hat{e}_l(\theta) = \hat{e}_x \sin \theta - \hat{e}_y \cos \theta$ ;  $\epsilon = 0.3$  characterizes the perturbation amplitude; and  $\alpha = 1.2$  characterizes the spatial localization of the swirl flow. The value of  $\alpha$  used in this configuration allows the Gaussian profile to achieve spatial decay of  $\mathcal{O}(10^{-17}) \sim \mathcal{O}(10^{-19})$  from the domain center to the closest "boundary" point. With these ranges of spatial decay, the perturbation near the domain "boundary" can be treated as numerically zero compared to the perturbation amplitude near the center of the computational domain. Consequently, the non-smoothness caused by the periodic extension of a Gaussian profile can be neglected. The fluid is a calorically perfect gas. The ratio of specific heats is  $\gamma = 1.4$ , and the specific gas constant is R = 1. The speed of sound and density in the freestream state are used for normalization. Therefore, the overall velocity field is  $u = 0.5\hat{e}_x + \delta u$ , and the overall temperature field is  $T = (\gamma R)^{-1} + \delta T$ . The perturbation is homentropic, so  $p/\rho^{\gamma}$  remains constant over the entire domain [46,47,56].

The simulation is set up on both a Cartesian and a curvilinear mesh with size  $32 \times 32$  as shown in Fig. 14. The curvilinear mesh is generated via a two-dimensional perturbation on the Cartesian mesh. The coordinate mapping is

$$\begin{cases} x = L \left[ \xi / N_{\xi} - 1/2 - A \sin(4\pi\eta / N_{\eta}) \right] \\ y = L \left[ \eta / N_{\eta} - 1/2 + A \sin(4\pi\xi / N_{\xi}) \right] \end{cases}$$
(58)

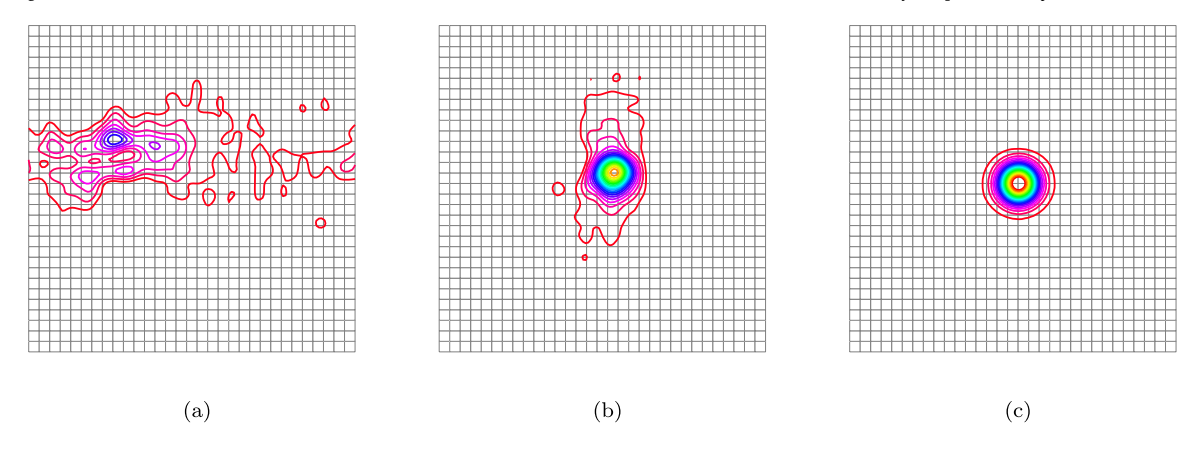


Fig. 15. Pressure distributions on a Cartesian mesh after one advection period: (a) second-order schemes; (b) fourth-order schemes; (c) compact sixth-order schemes. The contours represent the pressure distributions for  $p \in [0.55, 0.71]$ .

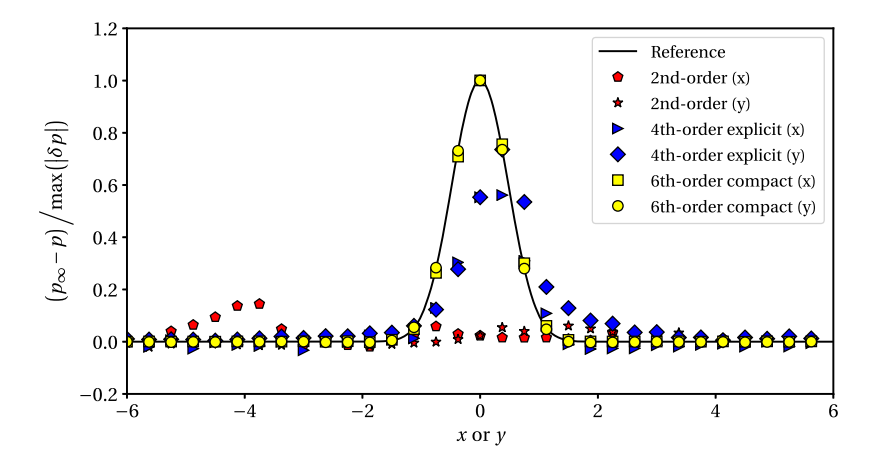


Fig. 16. Centerline pressure profiles after one advection period using different sets of spatial discretization schemes, where  $p_{\infty}$  is the freestream pressure, and  $\delta p$  is the pressure perturbation.  $p_{\infty}$ ,  $\delta p$  and the reference profile are analytically calculated from the initial condition.

where L=12 is the unperturbed domain length, and A=0.07 characterizes the mesh waviness. The mesh spacing in the reference domain is unity in both directions. The interpolation and differentiation with respect to the coordinates that use compact schemes to calculate GCL-consistent metrics on a periodic domain are illustrated in Appendix C. Time advancement is carried out using the third-order strong-stability-preserving Runge-Kutta (SSP-RK3) method [57] with a constant Courant–Friedrichs–Lewy (CFL) number of 0.4. Spatial computations are conducted using the same framework as previously described with second-order explicit, fourth-order explicit, and sixth-order compact central schemes respectively. All three sets of numerical schemes are non-dissipative.

The simulation results using different spatial discretization schemes on the Cartesian mesh are shown in Fig. 15. The contours represent the pressure profile for  $p \in [0.55, 0.71]$ . For visualization purposes, the simulation results are upsampled using the cubic spline method during post-processing. Compared with the reference profile given in Fig. 14a, after one advection period, the flow structures in the second-order simulation are completely distorted (Fig. 15a); significant numerical errors can be observed in the fourth-order simulations, but the basic flow structures are preserved (Fig. 15b); and almost no error is visible from the contours of the simulation using the sixth-order compact schemes (Fig. 15c). The centerline pressure profiles for the three simulation cases are shown in Fig. 16. As seen from the mesh generation, Eq. (58) for A = 0, the centerlines in both directions are aligned with a row or column of collocated grid points while using even  $N_{\xi}$  and  $N_{\eta}$ . Therefore, the data points in Fig. 16 represent the nodal values directly computed in the simulations. The reference profile is analytically calculated from the initial conditions, and the profile is normalized by the maximum pressure perturbation in the initial condition. According to the centerline profiles after one advection period, the sixth-order simulation best preserves the center location, profile shape, and the peak value. As a further investigation of the performance of the sixth-order compact schemes, the simulation is continued up to 15 advection periods. Some visualizations at selected numbers of advection periods are shown in Fig. 17. As the simulation time progresses, the numerical error accumulates and behaves as nonlinear dispersion. With this simulation setup, the computational accuracy can be well-preserved up to 11 advection periods. Beyond that, the numerical error begins to spread out, and the flow structures are more contaminated.

The simulation results on the curvilinear mesh are shown in Fig. 18. The results are obtained after one advection period, and Fig. 14b should be used for comparison. As shown in Eq. (44) – Eq. (46), the mesh waviness creates extra nonlinearity in the computational system which makes the simulations more challenging. As shown in Fig. 18a, the second-order simulation completely

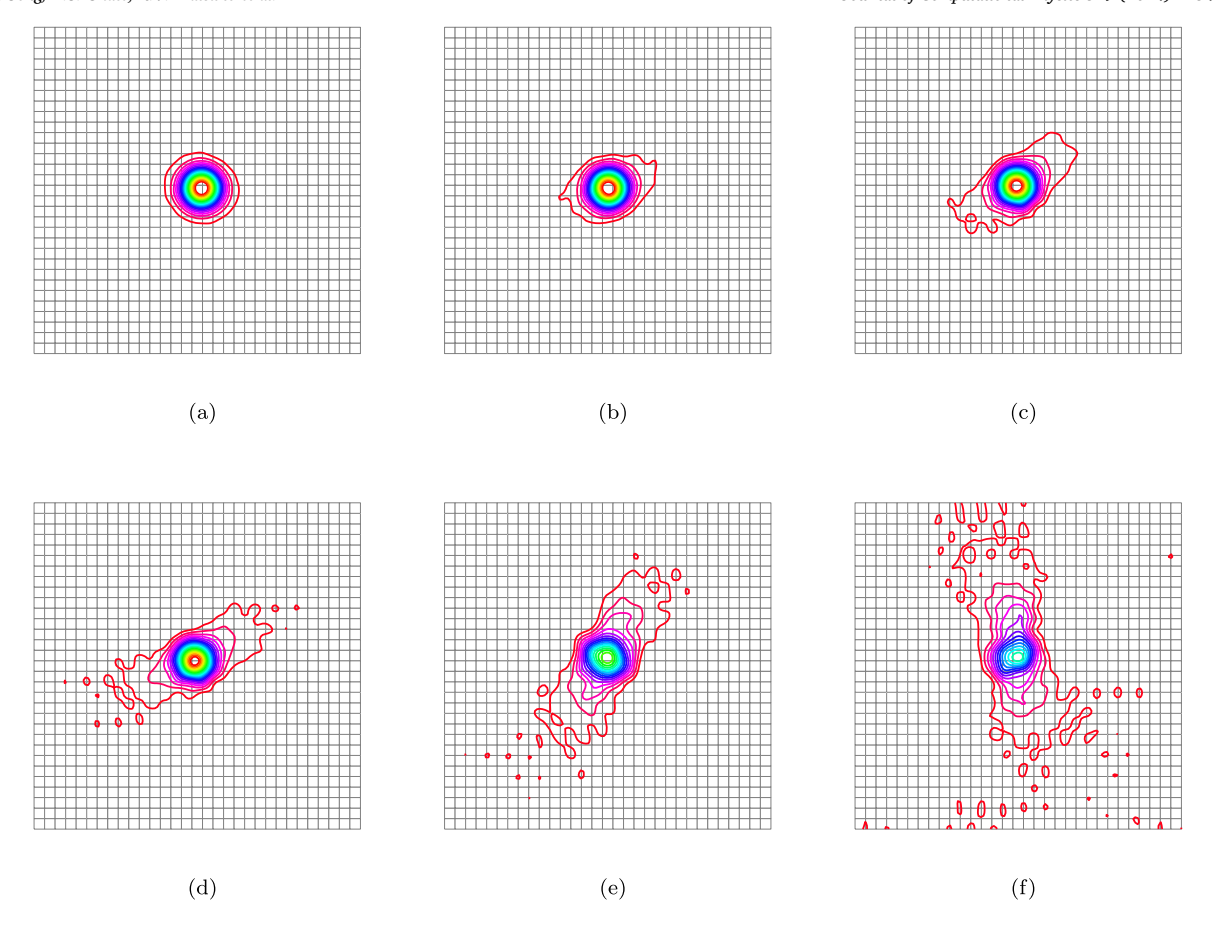


Fig. 17. Pressure distribution on Cartesian mesh using sixth-order compact schemes after (a) 5 advection periods; (b) 8 advection periods; (c) 11 advection periods; (d) 12 advection periods; (e) 14 advection periods; and (f) 15 advection periods.

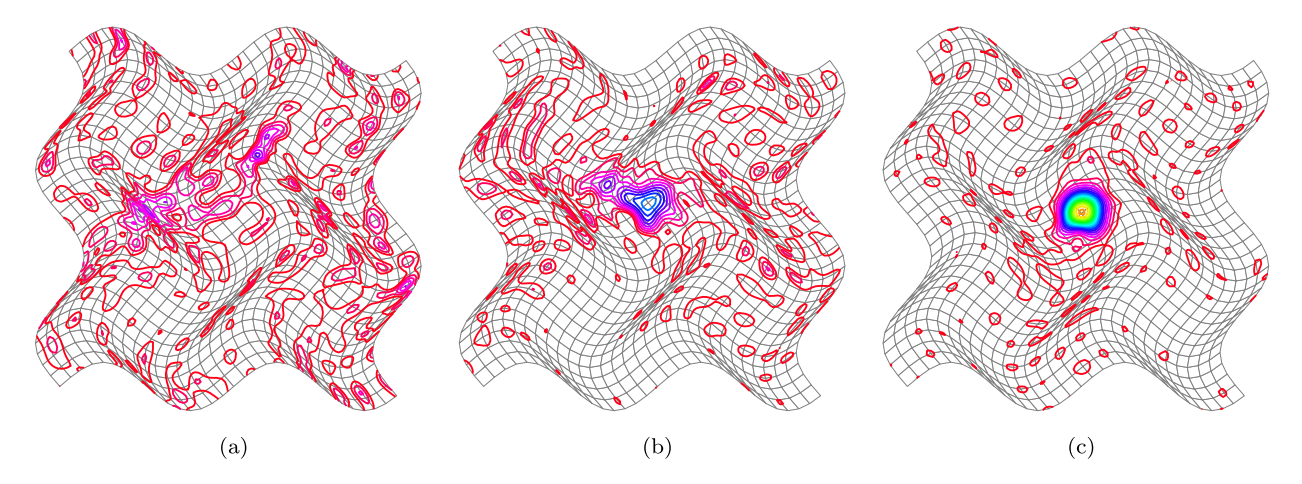
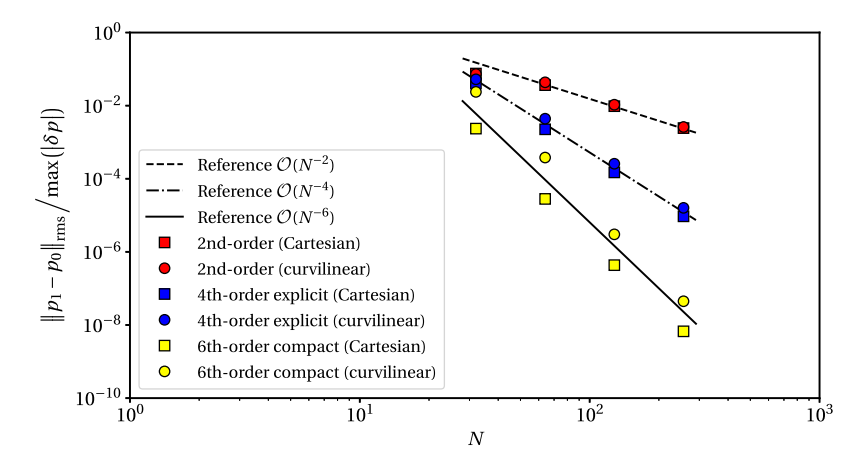


Fig. 18. Pressure distributions on a curvilinear mesh after one advection period: (a) second-order schemes; (b) fourth-order schemes; (c) sixth-order compact schemes.

destroys the flow features, and the numerical error is especially localized where the mesh is largely skewed. The flow features in the fourth-order simulation (Fig. 18b) are also significantly distorted, but a small number of the original features can still be identified from the resulting field. The compact sixth-order simulation (Fig. 18c) preserves majority of the flow features and gives the best result among the three simulations although the numerical solution in the freestream region is highly contaminated.

The grid convergence for all sets of simulations shown in this section is measured. In order to reduce the numerical error caused by the time advancement scheme, the CFL number is set to 0.05. For all cases, the solution profiles at one advection period are used to evaluate the numerical error. The numerical error is quantified by the root-mean-square pressure difference between the final state



**Fig. 19.** Grid convergence measurements of the homentropic swirl advection simulations using different sets of numerical schemes. *N* represents the number of grid points in each dimension, and the numerical error is indicated by the root-mean-square pressure difference between the initial condition and one advection period and is normalized by the maximum initial pressure perturbation.

and initial condition that is analytically set. The numerical error is further scaled by the maximum perturbation pressure in the initial condition. The results are shown in Fig. 19 where N is the number of grid points in each dimension. Compared to the reference curves in Fig. 19, all simulations achieve the expected formal orders of convergence on both a uniform Cartesian mesh and a curvilinear wavy mesh.

#### 4.2. Forced isotropic turbulence

This problem is configured on a three-dimensional periodic domain,  $(x, y, z) \in [0, 2\pi)^3$ , with a setup similar to the one described in Ref. [8]. An isotropic turbulent flow is energized by a low-wavenumber solenoidal term,  $\rho f_i$ , added to the right-hand side of Eq. (24). Eq. (25) remains unmodified, which implies the existence of an internal energy sink,  $\Lambda$ , that locally and instantaneously balances the forcing work,  $\Lambda + \rho f_i u_i = 0$ . The forcing,  $f_i$ , is updated via a solenoidally projected stochastic process [58] as expressed in Eq. (59),

$$f_i = \sum_{k_L \le k \le k_H} \mathcal{P}_{ij}^\perp \widehat{b}_j(k_m, t) e^{ik_m x_m} \tag{59}$$

where  $k_L=3$  and  $k_H=5$  are the cut-off wavenumbers defining a forcing band;  $k=\sqrt{k_m k_m}$  is the magnitude of the wavenumber vector;  $\mathcal{P}_{ij}^\perp = \delta_{ij} - k_i k_j / k^2$  is a solenoidal projector; and  $\hat{b}_j \in \mathbb{C}^3$  for each mode is updated using six independent Uhlenbeck-Ornstein random processes. The fluid is a calorically perfect gas with  $\gamma=1.4$ . The dynamic viscosity is calculated based on a power law,  $\mu=\mu_{\rm ref}(T/T_{\rm ref})^{0.5}$ , where the subscript "ref" represents a reference state. The thermal conductivity is calculated based on the Prandtl number,  $\Pr=c_p\mu/\kappa$ , where  $c_p=\gamma R/(\gamma-1)$  is the specific heat at a constant pressure. In this simulation, the Prandtl number remains constant at  $\Pr=0.72$ . The fluid is assumed to have no physical bulk viscosity.

The computational mesh size is  $1024 \times 1024 \times 1024$ . The simulation is conducted using sixth-order compact schemes with the artificial bulk viscosity,  $\beta^*$ , and artificial thermal conductivity,  $\kappa^*$ , added to the physical bulk viscosity and thermal conductivity respectively for eddy shocklet capturing. The formulations of  $\beta^*$  and  $\kappa^*$  are described in Ref. [37]. However, in this simulation, no solution filtering is applied. The time advancement is calculated using the standard fourth-order Runge-Kutta (RK4) method with CFL = 0.5. The simulation data over a period of seven eddy turnover times is used in post-processing after the flow has reached a statistically stationary state.

The visualizations of the instantaneous flow fields are shown in Fig. 20. The stationary isotropic turbulence is resolved in the DNS regime with  $k_{\max} \eta \approx 3.2$  where  $k_{\max}$  is the maximum wavenumber supported by the computational mesh, and  $\eta$  is known as the Kolmogorov length scale. In this case,  $\eta$  is calculated as  $\eta = (\langle \mu \rangle^3 \langle \epsilon \rangle^{-1} \langle \rho \rangle^{-2})^{1/4}$ , where the angle bracket,  $\langle (\cdot) \rangle$ , denotes a volume average, and  $\epsilon$  is the dissipation rate,  $\epsilon = 2\mu S_{ij}S_{ij} + (\beta^* - 2\mu/3)S_{kk}^2$ . The velocity energy spectrum is provided in Fig. 21 where  $E_k$  is defined as  $E_k = \hat{u}_j \hat{u}_j^*/2$  in continuous Fourier space for an infinite domain. Using the discrete Fourier transform on a finite periodic domain,  $E_k$  is evaluated as  $E_k = 4\pi k^2 \left\langle \hat{u}_j \hat{u}_j^*/2 \right\rangle_k$ , where the operator,  $\langle (\cdot) \rangle_k$ , indicates the average within a sampling bin centered at k. The distributions of velocity dilatation,  $\theta = u_{j,j}$ , and local Mach number,  $\sqrt{u_j u_j}/c$ , are shown in Fig. 22 where the function

at k. The distributions of velocity dilatation,  $\theta = u_{j,j}$ , and local Mach number,  $\sqrt{u_j u_j}/c$ , are shown in Fig. 22 where the function "std(·)" returns the standard deviation. The two-point correlations of each velocity component are also provided in Fig. 23 to improve confidence in the computational results, and the two-point correlations,  $R_{ii} = \langle u_i(x)u_i(x+r)\rangle/\langle u_i(x)u_i(x)\rangle$ , are calculated using the discrete Fourier transform. Here, the subscript indices for  $R_{ii}$  do not follow the summation convention.

According to the post-processing, the demonstrative simulation has  $\text{Re}_{\lambda} \approx 162$  and  $M_t \approx 0.7$ , where  $\text{Re}_{\lambda}$  is the characteristic Reynolds number based on the Taylor micro-scale,  $\lambda$ , and  $M_t$  is known as the turbulent Mach number. For isotropic turbulence,  $\text{Re}_{\lambda}$ 

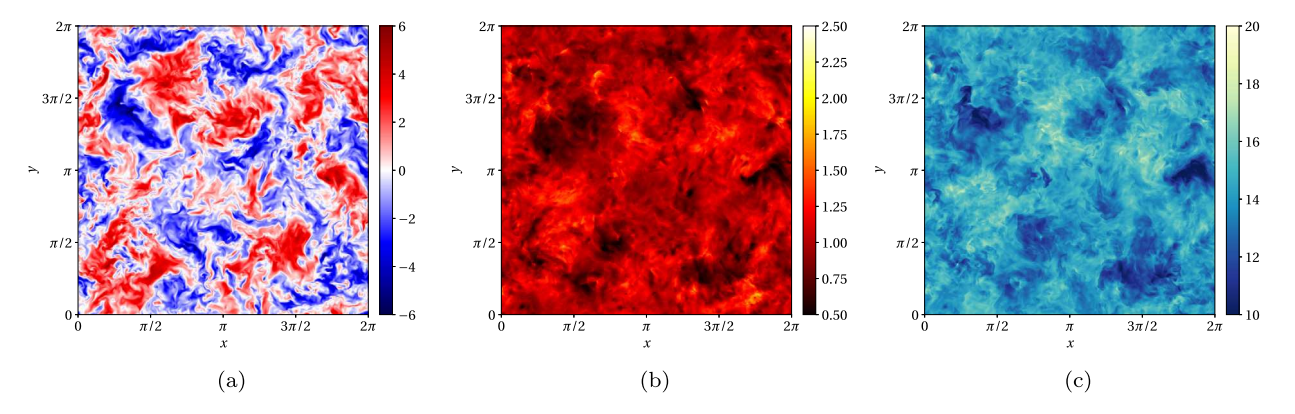


Fig. 20. Visualization of flow fields: (a) z-velocity; (b) density; (c) pressure.

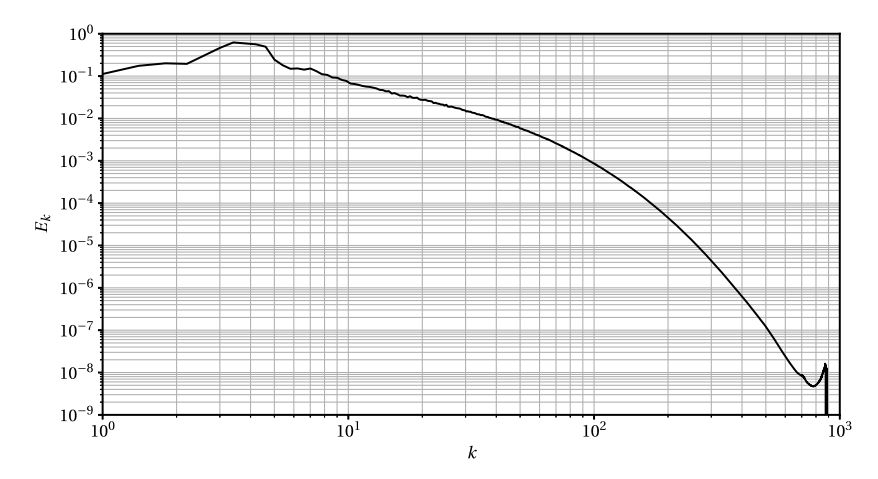


Fig. 21. Velocity energy spectrum.

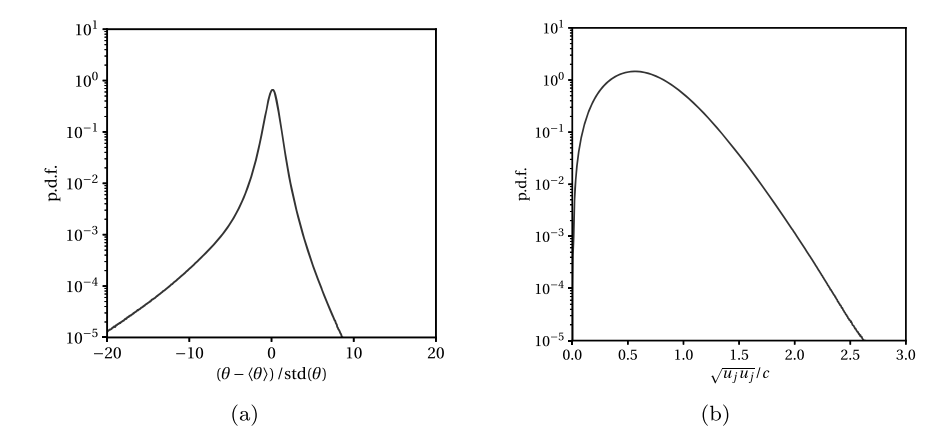


Fig. 22. Normalized probability density functions of (a) velocity dilatation and (b) local Mach number.

and  $M_t$  are calculated as  $\text{Re}_{\lambda} = u_{\text{rms}} \lambda / \langle v \rangle$  and  $M_t = \sqrt{\langle u_j u_j \rangle / \langle c \rangle}$  respectively, where  $u_{\text{rms}}$  and  $\lambda$  are calculated as  $u_{\text{rms}} = \sqrt{\langle u_j u_j \rangle / 3}$  and  $\lambda = \sqrt{\langle u^2 \rangle / \langle (\partial u / \partial x)^2 \rangle}$  respectively.

The value of  $M_t$  measured from this simulation indicates that the turbulence is highly compressible [3]. Fig. 24 shows the visualization of the shocklet distribution and the relative profiles of  $\beta^*$  and  $\kappa^*$ . The shocklets are visualized using a modified Ducros sensor, defined as  $-\theta|\theta|/\left[\theta^2+\omega_j\omega_j+10^{-32}\right]$ , where  $\theta=u_{j,j}$  is the velocity dilatation, and  $\omega_i=\varepsilon_{ijk}u_{k,j}$  is the vorticity. With this sensor, a shock is identified since the sensor value is close to +1. Compared with Fig. 24a, the instantaneous spatial distributions of  $\beta^*$  and  $\kappa^*$  are highly localized at the eddy shocklet structures, as shown in Fig. 24c and Fig. 24b respectively, to provide sufficient

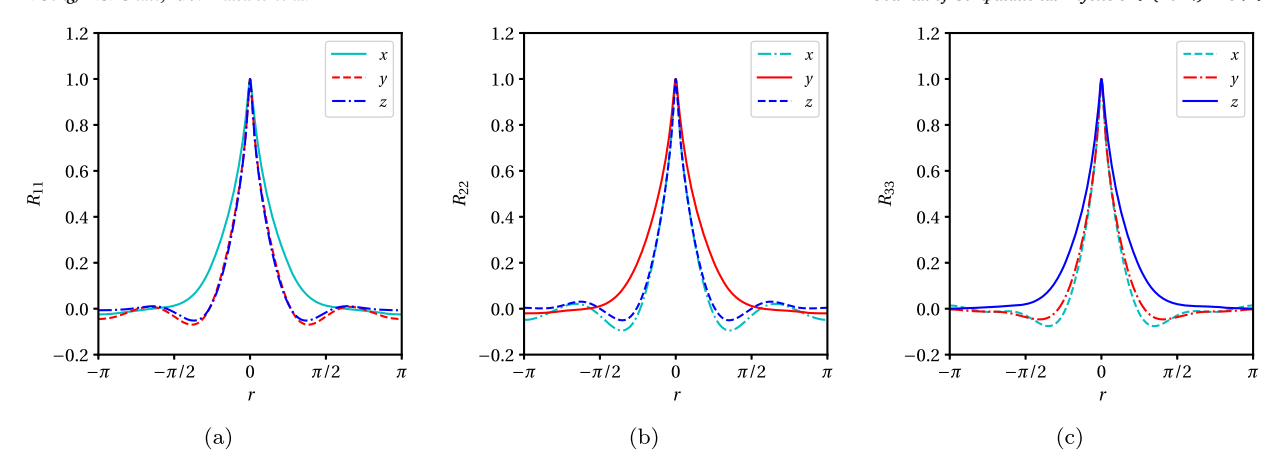


Fig. 23. Velocity two-point correlation.

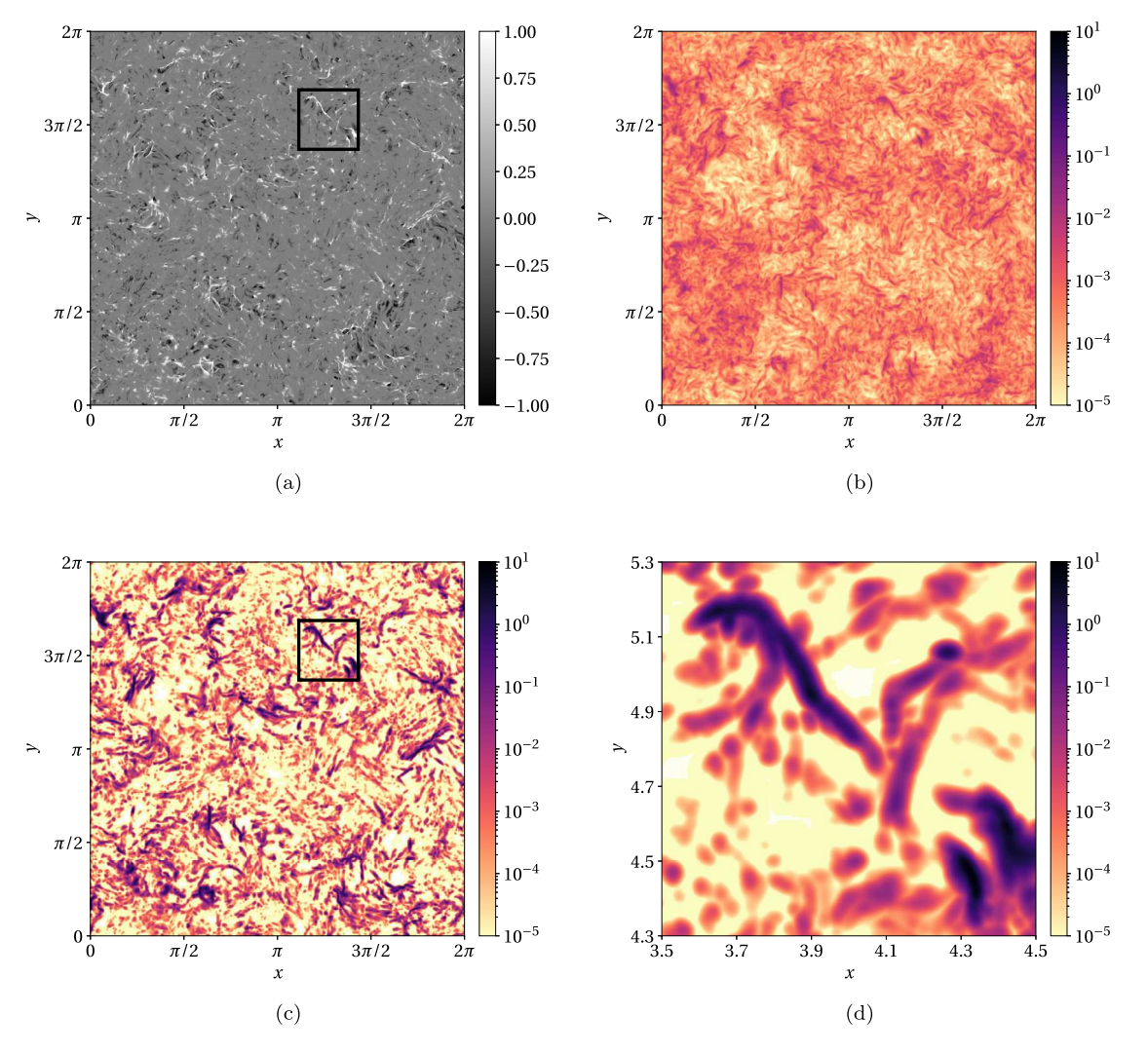


Fig. 24. Visualization of eddy shocklets and artificial diffusivities: (a) eddy shocklets visualized by the modified Ducros sensor  $-\theta|\theta|/\left[\theta^2+\omega_j\omega_j+10^{-32}\right]$ ; (b) distribution of  $\kappa^*\text{Pr}/(c_p\mu_{\text{ref}})$ ; (c) distribution of  $\beta^*/\mu_{\text{ref}}$ ; and (d) a zoomed-in view of  $\beta/\mu_{\text{ref}}$  corresponding to the boxed region in (a) and (c). In this simulation,  $T_{\text{ref}}\approx \langle T\rangle$  and  $\mu_{\text{ref}}\approx \langle \mu\rangle$ .

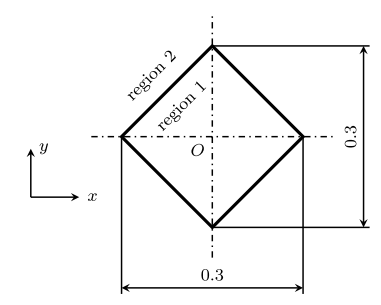


Fig. 25. Schematic of initial condition of the two-dimensional implosion problem.

numerical dissipation. With the present framework, the solution filtering, which was deemed necessary by previous works, is no longer required.

#### 4.3. Two-dimensional implosion problem

This test problem is used to demonstrate the compatibility of the computational framework with nonlinear shock-capturing schemes and approximate Riemann solvers. The problem is introduced in Ref. [59], and a modified version is used in this demonstration. The problem is configured on a two-dimensional periodic domain for  $(x,y) \in [-0.3,0.3)^2$  and is computed on a uniform Cartesian mesh and a curvilinear wavy mesh respectively. Both simulations are conducted using a  $512 \times 512$  mesh size. The curvilinear mesh generation follows the same analytical mapping used in Sec. 4.1 and is described in Eq. (58) with L = 0.6 and A = 0.05. The initial condition contains two homogeneous sub-regions as shown in Fig. 25. "Region 1" is the inner sub-region, and "region 2" is the outer sub-region. The border between the two sub-regions forms a diamond-shaped box with the four corners located at  $(\pm 0.15,0)$  and  $(0,\pm 0.15)$ . The flow is initially at rest, and the inner sub-region has a lower density and pressure than the outer sub-region. The changes across the sub-region boundary are sharp. The mathematical expressions of the initial density and pressure are specified in Eq. (60):

$$[\rho, p] = \begin{cases} [0.125, 0.140] & |x| + |y| < 0.15\\ [1.000, 1.000] & |x| + |y| \ge 0.15 \end{cases}$$

$$(60)$$

The fluid is a calorically perfect gas with  $\gamma=1.4$ . The simulation is conducted without including any physical viscosity and thermal conductivity, so the Euler system is solved. In this simulation, all primitive variables at the edge-staggered points are obtained by the eight-point adaptive targeted essentially non-oscillatory (TENO8-A) interpolation scheme, which is modified from the reconstruction scheme designed for the finite volume framework [60]. The Riemann flux is calculated using the Rusanov method [61]. The time advancement is conducted using SSP-RK3 method with CFL = 0.4.

The density profiles of the two simulations at the final calculation time t = 0.6 are shown in Fig. 26. Comparing the solution profiles on the uniform Cartesian mesh and the curvilinear wavy mesh in Fig. 26a and Fig. 26b respectively, the large-scale wave patterns are identical. There is no significant numerical issue corresponding to the mesh deformation and periodic domain extension on the curvilinear mesh. The flow instability pattern in the central region is highly sensitive to the perturbations. In these two simulations, the difference in the numerical perturbations is primarily caused by capturing the oblique waves with different mesh deformations. This demonstration only shows a specific combination of the shock-capturing scheme and approximate Riemann solver. Different combinations of shock-capturing schemes and approximate Riemann solvers are also compatible with this computational framework.

#### 4.4. LES of decaying isotropic turbulence

This test problem is designed to investigate the performance of the simulation framework used in LES or other eddy-resolving simulations of turbulent flows at very high Reynolds numbers. In an LES or other eddy-resolving simulation of turbulence, when the Kolmogorov length scale is significantly smaller than the computational grid size, physical viscous dissipation may be negligible compared to the model dissipation or numerical dissipation. A high-resolution LES or high-quality eddy-resolving simulation of a turbulent flow should keep the artificial dissipation length scale sufficiently small and near the grid size in order to preserve the resolvable turbulent flow structures across a wide range of length scales. In this test problem, the flow is assumed to be inviscid (Re $_{\lambda} \rightarrow \infty$ ). This can be alternatively interpreted as the viscous dissipation occurs at a vanishingly small length scale ( $k_{\max} \eta \rightarrow 0$ ). The definitions of  $\lambda$  and  $\eta$  are consistent with those defined in Sec. 4.2, and  $k_{\max}$  is the Nyquist wavenumber supported by the computational mesh. Therefore, no physical dissipation exists in the computational system. The simulations are configured as LES using different central schemes with an explicit SGS model and compared with eddy-resolving simulations using high-order shock-capturing schemes in combination with an approximate Riemann solver without the explicit SGS model.

The initial velocity field is solenoidal and randomly sampled in Fourier space based on the von Kármán spectrum [62]. The expression for the von Kármán velocity spectrum is given in Eq. (61).

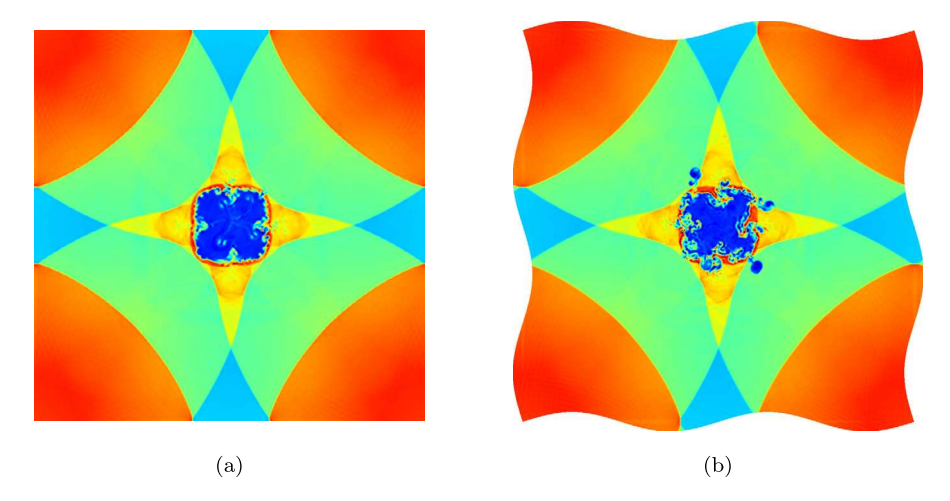


Fig. 26. Density distributions of the two-dimensional implosion problem at t = 0.6 computed on a (a) uniform Cartesian mesh and (b) curvilinear wavy mesh.

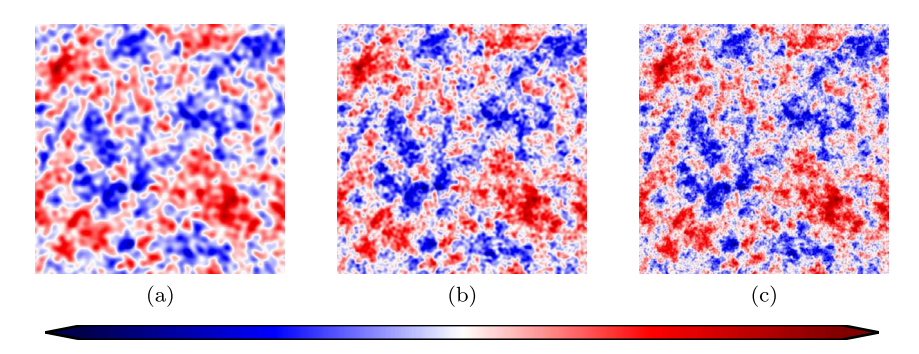


Fig. 27. Visualizations of z-velocity fields in an x-y plane with the initial conditions: (a) mesh resolution of  $64^3$ ; (b) mesh resolution of  $128^3$ ; and (c) mesh resolution of  $256^3$ . For the purpose of visualization, the coarse grid fields are upsampled to a fine grid via zero-padding in Fourier space. The scale of the color maps are the same for the three different cases. The color map scale is symmetric about 0.

$$E_{k} = \frac{\left(A/k_{s}\right)\left(k/k_{s}\right)^{4}}{\left[1 + \left(k/k_{s}\right)^{2}\right]^{17/6}}$$
(61)

where given the most energetic wavenumber,  $k_e$ ,  $k_s$  is calculated as  $k_s = k_e \sqrt{5/12}$ . In this configuration,  $k_e = 3$  is used. A is an amplitude factor. The details of the velocity generation approach for isotropic turbulence with a given energy spectrum are illustrated in Ref. [40]. Following this approach, the velocity is first generated on a 2563 mesh. Then, a three-dimensional spectrally-sharp low-pass filter is applied to only keep the non-trivial modes within a spherical region for k < 128 in Fourier space. After filtering, the field of each velocity component is consistently re-scaled to numerically match  $\langle u_i u_i \rangle = 1$ . Using this velocity field as the reference, the velocity fields are further filtered using the three-dimensional spectrally-sharp low-pass filter to keep the non-trivial modes within smaller spherical regions for k < 64 and k < 32. These filtered fields are eventually downsampled to a 128<sup>3</sup> mesh and a 643 mesh respectively. As a consequence, three sets of initial velocity fields are obtained with three different grid resolutions. The cut-off wavenumbers of the low-pass filters are equal to the Nyquist wavenumbers in each dimension instead of the maximum wavenumber that can be resolved using the three-dimensional meshes. This use of spherical spectrally-sharp filtering, as opposed to Cartesian spectrally-sharp filtering, allows for maintaining good statistical isotropy in the initial condition at every coarser grid level. Additionally, since all the velocity fields are obtained via filtering and downsampling from the same velocity field generated on the 256<sup>3</sup> mesh, the discrete initial velocity fields used as the initial conditions represent the same asymptotically smooth velocity field resolved at different levels of resolution. The initial z-component velocity profiles are visualized in Fig. 27, and the initial velocity energy spectra are shown in Fig. 28. The calculation of the velocity energy spectra in this section follows the same method as described in Sec. 4.2. The initial dimensionless density field is uniform and set to be unity as a reference. The initial dimensionless pressure is also uniform and equal to 3.5. This configuration leads to an initial turbulent Mach number of  $M_t \approx 0.45$ .

The LES are conducted using the 6th-order compact schemes, 4th-order explicit schemes, and 2nd-order explicit schemes respectively with the Vreman SGS model [14] in the momentum equation and a constant turbulent Prandtl number,  $Pr_t$ , model in the energy equation. For a calorically perfect gas,  $Pr_t$  is defined as  $Pr_t = c_p \mu_{\rm SGS}/\kappa_{\rm SGS}$ , where  $\mu_{\rm SGS}$  and  $\kappa_{\rm SGS}$  are the SGS eddy viscosity and thermal conductivity respectively. The Vreman SGS model requires a constant coefficient,  $C_{\rm SGS}$ , which is defined in Appendix B. In this demonstrative problem,  $C_{\rm SGS}$  is 0.044, 0.05 and 0.07 for the simulations using the 6th-order compact schemes, 4th-order ex-

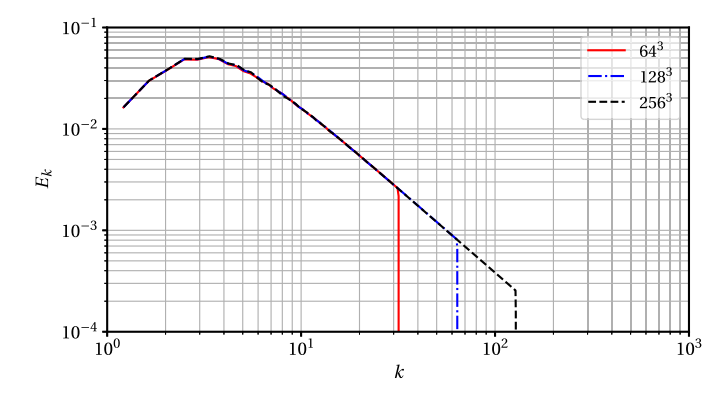


Fig. 28. Initial velocity energy spectra of the simulations at different grid resolutions.

plicit schemes, and 2nd-order explicit schemes respectively and is calibrated to obtain the correct turbulent kinetic energy decay rate. The turbulent Prandtl number is 0.7 for all simulations in this sub-section. Additional eddy-resolving simulations are conducted respectively using the TENO8-A and the five-point weighted essentially non-oscillatory (WENO5-JS) interpolation schemes [63] which are modified from their reconstruction forms designed for the finite volume framework. The simulations using the dissipative shock-capturing schemes (TENO8-A and WENO5-JS) do not include any explicit SGS model. The time advancement for all simulations is conducted using the SSP-RK3 method with CFL = 0.4. The stop time for all simulations is t = 10, which is when the turbulent kinetic energy decays by more than a factor of 15 compared to the initial condition. At the final stage, the turbulent Mach number is  $M_t \approx 0.1$ .

The velocity fields of all simulations are visualized in Fig. 29. The color map scales for all sub-figures in Fig. 29 are identical. The computational results are interpolated using the sinc modes [64] during post-processing for visualization purposes only. The velocity energy spectra for all the simulations are shown in Fig. 30. As shown by this comparison, the LES using central numerical schemes with the explicit SGS models show much higher spectral resolution than the two simulations conducted using dissipative schemes without SGS models. The SGS model dissipation starts to become dominant approximately beyond the wavenumber of  $k_{\rm max}/2$ . In contrast, the selected high-order (corresponding to the optimal weights [63,60]) shock-capturing schemes impose numerical dissipation starting at a much lower wavenumber. As a result, from the flow visualizations shown in Fig. 29, small-scale flow features are not well resolved using shock-capturing schemes compared to the simulations using central schemes with the SGS model. In Fig. 30, the energy spectra of all simulations using central schemes with the explicit SGS models clearly show the inertial sub-range where the turbulent kinetic energy cascades follow the  $k^{-5/3}$  law. In contrast, the energy spectra of simulations using implicit numerical dissipation without SGS models do not show the power-law energy cascade. This indicates that the dissipation implicitly imposed by the numerical scheme is noticeably inconsistent with the scale similarity of the turbulent cascade compared to the dissipation imposed by an explicit SGS model.

The LES results based on the central schemes do not show an observable difference in the velocity fields. Compared to the simulations using 6th-order compact schemes, the simulations using 4th-order and 2nd-order schemes do not show visible deterioration. As a further investigation of the small-scale-resolving quality of simulations obtained with the three central schemes, a three-dimensional bandpass filter is applied to only keep the modes within a spherical shell for  $k \in [16,32)$  in Fourier space. The bandpass-filtered velocity fields of all the simulations on the  $64^3$  mesh are shown in Fig. 31 (from Fig. 31a to Fig. 31e), and the bandpass-filtered velocity obtained from the LES on the  $256^3$  mesh using the 6th-order compact schemes is also provided in Fig. 31f for reference. All sub-figures in Fig. 31 are shown with the same scale of the color map. The simulations based on the shock capturing schemes (Fig. 31d and Fig. 31e) have lower feature intensities in the visualized wavenumber regime, and the sizes of the visualized features are larger than those of the bandpass-filtered LES results and the reference field (Fig. 31f). However, the bandpass-filtered LES solutions (Fig. 31a, Fig. 31b, and Fig. 31c) are equally optimal compared to the reference profile in Fig. 31f. These observations are consistent with the results presented in Ref. [65].

A reasonable explanation of this observation is that the total error is not dominated by the dispersion error of the numerical schemes. As opposed to the problem of the homentropic swirl advection illustrated in Sec. 4.1, the isotropic turbulence solution shows highly nonlinear behavior although both solutions are obtained by solving fully nonlinear systems. The linear solution behavior in the swirl advection problem (cf. Sec. 4.1) indicates that the net contributions of all the nonlinear interactions in the system are purely canceled. In contrast, the nonlinear interactions in the isotropic turbulence produce higher-wavenumber features consistent with the turbulent energy cascade. In LES, the higher-wavenumber flow features are eventually dissipated by the SGS model near the grid-size scale. When a solution has a strong linear behavior, although obtained from a nonlinear system, the dispersion error will significantly affect the computational quality in terms of the flow structure preservation. On the other hand, the evolution of the LES solution of the isotropic turbulence is dominated by the nonlinear interactions of the lower-wavenumber modes, and the higher-wavenumber modes can also intrinsically tolerate more randomness. Therefore, the solution quality evaluated from the velocity energy spectra shown in Fig. 30a and the flow visualizations of the LES solutions in Fig. 29 and Fig. 31 essentially illustrate the aliasing error produced by the nonlinear interactions among the low-wavenumber modes. Referring to the discussion in Sec. 2, the numerical error of the three sets of central schemes are not as significant in the low-wavenumber regime as they are in the high-wavenumber regime. Additionally, the transfer functions of the interpolation schemes of the lower-order schemes are even more favorable to dealiasing in

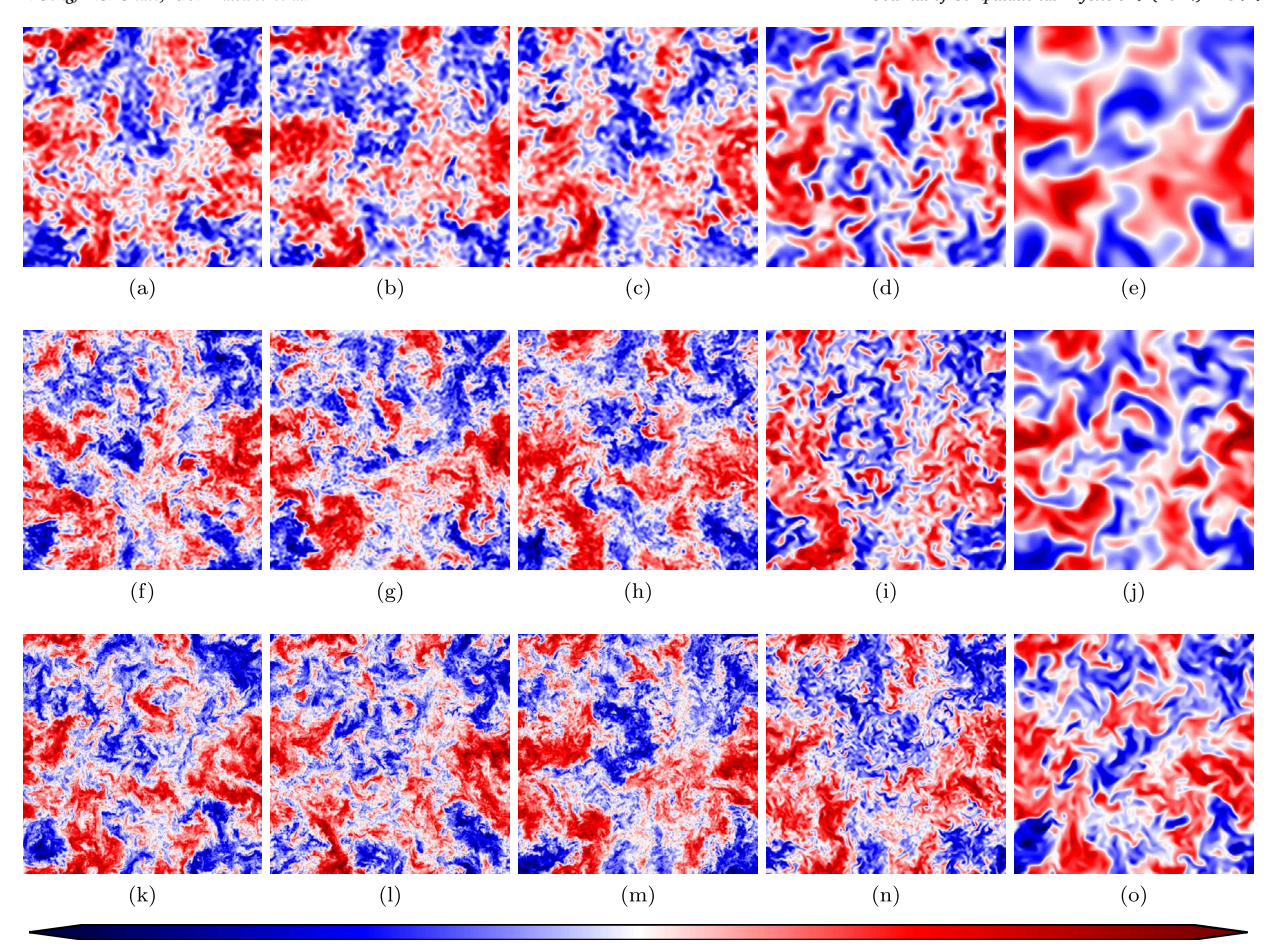


**Fig. 29.** Visualizations of the final (t = 10) z-component velocity fields in an x-y plane. The sub-figures in the first row ((a), (b), (c), (d), and (e)) are obtained from a  $64^3$  mesh; the sub-figures in the second row ((f), (g), (h), (i), and (j)) are obtained from a  $128^3$  mesh; and the sub-figures in the third row ((k), (l), (m), (n), and (o)) are obtained from a  $256^3$  mesh. The sub-figures in the first column ((a), (f), and (k)) are computed using the 6th-order compact schemes; the sub-figures in the second column ((b), (g), and (l)) are computed using the 4th-order explicit schemes; the sub-figures in the third column ((c), (h), and (m)) are computed using the 2nd-order explicit schemes; the sub-figures in the fourth column ((d), (i), and (n)) are computed using the TENO8-A interpolation schemes in combination with the 6th-order compact finite difference schemes as the divergence operator; and the sub-figures in the fifth column ((e), (j), and (o)) are computed using the WENO5-JS interpolation schemes in combination with the staggered 6th-order compact finite difference schemes as the divergence operator. The data for visualization have been upsampled in Fourier space by zero-padding during post-processing. The scales of color maps are the same for all sub-figures, and the color scale is symmetric about 0.

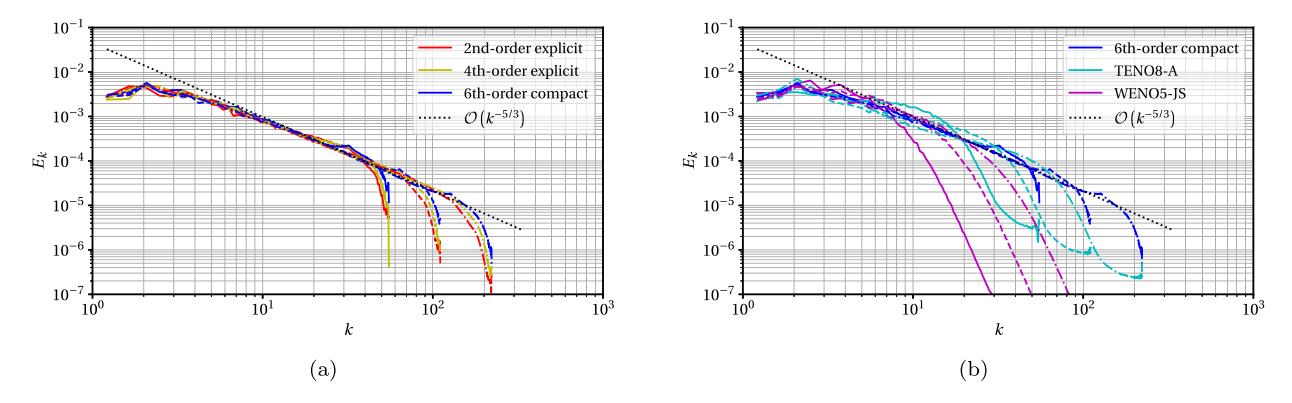


**Fig. 30.** Velocity energy spectra at the final simulation step (t = 10): (a) central schemes with Vreman SGS model; (b) nonlinear shock capturing schemes with an approximate Riemann solver where the divergence operation is computed by the staggered 6th-order compact finite difference schemes. The spectra obtained from the  $64^3$  mesh are plotted using solid curves, the spectra obtained from the  $128^3$  mesh are plotted using dashed curves, and the spectra obtained from the  $256^3$  mesh are plotted using dot-dashed curves.

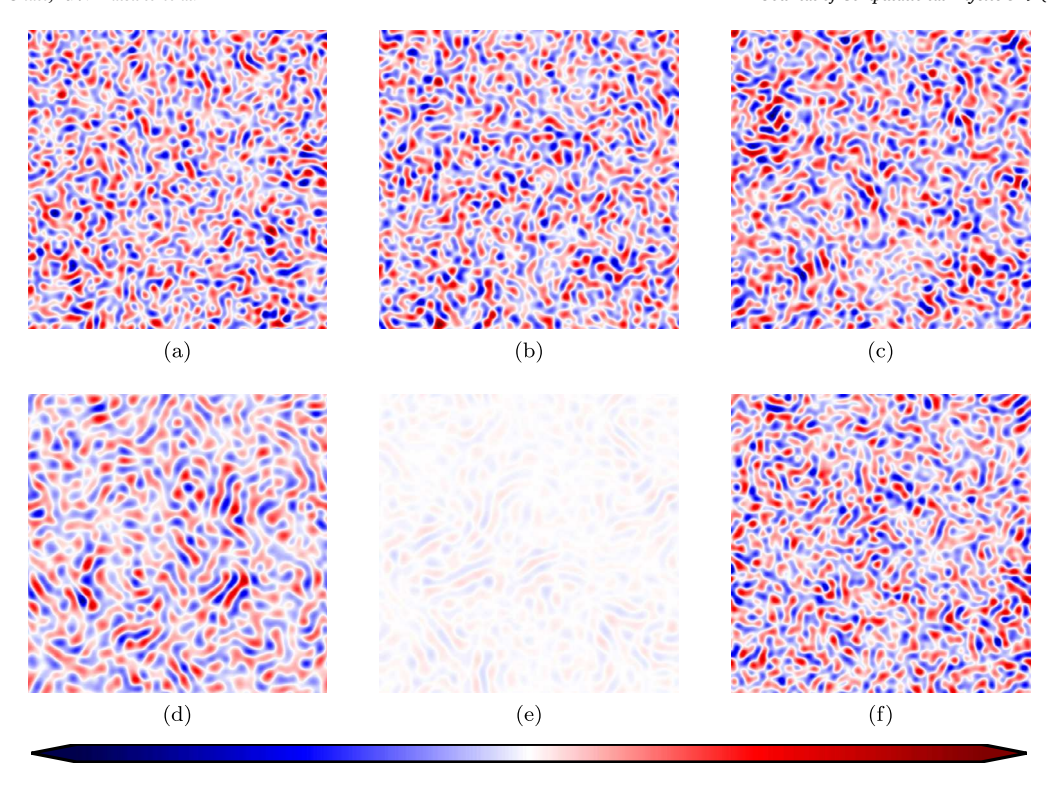


Fig. 31. Visualizations of bandpass-filtered *z*-component velocity fields on an x-y plane: (a) 6th-order compact schemes; (b) 4th-order explicit schemes; (c) 2nd-order explicit schemes; (d) TENO8-A interpolation schemes in combination with the staggered 6th-order compact finite difference schemes for the divergence operation; and (e) WENO5-JS interpolation schemes in combination with the staggered 6th-order compact finite difference schemes for the divergence operation. The sub-figures from (a) to (e) are computed from a 64<sup>3</sup> mesh. (f) is used for reference which is computed using the 6th-order compact schemes from a 256<sup>3</sup> mesh. The velocity profiles shown in all the sub-figures are sampled within a spherical shell for  $k \in [16,32)$  in Fourier space. For visualization only, the data have been upsampled in Fourier space by zero-padding. The color map scale of all the sub-figures are identical and symmetric about 0.

the nonlinear fluxes assembly by more aggressively reducing high-wavenumber mode amplitudes. Consequently, for LES of decaying isotropic turbulence, the 2nd-order explicit schemes, 4th-order explicit schemes, and 6th-order compact schemes present equally high-quality solutions in the velocity fields.

Besides the velocity field, the pressure field is also investigated. The configuration of the initial condition generates significant transients in the flow, and they remain as acoustic waves in this inviscid (asymptotically high-Reynolds-number) turbulence as it decays in the range of resolved scales. At the final stage (t = 10), the visualizations of the pressure field from all simulations are shown in Fig. 32 with the same color map scale. For each scheme, more detailed wave structures are resolved as the grid resolution increases. Comparing different schemes, higher-order schemes provide sharper and clearer coherent wave structures at the same grid resolution, and they show more rapid enhancement in resolving detailed wave features associated with grid refinement. Unlike the velocity field, the simulations with the TENO8-A scheme and without an explicit SGS model provide significantly improved spectral performance in resolving transient pressure waves. To quantify the numerical performance, the pressure field is decomposed as follows.

$$p = p^{\text{sol}} + p^{\text{dil}} + \langle p \rangle \tag{62}$$

where  $p^{\text{sol}}$  and  $p^{\text{dil}}$  are the solenoidal and dilatational components respectively, and  $\langle p \rangle$  is the mean component. In the low-Mach number regime, the solenoidal pressure is estimated by solving the Poisson equation [8].

$$-\frac{\partial^2 p^{\text{sol}}}{\partial x_j \partial x_j} \approx \langle \rho \rangle \frac{\partial u_i^{\text{sol}}}{\partial x_j} \frac{\partial u_j^{\text{sol}}}{\partial x_i}$$
 (63)

where  $u_i^{\text{sol}}$  is the solenoidal component of the velocity field. In this work, the solenoidal projection is conducted in Fourier space using  $\hat{u}_i(k_m)$ , the three-dimensional discrete Fourier transform of  $u_i$  with respect to each wavenumber vector  $k_m$ .

$$u_i^{\text{sol}} = \sum_{k_m \neq 0} \mathcal{P}_{ij}^{\perp} \widehat{u}_j(k_m) e^{ik_m x_m} \tag{64}$$

where  $\mathcal{P}_{ij}^{\perp}$  is the solenoidal projector defined in Sec. 4.2. With the solenoidal pressure solved, the dilatational pressure is calculated from Eq. (62). The energy spectra of the solenoidal and dilatational pressure from all simulations are shown in Fig. 33 and Fig. 34

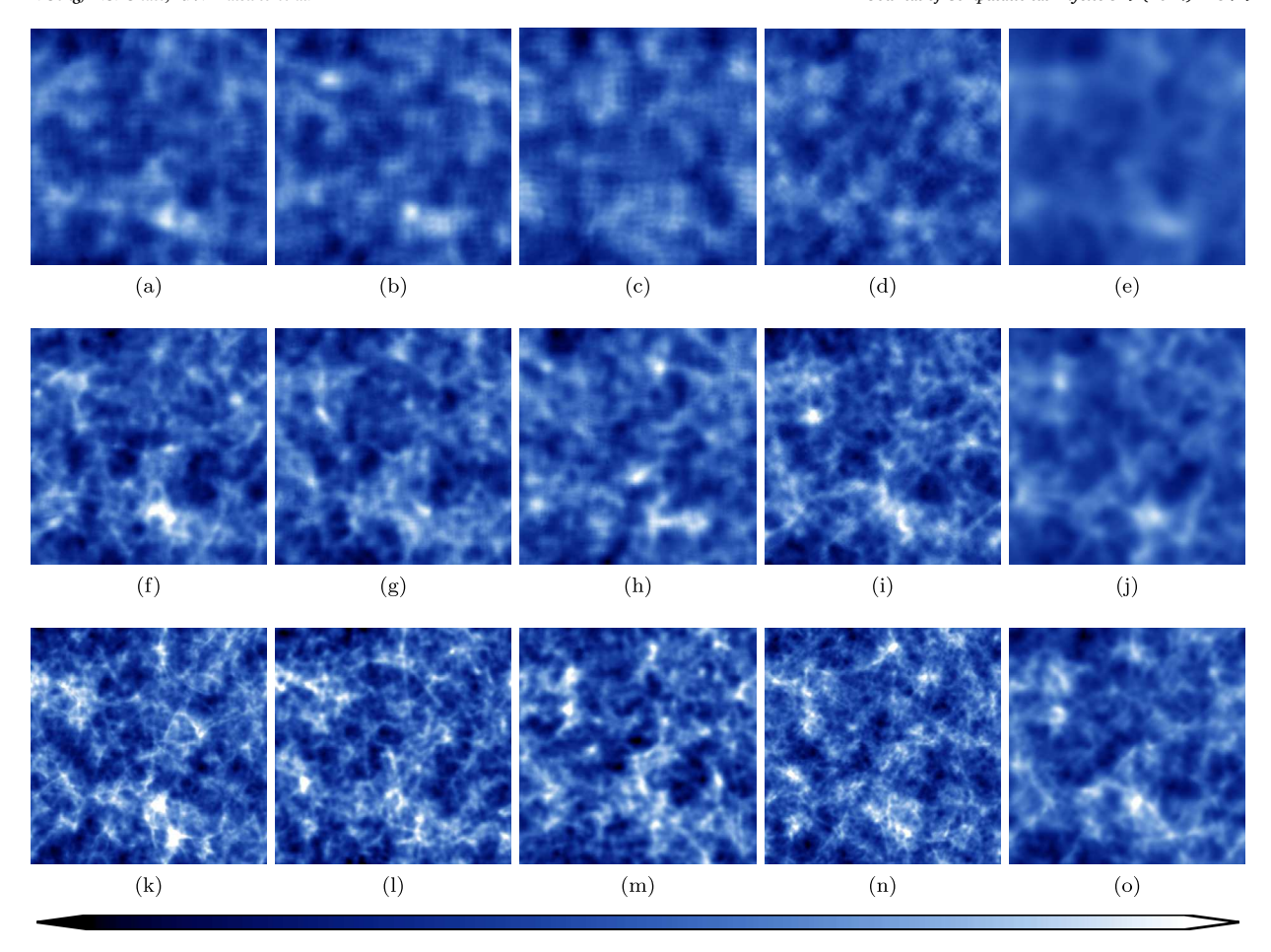


Fig. 32. Visualizations of the final (t = 10) pressure fields in the x-y plane. The color map scales are the same for all sub-figures. See caption in Fig. 29 for details of each sub-figure.

respectively. At a low turbulent Mach number, the solenoidal pressure is a reflection of the velocity field. Similar trends are observed by comparing the energy spectra of the velocity in Fig. 30 and solenoidal pressure in Fig. 34. The solenoidal pressure spectra of all the simulations using central schemes with an explicit SGS model exhibit clear inertial sub-ranges up to near-Nyquist wavenumbers, and at the same grid resolution, no large differences are observed as shown in Fig. 33a. The spectra of solenoidal pressure obtained from shock-capturing-scheme-based simulations indicate overly dissipative velocity fields and do not clearly resolve the turbulent cascade features, as shown in Fig. 33b, due to the inconsistent numerical dissipation behavior between the nonlinear numerical dissipation and physically expected SGS dissipation. On the other hand, the dilatational pressure energy spectra, shown in Fig. 34, convey different evaluation perspectives compared to the velocity and solenoidal pressure spectra. Since the transient acoustic waves have relatively sharp wave fronts and are strongly coherent at large scales, the simulation results are sensitive to the dispersion error and the spectral resolution. Comparing the simulations conducted with central schemes, in Fig. 34a, the simulations using higher-order schemes resolve more acoustic energy in the moderate wavenumber regime. In Fig. 34b, the simulations conducted with the TENO8-A scheme resolve even more transient acoustic energy in the moderate wavenumber regime compared to the simulations using the 6th-order compact schemes, as they primarily benefit from the higher-order convergence.

#### 4.5. LES of flow over a cylinder

This set of problems is selected to demonstrate the numerical performance in applications of LES using curvilinear meshes. The problems are defined in a three-dimensional domain where the z-direction is periodic with length  $L_z$ . The schematic of the problem configuration in the x-y cross-section is shown in Fig. 35. The cylinder object with a diameter D is placed at the origin, and the wall of the cylinder defines the inner boundary of the physical domain. The outer boundary of the domain is concentric with the cylinder object, and its diameter is  $D_0$ . The freestream in the far-field is imposed and preserved by a numerical sponge layer [66]. The thickness of the sponge layer is denoted as  $L_{\rm sp}$ . For a quality setup,  $(D_0 - 2L_{\rm sp})/D \gg 1$  must be satisfied. The freestream flow is aligned with the x-direction and specified by the pressure  $(p_\infty)$ , temperature  $(T_\infty)$ , and Mach number  $(M_\infty)$ .  $M_\infty$  is defined as the ratio of the flow speed to the speed of sound at the freestream condition. For a calorically perfect gas, expressed in terms of the

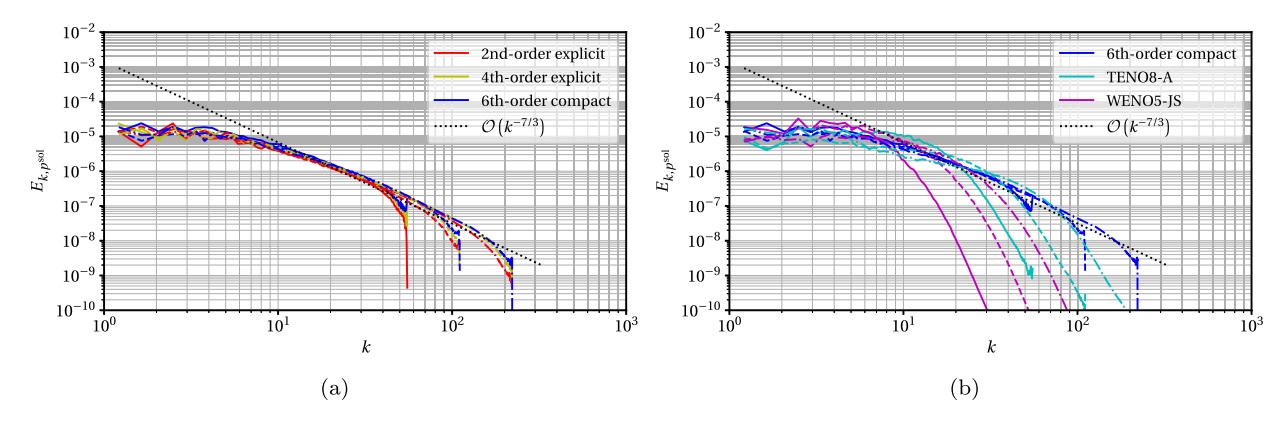
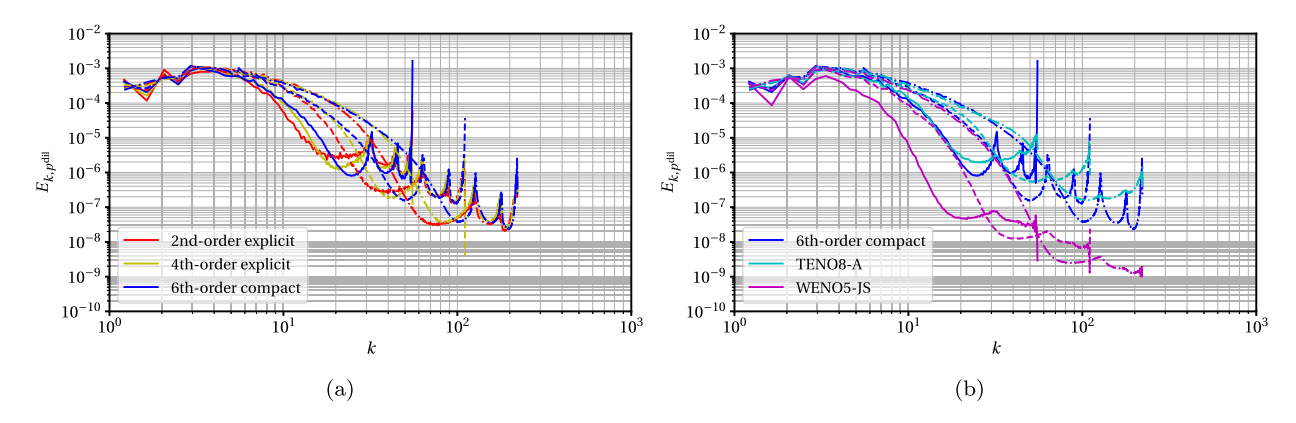


Fig. 33. Energy spectra of solenoidal pressure at final step (t = 10): (a) central schemes with Vreman SGS model and (b) nonlinear shock-capturing schemes with an approximate Riemann solver where the divergence operation is computed by the staggered 6th-order compact finite difference schemes. The line styles are the same as those used in Fig. 30.



**Fig. 34.** Energy spectra of dilatational pressure at the final step (t = 10): (a) central schemes with the Vreman SGS model and (b) nonlinear shock-capturing schemes with an approximated Riemann solver where the divergence operation is computed by the staggered 6th-order compact finite difference schemes. The line styles are the same as those used in Fig. 30.

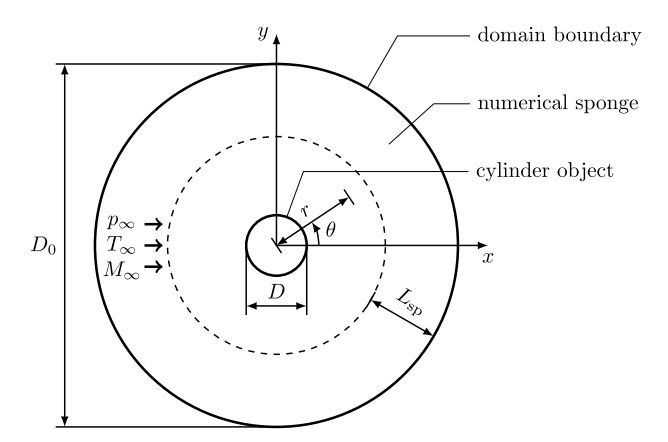
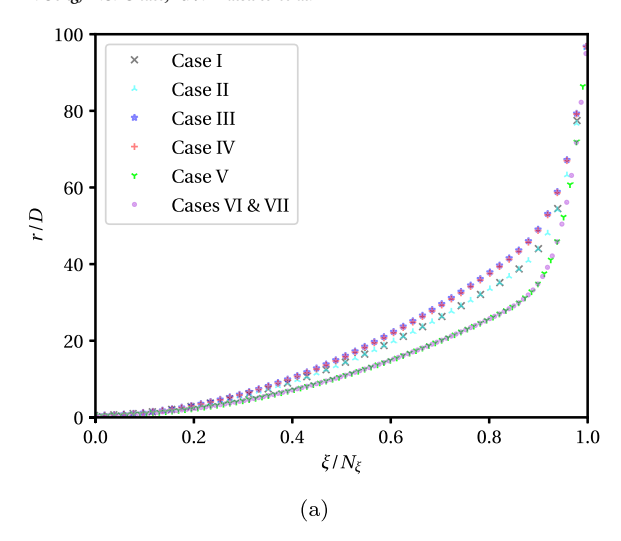
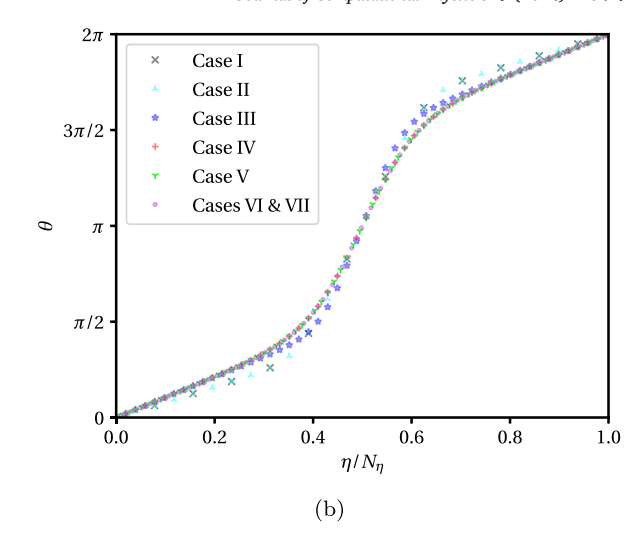


Fig. 35. Schematic of configuration of LES of flow over a cylinder. The configuration is homogeneous in the z-direction (not shown in the schematic).

specified quantities, the freestream speed is  $u_{\infty}=M_{\infty}\sqrt{\gamma RT_{\infty}}$ . The characteristic Reynolds number is defined as  $\text{Re}_D=\rho_{\infty}u_{\infty}D/\mu_{\infty}$ , where  $\rho_{\infty}$  is the freestream density calculated by the EOS of a calorically perfect gas. In this set of problems, the specific gas constant and the ratio of specific heats are R=1 and  $\gamma=1.4$  respectively. The local dynamic viscosity is evaluated as  $\check{\mu}=\mu_{\infty}\left(T/T_{\infty}\right)^{0.76}$ . The Prandtl number is assumed to be constant at Pr=0.7. The definition of Pr is the same as that in Sec. 4.2 which is used to determine the local physical thermal conductivity. The Vreman SGS model [14] is applied with  $C_{\text{SGS}}=0.06$ , and a constant turbulent Prandtl number,  $\text{Pr}_I=1$ , is used for all the simulations in this sub-section, where the definition of  $\text{Pr}_I$  is the same as that in Sec. 4.4. The





**Fig. 36.** Curvilinear mesh mapping in *x-y* plane: (a) mapping of the radial coordinate; (b) mapping of the azimuthal coordinate. Symbols shown in the sub-figures are plotted every ten grid points.

**Table 2** Specifications of simulations in Sec. 4.5: Cases I, II and III use central fluxes only; Cases IV, V, VI, and VII use central-Riemann hybrid fluxes, where a sharp switching, indicated by the threshold values of a turbulence-based shock sensor,  $\phi_{\Lambda}^*$ , and an acoustics-based shock sensor,  $\phi_{\Lambda}^*$ , is applied.

Label	$M_{\infty}$	$\mathrm{Re}_D$	Mesh Size	$L_z/D$	$D_0/D$	$L_{\rm sp}/D$	CFL	$\phi_{\mathrm{T}}^{*}$	$\phi_{ m A}^*$
Case I	0.25	3900	256 × 128 × 128	$2\pi$	200	50	0.98	-	-
Case II	0.25	3900	$512\times256\times128$	$2\pi$	200	50	0.98	-	-
Case III	0.25	3900	$512\times512\times128$	$2\pi$	200	50	0.98	-	-
Case IV	0.80	$1.66\times10^5$	$512\times512\times128$	$2\pi$	200	60	0.60	0.45	0.05
Case V	0.80	$1.66\times10^5$	$768 \times 768 \times 128$	$2\pi$	200	60	0.60	0.38	0.07
Case VI	0.80	$1.66\times10^5$	$1024 \times 1024 \times 384$	$2\pi$	200	60	0.60	0.35	0.05
Case VII	0.80	$1.66\times10^5$	$1024\times1024\times384$	$2\pi$	200	60	0.60	0.35	0

compact numerical schemes along the non-periodic dimension where physical boundary conditions are imposed are discussed in Appendix D, and the detailed SGS treatment is provided in Appendix B.

A nearly incompressible flow and a transonic flow are simulated as demonstrations. The freestream Mach numbers for the two flow conditions are  $M_{\infty}=0.25$  and  $M_{\infty}=0.8$  respectively. The Reynolds numbers are  $\mathrm{Re}_D=3900$  and  $\mathrm{Re}_D=1.66\times10^5$  for the low-Mach flow and transonic flow respectively. Both flow conditions have been investigated in prior studies [67–69]. For the low-Mach flow condition, the simulation only uses central fluxes, and for the transonic flow condition, the simulation uses hybrid central-Riemann fluxes. The central fluxes are calculated using the sixth-order compact schemes, and the Riemann fluxes are assembled in Rusanov form [61] with the WENO5-JS interpolation scheme [63]. The hybridization is sharply switched, so the fluxes are either fully central or Riemann-typed. The switching is indicated by two shock sensors evaluated based on the turbulent and acoustic flow features respectively. The values of the turbulence-based shock sensor and the acoustics-based shock sensor are denoted as  $\phi_T$  and  $\phi_A$  respectively. In this work, the range of the sensor values are  $\phi_T \in (-1,1)$  and  $\phi_A \in (-1,1)$  where a higher value indicates a stronger local compression. The Riemann flux will be used if both sensor values are greater than their threshold values,  $\phi_T > \phi_T^*$  and  $\phi_A > \phi_A^*$ , where the superscript, "\*", denotes the corresponding threshold value. The shock sensors are evaluated at each edge-staggered location. The details of the central-Riemann flux hybridization are discussed in the following context in this section. Three simulations for the low-Mach flow condition (Cases II, II, and III) and three for the transonic flow condition (Cases IV, V, and VI) are conducted to assess grid sensitivity, and one additional simulation under the same transonic flow condition (Case VII) is conducted to further investigate the effects of shock sensors. The detailed setup for each simulation is listed in Table 2.

The computational mesh is an "O-" type mesh with orthogonality preserved in physical space. In order to keep the consistency of the right-handed coordinate system in both the reference domain and the physical domain, the mapping from the reference domain to the physical domain is of the form  $\xi \mapsto r$ ,  $\eta \mapsto \theta$ , and  $\zeta \mapsto z$ , where r and  $\theta$  are the radial distance and the azimuthal angle respectively as marked in Fig. 35. The grid spacing is uniform in z-direction. The detailed mapping for each case listed in Table 2 is plotted in Fig. 36. Along the radial direction, the mesh is refined near the cylinder object to resolve the laminar boundary layer and coarsened in the far-field region to save the grid resolution while maintaining a sufficiently large domain. In the azimuthal direction, more grid points are distributed on the wake side to enhance the mesh resolution in regions of interest. The computational mesh used for Case I is shown in Fig. 37 as an illustration. The near-wall mesh pattern shown in Fig. 37c implies that the acoustic CFL condition is

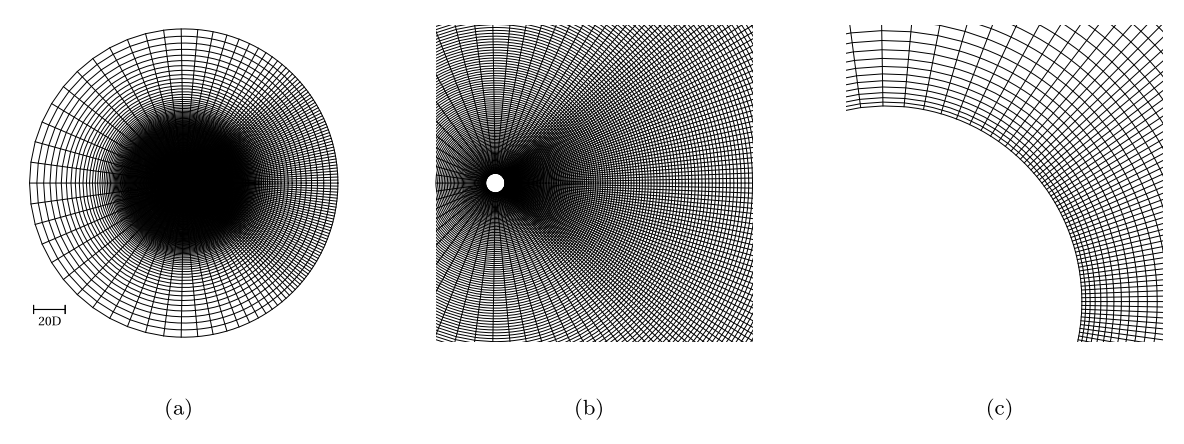


**Fig. 37.** Visualization of the computational mesh in *x-y* cross-section used for Case I: (a) full view; (b) detailed view in the wake region; (c) detailed view in the near-wall region. The mesh spacing in *z*-direction is uniform.

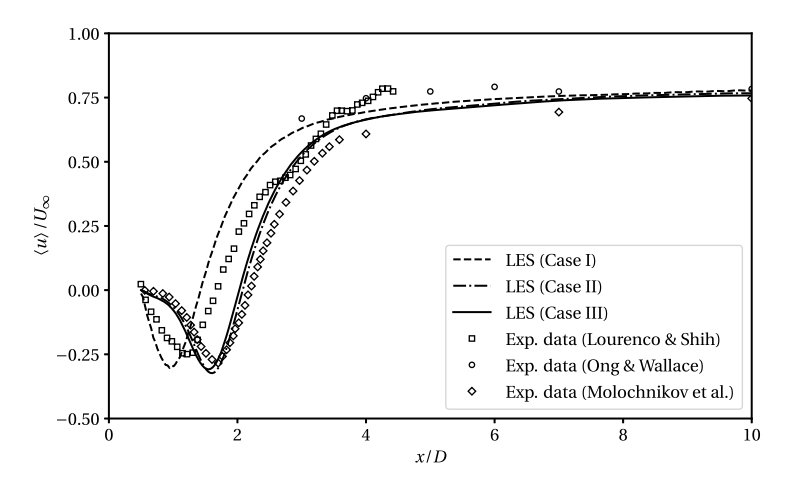


Fig. 38. Streamwise velocity profiles along the centerline in the cylinder wake in the low-Mach flow: the experimental data are from Lourenco and Shih [70], Ong and Wallace [68], and Molochnikov et al. [71], measured using PIV, HWA, and SIV respectively.

limited by the wall-normal mesh refinement, and the azimuthal grid refinement does not cause a more restrictive constraint on the time advancement process.

The mean streamwise velocity profile along the centerline in the cylinder wake region for each simulation is shown in Fig. 38, and the simulation results are compared with the experimental data [70,68,71]. The experimental data from Ref. [70] are collected using the method of particle image velocimetry (PIV), the data from Ref. [68] are measured using hot wire anemometry (HWA), and the data from Ref. [71] are obtained using the smoke image velocimetry (SIV) technique. The operator,  $\langle (\cdot) \rangle$ , in this section denotes the temporal averaging and spatial averaging in the *z*-direction. Temporal averaging is performed at every time-step once a statistically stationary state devoid of any initial transients has been reached. With successive mesh refinement from Case I to Case III, the streamwise velocity profiles asymptotically converge. In the near wake region, x/D < 3, the converged profile is closer to the experimental data from Molochnikov et al. [71].

The averaged streamwise velocity profiles along the transverse direction at different locations in the cylinder wake are shown in Fig. 39a. In the near-wake region, as shown in Fig. 39a, the velocity profiles from all three cases well match the experimental measurements at x/D = 0.58. However, at x/D = 1.06 and x/D = 1.54, the experimental data from Lourenco and Shih [70] and Molochnikov et al. [71] have obvious discrepancies. The LES results from the coarsest mesh (Case I) most closely match the measured profiles in Lourenco and Shih [70], and the results from the refined meshes (Case II and III) converge to the measured profiles in Molochnikov et al. [71]. In the far-wake region, as shown in Fig. 39b, the discrepancy between the two experimental measurements reduces as x/D increases, and the converged LES results agree well with the experimental data.

The profiles of velocity variance related to the streamwise and transverse velocity components along the transverse direction at different cylinder wake locations are shown in Fig. 40. The LES results are compared with the experimental measurements. Defining the fluctuating component  $u_i' = u_i - \langle u_i \rangle$ , the velocity variance is calculated as  $\langle u_i'u_j' \rangle = \langle u_iu_j \rangle - \langle u_i \rangle \langle u_j \rangle$  assuming fully-converged statistics. For all three variances,  $\langle u'u' \rangle$ ,  $\langle u'v' \rangle$ , and  $\langle v'v' \rangle$ , the converged simulation data qualitatively agree with the experimental data. For the autovariances,  $\langle u'u' \rangle$  and  $\langle v'v' \rangle$ , the simulation on the coarsest mesh gives an overestimation. The converged LES profiles still slightly overestimate the experimental data at x/D=4, but the profiles match well at other wake locations. For the covariance,

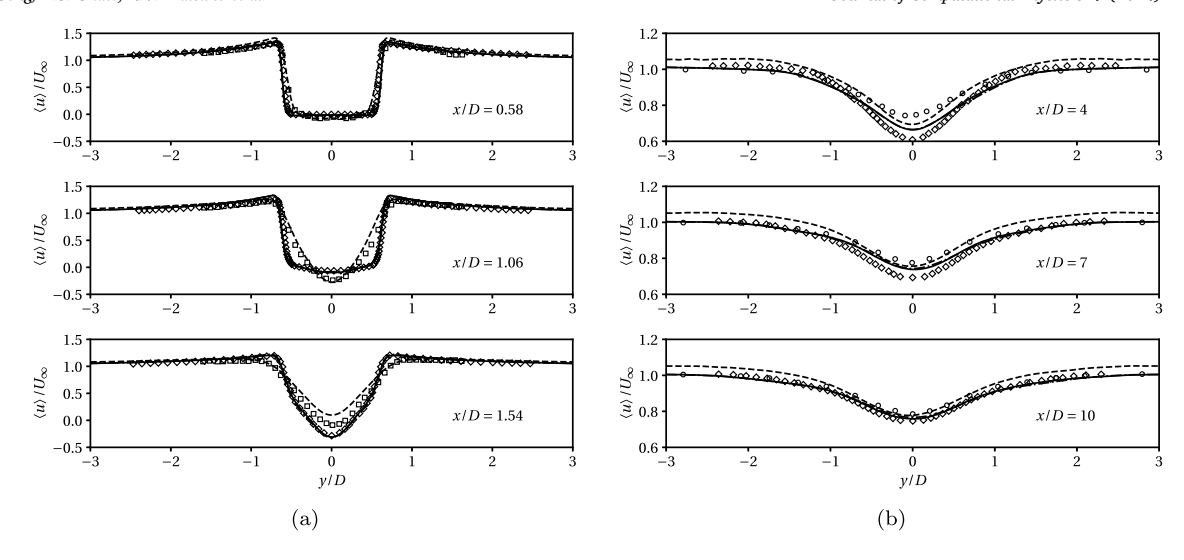
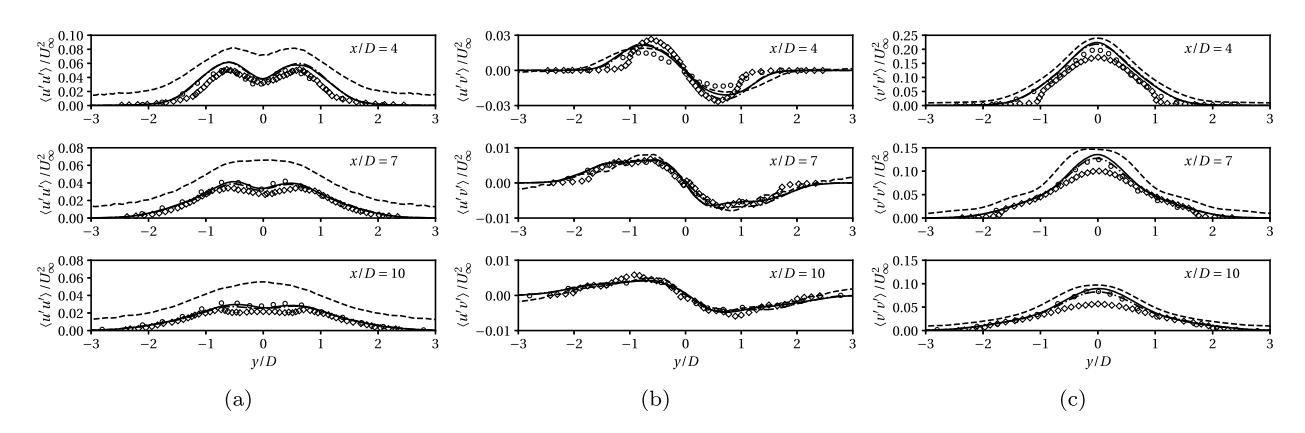


Fig. 39. Streamwise velocity profiles at different locations in the cylinder wake in the low-Mach flow: (a) velocity profiles at near-wake locations; (b) velocity profiles at far-wake locations. The symbols of the experimental data points are identical to those in Fig. 38.



**Fig. 40.** Velocity variance profiles at different cylinder wake locations in the low-Mach flow: (a)  $\langle u'u' \rangle$  profiles; (b)  $\langle u'v' \rangle$  profiles; (c)  $\langle v'v' \rangle$  profiles. The symbols of the experimental data points are identical to those in Fig. 38.

 $\langle u'v' \rangle$ , a slight discrepancy between the LES and experimental data can be observed at x/D=4, but all three LES profiles agree well with the experimental measurements at x/D=7 and x/D=10.

The simulations with the transonic freestream condition, used as a demonstration, involve comprehensive use of the capabilities developed in this framework including the curvilinear mesh with periodic and non-periodic boundary conditions, SGS models, and central-Riemann flux hybridization. Representative flow visualizations from Case VI are shown in Fig. 41. Fig. 41a shows numerical Schlieren imaging at a cross-section in z-direction. The numerical Schlieren imaging primarily reveals the turbulent wake flow structures associated with vortex shedding, a spatially and temporally growing Kelvin-Helmholtz instability at the edge of the nearwake region leading to transition to turbulence, and shock waves. The flow contains two strong normal shocks interacting with the edge of turbulent wake and two weak oblique shocks attached to the laminar boundary layer at the cylinder surface as observed from prior experimental and numerical studies [72,73]. In addition, the simulation also captures the eddy shocklets in the near wake region as well as the periodic formation of normal shocks between the neighboring shedding vortices caused by the counter-rotating flow motion. The ratio of the SGS viscosity to the physically computable viscosity is visualized in Fig. 41b. Using an SGS viscosity model, this ratio of the viscosities also indicates the ratio of the dissipation imposed by the SGS model to the resolved viscous dissipation in the LES. As shown in Fig. 41b, in comparison with the numerical Schlieren imaging, the SGS viscosity rapidly vanishes away from the turbulent flow structures. Near the cylinder wall, the SGS viscosity is nearly zero, and the near-wall flow is well-resolved. Farther away from the cylinder, SGS dissipation becomes dominant in resolving the turbulent structures mainly because of the mesh coarsening. For the shock-turbulence interactions, to avoid the overly dissipative numerical behavior due to the activation of the shock-capturing treatment as well as the SGS model [74], the SGS model is enforced to be zero locally where the shock-capturing scheme is active.

The pressure coefficient profiles at the cylinder surface for the simulations of the transonic freestream condition (Cases IV, V, VI, and VII) are shown in Fig. 42. The simulation results are compared with the experimental data [69] which are collected at the surface

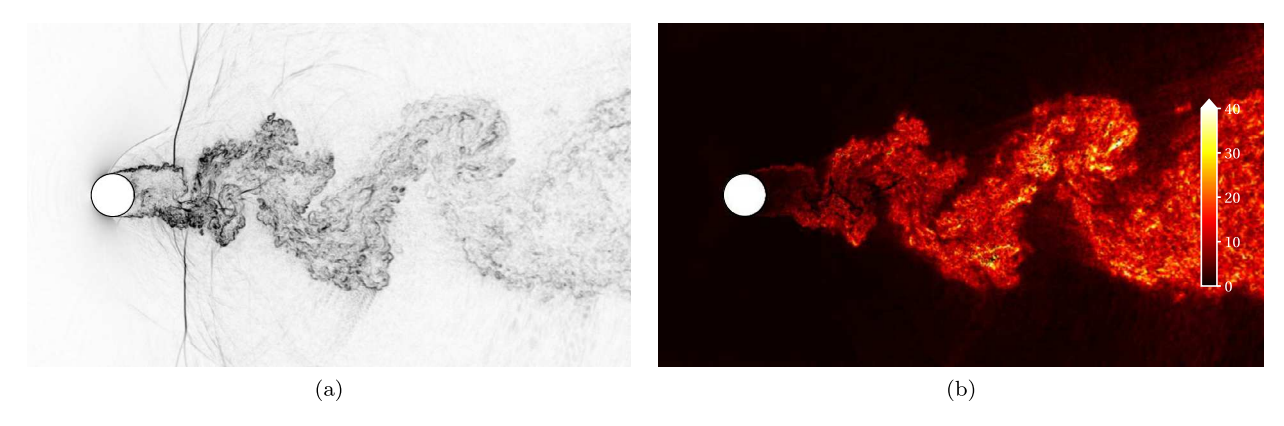


Fig. 41. Visualizations of the LES of transonic flow over a cylinder (Case VI) at the same physical time: (a) numerical Schlieren imaging,  $|\nabla \rho|$ ; (b) ratio of the SGS viscosity to the physically computable viscosity,  $\mu_{SGS}/\check{\mu}$  (cf. Appendix B).

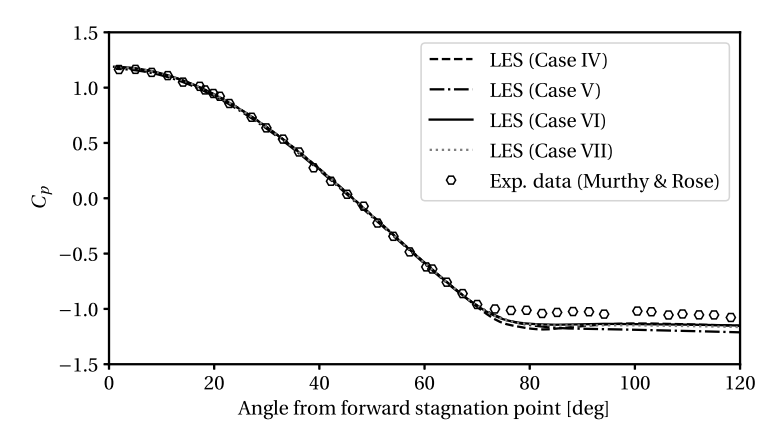


Fig. 42. Profile of the pressure coefficient,  $C_p = (p - p_{\infty}) / (\rho U_{\infty}^2/2)$ , on the cylinder surface in the transonic flow. The experimental data are from Murthy and Rose [69] and measured at the static surface pressure ports through a scanning valve device.

pressure ports placed near the midspan locations through a scanning valve device. All four LES profiles show quantitative agreement in the region where the angle from the forward stagnation point is less than 70°. Additionally, the boundary layer separation points indicated by the pressure coefficient profiles consistently match among the LES and experimental data. Some discrepancies exist in the back pressure among the LES results and the experimental measurements, and the simulation results with mesh refinement in the near-wake region (Cases V and VI) show a non-monotonic convergence in the back pressure calculation compared to that of the coarsest mesh (Case IV). The use of the acoustics-based shock sensor is insensitive to the calculation of the mean pressure coefficient for Cases VI and VII.

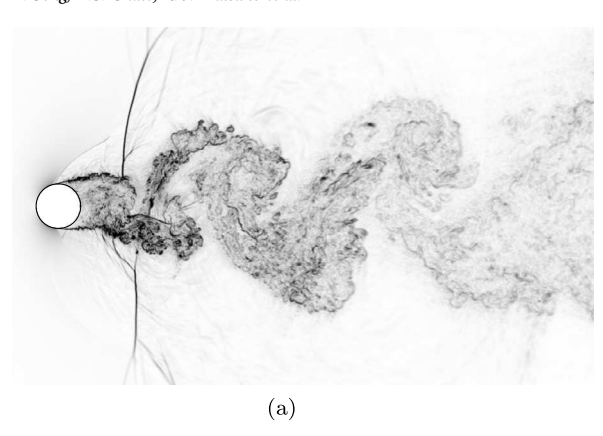
The hybridization of central and Riemann fluxes is jointly controlled by a turbulence-based shock sensor and an acoustics-based shock sensor. The Riemann fluxes will be selected only when both shock sensor values are greater than their corresponding threshold values as listed in Table 2. In this work, the modified Ducros sensor (cf. Sec. 4.2) is used as the turbulence-based shock sensor,  $\phi_T$ .

$$\phi_{\rm T} = \frac{-\theta |\theta|}{\theta^2 + \omega_j \omega_j + \epsilon^2} \tag{65}$$

where  $\theta$  is the velocity dilatation,  $\omega_j$  is the vorticity vector, and  $\epsilon = 10^{-16}$  is applied for numerical regularization. The acoustics-based shock sensor is given as

$$\phi_{\rm A} = -\tanh(2\theta\Delta/c) \tag{66}$$

where c is the local speed of sound, and  $\Delta$  is a characteristic length scale representing the local grid size. In this work,  $\Delta = \sqrt[3]{J}$  is used where J is the Jacobian of the metric tensor (cf. Sec. 3.3) defined in Eq. (39). The modified Ducros sensor in Eq. (65) detects the shock based on the velocity dilatation strength relative to the enstrophy. This sensor is particularly sensitive to the turbulent flow structures and will deactivate the use of Riemann fluxes in the turbulent flow region. However, when the enstrophy is relatively low as in the laminar flow region or the edge of the turbulent flow region, the modified Ducros sensor is less sensitive due to the lack of reference enstrophy and may mis-identify weak compression waves as shocks. The acoustics-based sensor will then play a dominant role in such regions. In the definition of the acoustics-based sensor, in Eq. (66), the dimensionless quantity,  $\theta \Delta/c$ , represents a "grid Mach number." For a strong compression wave, including a shock wave, the grid Mach number quantifies the difficulty in



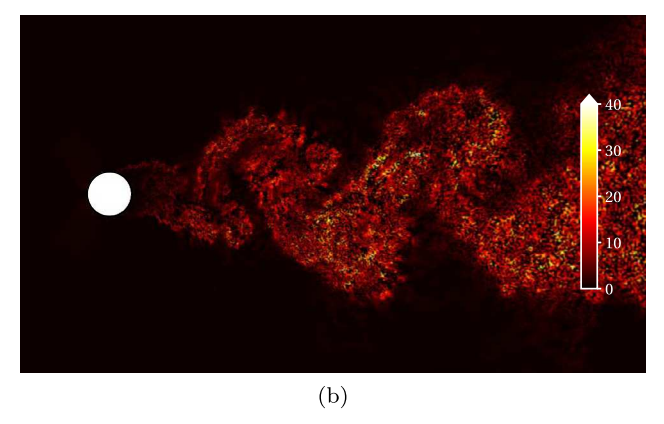


**Fig. 43.** Visualizations of the LES of transonic flow over a cylinder (Case VII) at the same physical time: (a) numerical Schlieren imaging,  $|\nabla \rho|$ ; (b) ratio of the SGS viscosity to the physically computable viscosity,  $\mu_{SGS}/\check{\mu}$  (cf. Appendix B).

numerically resolving the wave with the resolution supported by the computational mesh. According to the acoustics-based sensor, if a compression wave is too strong to be well-resolved by the computational mesh, the shock-capturing method should be enabled. The combination of the turbulence-based and acoustics-based shock sensors will more effectively suppress the unnecessary utilization of the shock-capturing method to avoid overly dissipative simulation results.

The simulation results from Cases VI and VII are used to compare the effects of the flux hybridization. The simulation of Case VII uses a flow state computed with Case VI as its initial condition where all transients are flushed out of the domain of interest. The simulation results are visualized in Fig. 43 after approximately another 33 convective time units, i.e.,  $tU_{\infty}/D \approx 33$ . The visualizations in Fig. 41, for Case VI, and Fig. 43, for Case VII, are at the same physical time for comparison. The large-scale flow structures in the two cases are identical. Setting the acoustics-based shock sensor threshold to  $\phi_A^* = 0$  (Case VII) yields the strategy described in Ref. [37], where the activation of a shock-capturing method is fully controlled by the modified Ducros sensor in the compression region. In contrast,  $\phi_A^* > 0$  (Case VI) additionally enforces the central flux to be applied if the compressive motion is relatively weak in both turbulent and laminar regions. Comparing the visualizations shown in Fig. 41 and Fig. 43, more small-scale wave structures in the laminar flow regions can be resolved in Case VI where  $\phi_A^* > 0$ . Furthermore, the relative SGS viscosity in the turbulent wake region is larger in Case VI compared to that in Case VII.

The behavior of the shock sensors and flux hybridization status for Cases VI and VII are visualized in Fig. 44. The turbulence-based shock sensor in both cases is capable of identifying the shock structures and can effectively suppress the use of Riemann fluxes in the turbulent wake region. However, near the forward stagnation point where the flow is laminar and shock-free, the turbulence-based shock sensor mis-identifies the shock structure in both cases due to the small vorticity magnitude compared to the compressive motion characterized by negative dilatation. In addition, in the wake region at the edges of the turbulent shedding vortices and the region farther away, the acoustic waves are also mis-identified as shocks by the turbulence-based shock sensor. The acoustics-based sensor in both cases highlights the shock structures and successfully recognizes the weak compression near the forward stagnation point and the acoustic waves that can be well-resolved with the local mesh resolution. The simulation of Case VI benefits from the acoustics-based sensor while the simulation of Case VII only uses the acoustics-based sensor to distinguish compressive motions from expansive motions. In the comparison shown in Fig. 44e and Fig. 44f, the use of Riemann fluxes in Case VII is highly localized to the shock structures, and the shock-capturing method is effectively deactivated elsewhere. In contrast, in Case VII, the shock-capturing method is unnecessarily enabled in the non-turbulent flow region although it is successfully suppressed in the turbulent flow structures.

#### 5. Conclusions

A high-order compact-finite-difference-based computational framework is proposed for simulations of compressible turbulent flows. This framework uses collocated and staggered first derivative schemes as well as the compact midpoint interpolation scheme. During the solution process, all conservative variables are only stored at the collocated nodal points, and the fluxes are assembled at the edge-staggered locations using the interpolated primitive variables. Fourier analysis indicates that robustness is gained by reducing the aliased interactions during the assembly of the nonlinear advective fluxes at edge-staggered points. Additional robustness results from staggered evaluation of viscous fluxes that leads to enhanced accuracy in resolving the viscous-type dissipation at small scales especially near and at the Nyquist wavenumber. Eddy-resolving simulations, such as DNS and LES, can therefore maintain numerical stability without additional numerical filtering of the solution. This attribute is particularly pertinent to computations on curvilinear meshes where spatial variations of the metric terms add to further aliasing. A GCL-consistent metric generation process is also developed as part of the framework. For flows containing shocks, the flux evaluation is compatible with the application of nonlinear shock-capturing schemes combined with an approximate Riemann solver via state variable blending. The staggered calculation of viscous fluxes is favored when other shock-regularization schemes, such as localized artificial bulk viscosity and thermal conductivity models, are used, especially in problems where small-scale eddy shocklets are present.

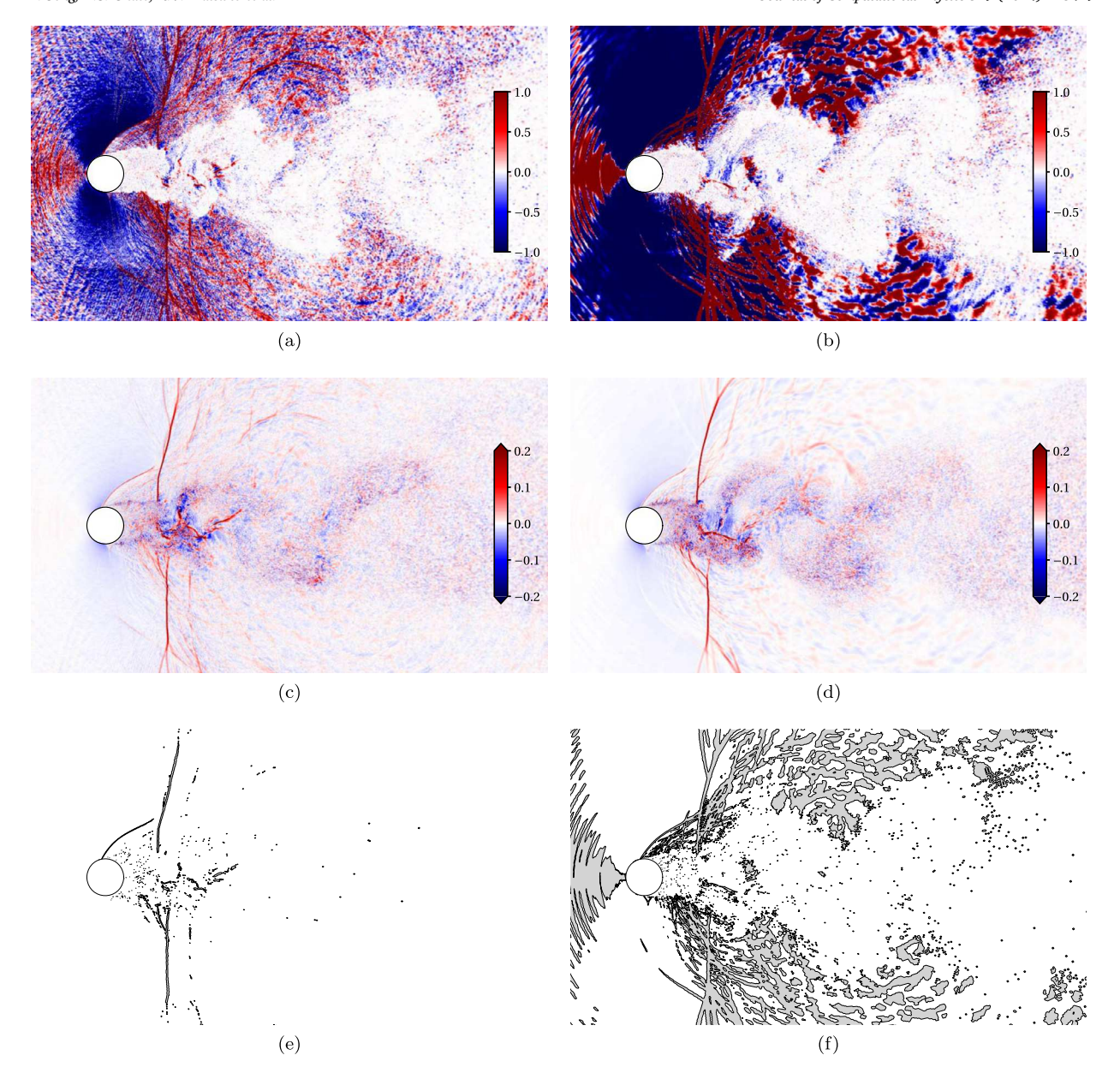


Fig. 44. Visualizations of shock sensors and central-Riemann flux hybridization in LES of transonic flow over a cylinder in Cases VI and VII: (a) and (b) are visualizations of the turbulence-based shock sensor values; (c) and (d) are visualizations of the acoustics-based shock sensor values; and in (e) and (f), the Riemann fluxes are used in the dark regions, and the central fluxes are used in the bright regions. The sub-figures in the left column, (a), (c), and (e), are from Case VI, and the sub-figures in the right column, (b), (d), and (f), are from Case VII. The simulations of Cases VI and VII start from the same initial conditions, and the visualizations are at the same computational time.

Different aspects of the numerical performance of the scheme are investigated using several demonstrative computations of 2D and 3D canonical flow configurations. The results indicate that high-order compact numerical schemes have significantly lower dispersion error and preserve coherent flow structures even on highly skewed curvilinear meshes. The LES of decaying isotropic turbulence shows that the framework is suitable for use with high-order compact schemes. The results relying on implicit numerical dissipation are overly dissipative compared to those simulated using explicit SGS models. Comprehensive use of the framework is demonstrated in the set of LES of flow over a cylinder. The robustness and accuracy are justified in both the low-Mach and transonic flow cases. For the transonic flow case, central-Riemann hybrid fluxes are used. The blending of primitive variables is self-controlled by two physics-based shock sensors. The simulation results show that the turbulent flow structures and acoustic wave structures are preserved by central fluxes with the SGS model only and are not affected by the numerical dissipation added from the shock-capturing scheme and the approximate Riemann solver.

#### CRediT authorship contribution statement

Hang Song: Conceptualization, Methodology, Software, Validation, Formal analysis, Investigation, Visualization, Writing – original draft, Writing – review & editing. Aditya S. Ghate: Writing – review & editing, Validation, Software, Methodology, Conceptualization. Kristen V. Matsuno: Writing – review & editing, Validation, Software. Jacob R. West: Writing – review & editing, Validation, Software. Akshay Subramaniam: Writing – review & editing, Validation, Software. Sanjiva K. Lele: Writing – review & editing, Validation, Supervision, Project administration.

#### **Declaration of competing interest**

The authors declare that they have no known competing financial interests or personal relationships that could have appeared to influence the work reported in this paper.

#### Data availability

No data was used for the research described in the article.

#### Acknowledgements

This work is supported by the National Science Foundation (NSF), grant number NSF-OAC-2103509. The code development used resources from the Extreme Science and Engineering Discovery Environment (XSEDE) and the Advanced Cyberinfrastructure Coordination Ecosystem: Services & Support (ACCESS), supported by NSF, and resources at the Texas Advanced Computing Center (TACC) at The University of Texas at Austin. The large-scale demonstrative simulations were supported by ALCC and INCITE allocations and run on the *Summit* supercomputer from the Oak Ridge Leadership Computing Facility (OLCF), which is supported by the Office of Science of the U.S. Department of Energy under contract DE-AC05-000R22725.

The authors are thankful to Prof. Parviz Moin (Stanford University) for the valuable comments on the contents of this work. The authors are grateful to Dr. Man-Long Wong (Stanford University) for the helpful discussions on high-order numerical methods and shock-capturing schemes and Prof. Lin Fu (HKUST) for the valuable comments on the derivations and implementations of high-order nonlinear interpolation schemes for shock capturing. The authors acknowledge Lucy J. Brown (Stanford University) for the useful feedback while using the computational code, which led to this work, in its early stages. The authors would also like to express their appreciation to Anjini Chandra (Stanford University) and Andy Wu (Stanford University) for providing comments and suggestions during drafting and revision. Lastly, the authors would like to thank the reviewers for their helpful comments and suggestions on improving the contents of this work during revision.

# Appendix A. Truncation error estimation of the linear advection-diffusion system

Considering a one-dimensional linear advection-diffusion process, the modified equation, Eq. (20), can be written in the following form.

$$\frac{d\widehat{\phi}}{dt} + (ikv' + k^2v')\,\widehat{\phi} = 0\tag{A.1}$$

where, without loss of generality, k, v' and v' can be interpreted as the x-component of the wavenumber, modified spectral advective velocity, and modified spectral diffusivity respectively. The complete definitions and explanations of v' and v' are given in Sec. 2. Compared to the exact operations, the truncation error can be quantified in Fourier space.

$$\frac{d\widehat{\phi}}{dt} + (ikV + k^2 v)\,\widehat{\phi} = \widehat{\epsilon}_{\text{adv}} + \widehat{\epsilon}_{\text{dif}} \tag{A.2}$$

where  $\hat{\epsilon}_{adv}$  and  $\hat{\epsilon}_{dif}$  denote the spectral truncation error generated from the numerical advection operator and diffusion operator respectively.

$$\hat{\epsilon}_{\text{adv}} = ikV \left(1 - v'/V\right) \hat{\phi}$$
 and  $\hat{\epsilon}_{\text{dif}} = k^2 v \left(1 - v'/v\right) \hat{\phi}$  (A.3, A.4)

For  $v'(k\Delta x)$  and  $v'(k\Delta x)$ , when evaluated using a Taylor series about  $k\Delta x=0$ , it can be easily shown that 1-v'(0)/V=0 and 1-v'(0)/v=0 are satisfied for a consistent discretization. Therefore, the general forms for  $\widehat{\epsilon}_{\rm adv}$  and  $\widehat{\epsilon}_{\rm dif}$  can be denoted as

$$\hat{\epsilon}_{\text{adv}} = -ikV\hat{\phi} \sum_{n=1}^{\infty} \left[ \frac{1}{n!} \left. \frac{d^n(v'/V)}{d(k\Delta x)^n} \right|_{k\Delta x = 0} (k\Delta x)^n \right]$$
(A.5)

$$\hat{\epsilon}_{\text{dif}} = -k^2 \nu \hat{\phi} \sum_{n=1}^{\infty} \left[ \frac{1}{n!} \frac{d^n (\nu'/\nu)}{d(k\Delta x)^n} \Big|_{k\Delta x = 0} (k\Delta x)^n \right]$$
(A.6)

which enables calculation of the leading-order truncation error of specific schemes from their spectral behaviors.

**Table A.3**Leading-order truncation errors in calculations of the model one-dimensional linear advection-diffusion equation on a periodic domain.

Order	$\epsilon_{ m adv}/V$		$\epsilon_{ m dif}/ u$			
	Collocated schemes	Staggered schemes	Collocated schemes	Staggered schemes		
2	$-\frac{1}{6}\left[\frac{\partial^3\phi}{\partial x^3}\right]\Delta x^2$	$-\frac{1}{6} \left[ \frac{\partial^3 \phi}{\partial x^3} \right] \Delta x^2$	$\frac{1}{3} \left[ \frac{\partial^4 \phi}{\partial x^4} \right] \Delta x^2$	$\frac{1}{12} \left[ \frac{\partial^4 \phi}{\partial x^4} \right] \Delta x^2$		
4	$\frac{1}{30} \left[ \frac{\partial^5 \phi}{\partial x^5} \right] \Delta x^4$	$\frac{9}{320} \left[ \frac{\partial^5 \phi}{\partial x^5} \right] \Delta x^4$	$-\frac{1}{15}\left[\frac{\partial^6\phi}{\partial x^6}\right]\Delta x^4$	$-\frac{3}{320}\left[\frac{\partial^6\phi}{\partial x^6}\right]\Delta x^4$		
6	$-\frac{1}{2100}\left[\frac{\partial^7\phi}{\partial x^7}\right]\Delta x^6$	$-\frac{59}{89600}\left[\frac{\partial^7\phi}{\partial x^7}\right]\Delta x^6$	$\frac{1}{1050} \left[ \frac{\partial^8 \phi}{\partial x^8} \right] \Delta x^6$	$\frac{61}{179200} \left[ \frac{\partial^8 \phi}{\partial x^8} \right] \Delta x^6$		

For the collocated scheme specified in Eq. (1),  $v'/V = (k'\Delta x)/(k\Delta x)$  and  $v'/v = (k'\Delta x)^2/(k\Delta x)^2$ . The modified wavenumber is given in Eq. (13). Considering the constraints on the coefficients given in Eq. (2) and Eq. (3) for a formally fourth-order derivative approximation, the Taylor-expansion approximations are

$$\hat{\epsilon}_{\text{adv}} = -V\hat{\phi} \left\{ (ik)^5 \frac{3\alpha - 1}{30(2\alpha + 1)} \Delta x^4 - (ik)^7 \frac{18\alpha^2 - 10\alpha + 1}{252(2\alpha + 1)^2} \Delta x^6 \right\} + \mathcal{O}\left(\Delta x^8\right)$$
(A.7)

and

$$\widehat{\epsilon}_{\text{dif}} = \nu \widehat{\phi} \left\{ (ik)^6 \frac{3\alpha - 1}{15(2\alpha + 1)} \Delta x^4 - (ik)^8 \frac{18\alpha^2 - 10\alpha + 1}{126(2\alpha + 1)^2} \Delta x^6 \right\} + \mathcal{O}\left(\Delta x^8\right)$$
(A.8)

The results indicate that the truncation errors in physical space are

$$\epsilon_{\text{adv}} = -V \left\{ \frac{3\alpha - 1}{30(2\alpha + 1)} \left[ \frac{\partial^5 \phi}{\partial x^5} \right] \Delta x^4 - \frac{18\alpha^2 - 10\alpha + 1}{252(2\alpha + 1)^2} \left[ \frac{\partial^7 \phi}{\partial x^7} \right] \Delta x^6 \right\} + \mathcal{O}\left(\Delta x^8\right)$$
(A.9)

and

$$\epsilon_{\rm dif} = \nu \left\{ \frac{3\alpha - 1}{15(2\alpha + 1)} \left[ \frac{\partial^6 \phi}{\partial x^6} \right] \Delta x^4 - \frac{18\alpha^2 - 10\alpha + 1}{126(2\alpha + 1)^2} \left[ \frac{\partial^8 \phi}{\partial x^8} \right] \Delta x^6 \right\} + \mathcal{O}\left(\Delta x^8\right)$$
 (A.10)

For the staggered derivative and midpoint interpolation schemes specified in Eq. (4) and Eq. (7) respectively,  $v'/V = [T(k\Delta x)] (k'\Delta x)/(k\Delta x)$  and  $v'/v = (k'\Delta x)^2/(k\Delta x)^2$ . The transfer function of the midpoint interpolation scheme,  $T(k\Delta x)$ , is given in Eq. (17), and the modified wavenumber of the staggered derivative scheme is given in Eq. (14). For the formally fourth-order discretization, the truncated Taylor series of  $\hat{\epsilon}_{adv}$  is

$$\widehat{\epsilon}_{\text{adv}} = -V\widehat{\phi} \left\{ (ik)^5 \frac{212\alpha_D\alpha_I - 14\alpha_D + 66\alpha_I - 27}{960 \left( 2\alpha_I + 1 \right) \left( 2\alpha_D + 1 \right)} \Delta x^4 - (ik)^7 \frac{1376\alpha_D^2\alpha_I^2 - 52\alpha_D^2\alpha_I + 844\alpha_D\alpha_I^2 + 134\alpha_D^2 - 584\alpha_D\alpha_I + 246\alpha_I^2 + \alpha_D - 111\alpha_I + 9}{4032 \left( 2\alpha_D + 1 \right)^2 \left( 2\alpha_I + 1 \right)^2} \Delta x^6 \right\} + \mathcal{O}\left( \Delta x^8 \right)$$
(A.11)

where the subscripts "D" and "I" are used for the coefficients of staggered derivative and midpoint interpolation schemes respectively. The truncated Taylor series of  $\hat{\epsilon}_{\text{dif}}$  is

$$\hat{\epsilon}_{\text{dif}} = \nu \hat{\phi} \left\{ (ik)^6 \frac{62\alpha - 9}{960(2\alpha + 1)} \Delta x^4 - (ik)^8 \frac{820\alpha^2 - 244\alpha + 9}{16128(2\alpha + 1)^2} \Delta x^6 \right\} + \mathcal{O}\left(\Delta x^8\right)$$
(A.12)

The results indicate that the truncation errors in physical space are

$$\epsilon_{\text{adv}} = -V \left\{ \frac{212\alpha_{D}\alpha_{I} - 14\alpha_{D} + 66\alpha_{I} - 27}{960\left(2\alpha_{I} + 1\right)\left(2\alpha_{D} + 1\right)} \left[ \frac{\partial^{5}\phi}{\partial x^{5}} \right] \Delta x^{4} - \frac{1376\alpha_{D}^{2}\alpha_{I}^{2} - 52\alpha_{D}^{2}\alpha_{I} + 844\alpha_{D}\alpha_{I}^{2} + 134\alpha_{D}^{2} - 584\alpha_{D}\alpha_{I} + 246\alpha_{I}^{2} + \alpha_{D} - 111\alpha_{I} + 9}{4032\left(2\alpha_{D} + 1\right)^{2}\left(2\alpha_{I} + 1\right)^{2}} \left[ \frac{\partial^{7}\phi}{\partial x^{7}} \right] \Delta x^{6} \right\} + \mathcal{O}\left(\Delta x^{8}\right)$$
(A.13)

and

$$\epsilon_{\rm dif} = \nu \left\{ \frac{62\alpha - 9}{960(2\alpha + 1)} \left[ \frac{\partial^6 \phi}{\partial x^6} \right] \Delta x^4 - \frac{820\alpha^2 - 244\alpha + 9}{16128(2\alpha + 1)^2} \left[ \frac{\partial^8 \phi}{\partial x^8} \right] \Delta x^6 \right\} + \mathcal{O}\left(\Delta x^8\right)$$
(A.14)

The same procedure can be applied in combining second-order schemes. The modified wavenumber profiles are  $k'\Delta x = \sin(k\Delta x)$  and  $k'\Delta x = 2\sin(\frac{1}{2}k\Delta x)$  for the collocated and staggered derivative schemes respectively, and the transfer function for the midpoint interpolation scheme is  $T(k\Delta x) = \cos(\frac{1}{2}k\Delta x)$ . For fourth-order explicit schemes,  $\alpha$  for all schemes is set to 0, and the values of  $\alpha$ 

for sixth-order compact schemes are provided in Table 1. The leading-order truncation errors of the model equation computed using different combinations of central schemes are shown in Table A.3

#### Appendix B. Subgrid-scale models used in the demonstrative simulations

The large-eddy simulation (LES) system solved in this work is interpreted as the Favre-filtered system with respect to the velocity and temperature fields [75,76]. No subgrid-scale (SGS) model is applied to mass conservation, Eq. (23), and the SGS models in momentum conservation, Eq. (24), and energy conservation, Eq. (25), are formulated as the turbulent viscosity and conductivity respectively according to the Boussinesq hypothesis [16]. Therefore, the overall dynamic viscosity,  $\mu$ , and thermal conductivity,  $\kappa$ , used with the Navier-Stokes system are

$$\mu = \check{\mu} + \mu_{SGS}$$
 and  $\kappa = \check{\kappa} + \kappa_{SGS}$  (B.1, B.2)

where  $\check{\mu}$  and  $\check{\kappa}$  are the computable dynamic viscosity and thermal conductivity respectively, and  $\mu_{SGS}$  and  $\kappa_{SGS}$  are the modeled turbulent viscosity and conductivity respectively.

In this work,  $\mu_{SGS}$  is calculated using the Vreman SGS model [14]. The calculation method is summarized in the following equations.

$$\mu_{\text{SGS}} = \rho C_{\text{SGS}} \Delta^2 \sqrt{B[m]/\|\nabla u\|_F^2}$$
(B.3)

where  $\Delta$  is a length scale characterizing the grid spacing. On a uniform Cartesian mesh and curvilinear mesh,  $\Delta$  are calculated as

$$\Delta = \sqrt[3]{\Delta x \Delta y \Delta z}$$
 and  $\Delta = \sqrt[3]{J}$ 

respectively, where  $\Delta x$ ,  $\Delta y$ , and  $\Delta z$  are the grid spacings on the uniform Cartesian mesh along the x-, y-, and z-directions respectively, and J is the metric Jacobian assuming the grid spacing of the reference mesh is unity in all directions. For the applications shown in this work, the treatment in the calculation of  $\Delta$  with respect to the grid anisotropy is ignored. The Frobenius norm of the resolved velocity gradient tensor is computed as

$$\|\nabla \boldsymbol{u}\|_F^2 = u_{i,j}u_{i,j}$$

B[m] is a functional that takes in a  $3 \times 3$  symmetric semi-positive-definite tensor m, defined as

$$B[\mathbf{m}] = \frac{1}{2} \delta_{ij} \varepsilon_{ikl} \varepsilon_{jpq} m_{kp} m_{lq}$$

Finally, the tensor m is defined as

$$m_{ij} = u_{i,k}u_{j,k}$$

 $\kappa_{SGS}$  is calculated based on a constant turbulent Prandtl number,  $Pr_t$ 

$$\kappa_{\text{SGS}} = c_p \mu_{\text{SGS}} / \text{Pr}_t$$
 (B.4)

where  $c_n$  is the specific heat at a constant pressure.

## Appendix C. Calculation of metrics using compact numerical schemes on a periodic domain

Given a pair of periodic "boundaries,"  $\partial B_a$  and  $\partial B_b$ , for  $\forall x_a \in \partial B_a$ ,  $\exists x_b \in \partial B_b$  such that

$$x_b = Qx_a + I \tag{C.1}$$

where Q is an orthogonal tensor denoting rigid rotation, and I represents rigid translation. At the mapped locations in the pair of periodic boundaries, all physical quantities are equivalent. According to the mapping in Eq. (C.1), a scalar quantity field,  $\phi$ , at the pair of periodic boundaries satisfies  $\phi(x_b) = \phi(x_a)$ , and a vector field, v, satisfies  $v(x_b) = Qv(x_a)$ . Q is an identity tensor for a translationally-periodic boundary.

$$x_b = x_a + l \tag{C.2}$$

As a result, each component in the vector field can be mapped individually, and each component in a tensor field can be smoothed over the entire domain including across the periodic boundary. In this work, only translationally-periodic boundaries are considered with the mapping formulated in Eq. (C.2).

Nevertheless, the physical coordinates may still be discontinuous across the periodic boundary unless l=0 as in the demonstrative simulations in Sec. 4.5 in the azimuthal direction. Therefore, the compact schemes used for generation of the metric tensor, illustrated in Sec. 3.4, require the following modifications along the periodic dimension to avoid discontinuity or inconsistency. The modifications are illustrated using the sixth-order compact differential schemes and interpolation schemes used in this work, and the methods can be easily generalized for different compact schemes.

For staggered differentiation of the coordinate along the periodic dimension, according to Eq. (4), the linear system can be formulated as

$$\begin{bmatrix} 1 & \alpha & 0 & \cdots & 0 & 0 & \alpha \\ \alpha & 1 & \alpha & \cdots & 0 & 0 & 0 \\ 0 & \alpha & 1 & \cdots & 0 & 0 & 0 \\ \vdots & \vdots & \vdots & \ddots & \vdots & \vdots & \vdots \\ 0 & 0 & 0 & \cdots & 1 & \alpha & 0 \\ 0 & 0 & 0 & \cdots & \alpha & 1 & \alpha \\ \alpha & 0 & 0 & \cdots & 0 & \alpha & 1 \end{bmatrix} \begin{bmatrix} (\partial x)_0 \\ (\partial x)_1 \\ (\partial x)_2 \\ \vdots \\ (\partial x)_{N-3} \\ (\partial x)_{N-2} \\ (\partial x)_{N-1} \end{bmatrix} = a \begin{bmatrix} x_{1/2} - x_{-1/2} \\ x_{3/2} - x_{1/2} \\ x_{5/2} - x_{3/2} \\ \vdots \\ x_{N-5/2} - x_{N-7/2} \\ x_{N-3/2} - x_{N-5/2} \\ x_{N-3/2} - x_{N-5/2} \\ x_{N-1/2} - x_{N-3/2} \end{bmatrix} + \frac{b}{3} \begin{bmatrix} x_{3/2} - x_{-3/2} \\ x_{5/2} - x_{-1/2} \\ x_{7/2} - x_{1/2} \\ \vdots \\ x_{N-3/2} - x_{N-9/2} \\ x_{N-1/2} - x_{N-7/2} \\ x_{N-1/2} - x_{N-5/2} \end{bmatrix}$$
(C.3)

where x represents an arbitrary component of the coordinate system and  $\partial x$  denotes a metric component corresponding to x. The mesh spacing in the reference domain is set to be unity. Assuming that there are N grid points along the periodic dimension, the coordinate, with its subscript from 0 to N-1, is represented by the computational mesh. Based on the rigid translation, the out-of-bounds coordinates in Eq. (C.3) are calculated as

$$x_{-i} = x_{N-i} - l$$
 and  $x_{N+i} = x_i + l$  for  $0 \le j < N$  (C.4, C.5)

where l is the translational period in such a dimension.

For periodic coordinate interpolation, according to Eq. (7), at the first and last grid points, the equations are

$$\alpha x_{-1/2} + x_{1/2} + \alpha x_{3/2} = \frac{a}{2} (x_0 + x_1) + \frac{b}{2} (x_{-1} + x_2)$$
(C.6)

$$\alpha x_{N-3/2} + x_{N-1/2} + \alpha x_{N+1/2} = \frac{a}{2} \left( x_{N-1} + x_N \right) + \frac{b}{2} \left( x_{N-2} + x_{N+1} \right) \tag{C.7}$$

where the out-of-bounds coordinates on the right-hand sides of the equations can still be calculated using the relations given in Eq. (C.4) and Eq. (C.5). However, the out-of-bounds coordinates on the left-hand sides of the equations are extra unknowns that are not directly solvable from the linear system. To address this, Eq. (C.4) and Eq. (C.5) are imposed to modify Eq. (C.6) and Eq. (C.7) so that  $x_{-1/2}$  and  $x_{N+1/2}$  will be substituted with  $x_{N-1/2}$  and  $x_{N+1/2}$  are result, the solvable linear system is formulated as

$$\begin{bmatrix} 1 & \alpha & 0 & \cdots & 0 & 0 & \alpha \\ \alpha & 1 & \alpha & \cdots & 0 & 0 & 0 \\ 0 & \alpha & 1 & \cdots & 0 & 0 & 0 \\ \vdots & \vdots & \vdots & \ddots & \vdots & \vdots & \vdots \\ 0 & 0 & 0 & \cdots & 1 & \alpha & 0 \\ 0 & 0 & 0 & \cdots & \alpha & 1 & \alpha \\ \alpha & 0 & 0 & \cdots & 0 & \alpha & 1 \end{bmatrix} \begin{bmatrix} x_{1/2} \\ x_{3/2} \\ x_{5/2} \\ \vdots \\ x_{N-5/2} \\ x_{N-3/2} \\ x_{N-1/2} \end{bmatrix} = \underbrace{a}_{1} \begin{bmatrix} x_{0} + x_{1} \\ x_{1} + x_{2} \\ x_{2} + x_{3} \\ \vdots \\ x_{N-3} + x_{N-2} \\ x_{N-2} + x_{N-1} \\ x_{N-1} + x_{N} \end{bmatrix} + \underbrace{b}_{2} \begin{bmatrix} x_{-1} + x_{2} \\ x_{0} + x_{3} \\ x_{1} + x_{4} \\ \vdots \\ x_{N-4} + x_{N-1} \\ x_{N-3} + x_{N} \\ x_{N-2} + x_{N+1} \end{bmatrix} + \alpha \begin{bmatrix} l \\ 0 \\ 0 \\ \vdots \\ 0 \\ 0 \\ -l \end{bmatrix}$$
 (C.8)

where the last term on the right-hand side is caused by modifying the out-of-bounds coordinates on the left-hand side.

# Appendix D. Boundary and near-boundary schemes

Along a non-periodic dimension, one-sided schemes are applied. The detailed derivations of one-sided schemes for collocated differentiation, staggered differentiation, and midpoint interpolation are discussed in Ref. [19] and Ref. [43] respectively. In this work, the physical boundary is placed at the first (or last) edge-staggered point, which is a half-grid spacing from the first (or last) nodal point on the interior side. The boundary scheme associated with the collocated sixth-order compact finite difference method shown in Eq. (1) is

$$f_0' + 3f_1' = \frac{1}{\Delta \xi} \left( -\frac{17}{6} f_0 + \frac{3}{2} f_1 + \frac{3}{2} f_2 - \frac{1}{6} f_3 \right) \tag{D.1}$$

This discretization makes the boundary scheme formally fourth-order accurate. At the first near-boundary point, the most compact fourth-order central discretization is used.

$$\frac{1}{4}f_0' + f_1' + \frac{1}{4}f_2' = \frac{3}{4}(f_2 - f_0)/\Delta\xi \tag{D.2}$$

At the second near-boundary point, a fourth-order central scheme with a wider stencil is used.

$$\frac{163}{508}f_1' + f_2' + \frac{163}{508}f_3' = \frac{393}{508} \left(f_3 - f_1\right) / \Delta \xi + \frac{3}{127} \left(f_4 - f_0\right) / \Delta \xi \tag{D.3}$$

Starting from the third near-boundary point, the interior scheme is applied. The schematic of boundary and near-boundary stencils associated with the collocated sixth-order compact finite difference method scheme is shown in Fig. D.45.

The boundary scheme of the node-to-edge staggered differentiation scheme, shown in Eq. (4) by shifting the grid-point indices, that is used for the calculations of gradient components is

Fig. D.45. Schematic of the collocated differentiation near a boundary.

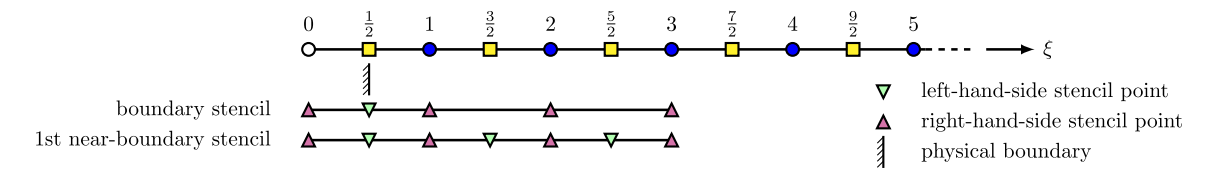


Fig. D.46. Schematic of the one-dimensional node-to-edge differentiation and interpolation near a boundary.

$$f'_{1/2} = \frac{1}{\Delta \xi} \left( -\frac{23}{24} f_0 + \frac{7}{8} f_1 + \frac{1}{8} f_2 - \frac{1}{24} f_3 \right) \tag{D.4}$$

This form is formally third-order accurate, and a Dirichlet boundary condition is imposed from the value set at the ghost point,  $f_0$ . Since the boundary scheme is an explicit scheme, it is one-way coupled with the linear system to determine the derivatives at the near-boundary and interior points at the edge-staggered locations. At the first near-boundary point, the scheme is a compact fourth-order central scheme.

$$\frac{37}{183}f'_{1/2} + f'_{3/2} + \frac{37}{183}f'_{5/2} = \frac{475}{488} (f_2 - f_1) / \Delta \xi + \frac{631}{4392} (f_3 - f_0) / \Delta \xi$$
(D.5)

Starting from the second near-boundary point, the interior scheme is applied. The stencils of the boundary and near-boundary schemes associated with the node-to-edge staggered derivative schemes are shown in Fig. D.46.

The boundary scheme of the node-to-edge interpolation associated with the compact interpolation scheme shown in Eq. (7) is

$$f_{1/2}^{I} = \frac{5}{16}f_0 + \frac{15}{16}f_1 - \frac{5}{16}f_2 + \frac{1}{16}f_3 \tag{D.6}$$

This form yields a fourth-order explicit interpolation, and the boundary scheme is one-way coupled with the linear system to determine the interpolated values at near-boundary and interior edge-staggered points, similar to the node-to-edge differentiation. At the first near-boundary point, the scheme is set to be a fourth order scheme.

$$\frac{1}{4}f_{1/2}^{I} + f_{3/2}^{I} + \frac{1}{4}f_{5/2}^{I} = \frac{23}{32}(f_2 + f_1) + \frac{1}{32}(f_3 + f_0)$$
(D.7)

Starting from the second near-boundary point, the interior scheme is applied. The boundary and near-boundary stencils associated with the interpolation schemes are also shown in Fig. D.46.

The edge-to-node differentiation that is used for the divergence operator includes a ghost point beyond the physical boundary. The scheme at the ghost point is in an explicit sided form.

$$f_0' = \frac{1}{\Delta \xi} \left( -\frac{71}{24} f_{1/2} + \frac{47}{8} f_{3/2} - \frac{31}{8} f_{5/2} + \frac{23}{24} f_{7/2} \right) \tag{D.8}$$

The discretization is formally third-order accurate with dissipative leading order truncation error. Similar to the node-to-edge derivative and interpolation schemes, by setting the off-diagonal coefficient to zero, the boundary scheme is one-way coupled with the near boundary and interior schemes. The actual boundary scheme uses the most compact fourth-order central difference method as follows:

$$\frac{1}{22}f_0' + f_1' + \frac{1}{22}f_2' = \frac{12}{11} \left( f_{3/2} - f_{1/2} \right) / \Delta \xi \tag{D.9}$$

The combination of Eq. (D.8) and Eq. (D.9) results in a compact one-sided scheme at the boundary stencil. The scheme at the first near-boundary stencil is

$$\frac{9089}{69564}f_1' + f_2' + \frac{9089}{69564}f_3' = \frac{95257}{92752} \left(f_{5/2} - f_{3/2}\right) / \Delta \xi + \frac{5927}{75888} \left(f_{7/2} - f_{1/2}\right) / \Delta \xi \tag{D.10}$$

Starting from the second near-boundary stencil, the interior scheme is used. The boundary and near-boundary stencils associated with the staggered central difference schemes are shown in Fig. D.47.

With the physical boundary placed at the edge-staggered point, the boundary conditions are weakly imposed on the Navier-Stokes system via fluxes. This treatment enhances robustness and provides the flexibility to impose different types of boundary conditions.

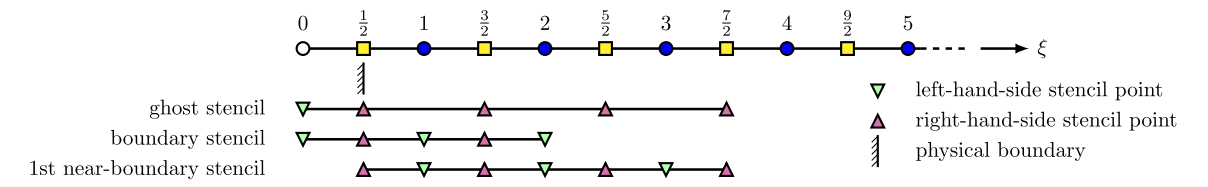


Fig. D.47. Schematic of the one-dimensional edge-to-node differentiation near a boundary.

In this work, the boundary conditions for the simulations in Sec. 4.5 are imposed by setting the variables at the ghost nodal points prior to calculating the variables at the edge-staggered points (cf. Sec. 3.2 and Sec. 3.3).

#### Appendix E. Shock-capturing methods

The methods for shock capturing used in this work are documented in this section. The localized artificial diffusivity (LAD) model is described in Appendix E.1. The nonlinear interpolation schemes and the approximate Riemann solver are illustrated in Appendix E.2 and Appendix E.3 respectively. The LAD model and the nonlinear interpolation scheme combined with an approximate Riemann solver are two independent methods for shock capturing. In this work, these two approaches are not mixed in the same simulation. This work proposes that the latter method should be hybridized with central schemes in simulations of compressible turbulent flows. The details are illustrated in Sec. 3.5 and Sec. 4.5.

#### E.1. Localized artificial diffusivity model

The LAD model used in this work is primarily based on the formulation given in Ref. [56] and Ref. [37]. For shock capturing, only artificial bulk viscosity and thermal conductivity models are used. The artificial diffusivities are added to the overall bulk viscosity,  $\beta$ , and thermal conductivity,  $\kappa$ , in the Navier-Stokes equations described in Sec. 3.1.

$$\beta = \check{\beta} + \beta^*$$
 and  $\kappa = \check{\kappa} + \kappa^*$  (E.1, E.2)

where  $\check{\beta}$  and  $\check{\kappa}$  are calculated using the physical bulk viscosity and thermal conductivity models respectively, and  $\beta^*$  and  $\kappa^*$  are the artificial bulk viscosity and thermal conductivity respectively. On Cartesian meshes, the artificial diffusivities are formulated as

$$\beta^* = C_{\beta} \mathcal{G} \left\{ \rho \mathcal{H} \left( \frac{-\theta |\theta|}{\theta^2 + \omega_i \omega_i + \varepsilon^2} \right) \middle| D_{mpql} \frac{\partial^4 \theta}{\partial x_m \partial x_p \partial x_q \partial x_l} \middle| \left( \Delta x_j \frac{\partial \rho}{\partial x_j} \right)^2 \left( \frac{\partial \rho}{\partial x_k} \frac{\partial \rho}{\partial x_k} + \varepsilon^2 \right)^{-1} \right\}$$
 (E.3)

$$\kappa^* = C_{\kappa} \mathcal{G} \left\{ \frac{\rho c}{T} \left| D_{mpql} \frac{\partial^4 e_{\text{th}}}{\partial x_m \partial x_p \partial x_q \partial x_l} \right| \sqrt{\left(\Delta x_j \frac{\partial e_{\text{th}}}{\partial x_j}\right)^2 \left(\frac{\partial e_{\text{th}}}{\partial x_k} \frac{\partial e_{\text{th}}}{\partial x_k} + \varepsilon^2\right)^{-1}} \right\}$$
(E.4)

where  $C_{\beta}$  and  $C_{\kappa}$  are the model constants for  $\beta^*$  and  $\kappa^*$  respectively,  $\mathcal{G}(\cdot)$  denotes the truncated Gaussian filter [77],  $\mathcal{H}(\cdot)$  denotes the Heaviside step function,  $\rho$  is density, c is the speed of sound, T is temperature,  $e_{\text{th}}$  is internal energy,  $\theta = u_{k,k}$  is the velocity dilatation,  $\omega_i$  is the vorticity vector,  $\varepsilon = 1 \times 10^{-16}$  serves as numerical regulation, and  $\Delta x_j$  is the grid spacing in the j-th dimension.  $D_{mpql}$  is a fourth-order tensor operator. The early version proposed in Ref. [39] uses  $D_{mpql} = (\Delta x \Delta y \Delta z)^{4/3} \delta_{mp} \delta_{ql}$ . In Ref. [56] and Ref. [37], based on the consideration of the computational cost, especially for curvilinear meshes, the operation of  $D_{mpql}$  is reduced as  $D_{mpql} = \Delta x_m^4$  if m = p = q = l, otherwise  $D_{mpql} = 0$ . This design makes the operation  $D_{mpql} \partial_{x_m} \partial_{x_p} \partial_{x_q} \partial_{x_l}$  the sum of undivided fourth derivatives in all dimensions. The terms  $\sqrt{(\Delta x_j \rho_{,j})^2/(\rho_{,k} \rho_{,k})}$  and  $\sqrt{(\Delta x_j e_{\text{th},j})^2/(e_{\text{th},k} e_{\text{th},k})}$  define the length scales considering both grid spacing in different directions and the obliqueness of shock waves indicated by the normalized density and internal energy gradient respectively. The fourth derivative is approximated using the following scheme [19].

$$\alpha f_{j-1}^{\prime\prime\prime\prime} + f_{j}^{\prime\prime\prime\prime} + \alpha f_{j+1}^{\prime\prime\prime\prime} = a \frac{f_{j-2} - 4f_{j-1} + 6f_{j} - 4f_{j+1} + f_{j+2}}{\Delta x^{4}} + b \frac{f_{j-3} - 9f_{j-1} + 16f_{j} - 9f_{j+1} + f_{j+3}}{6\Delta x^{4}} \tag{E.5}$$

where  $f_j''''$  denotes the numerical evaluation of  $\partial_x^4 f$  at  $x_j$ . For a formally fourth-order scheme, the coefficients satisfy the following constraints.

$$a = 2(1 - \alpha) \tag{E.6}$$

$$b = 4\alpha - 1 \tag{E.7}$$

If  $\alpha = 7/26$ , the scheme in Eq. (E.5) becomes formally sixth-order, and a = 19/13 and b = 1/13. In this work, the sixth-order scheme is used. The truncated Gaussian filter used is given by the following.

$$[\mathcal{G}(f)]_{j} = \frac{3565}{10368} f_{j} + \frac{3091}{12960} (f_{j+1} + f_{j-1}) + \frac{1997}{25920} (f_{j+2} + f_{j-2}) + \frac{149}{12960} (f_{j+3} + f_{j-3}) + \frac{107}{103680} (f_{j+4} + f_{j-4})$$
(E.8)

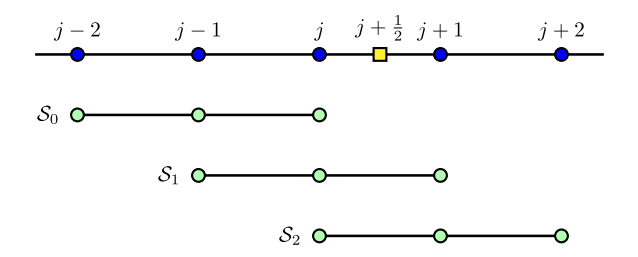


**Fig. E.48.** Candidate sub-stencils of the WENO5-JS interpolation scheme using nodal-point values within the stencil to approximate the edge-staggered value at j + 1/2.

#### E.2. Nonlinear interpolation schemes for shock-capturing

The concept of nonlinear interpolation schemes for shock-capturing referred to in this work is originally introduced in Ref. [63] and known as the weighted essentially non-oscillatory (WENO) method. The five-point-stencil scheme introduced in Ref. [63] is known as the WENO5-JS scheme. Consistent with the higher-order staggered finite difference schemes used for evaluating the flux divergence, the interpolation is used to preserve high-order convergence as opposed to the reconstruction scheme designed for the higher-order finite volume method or the finite difference method referred to in Ref. [54] where the flux difference operation is applied. Since many in literature have provided the discussions on the details of the WENO5-JS interpolation scheme and the schemes improved from it, only the key steps are documented.

The WENO5-JS interpolation scheme evaluates the value at j + 1/2 using three candidate sub-stencils,  $S_0$ ,  $S_1$  and  $S_2$ , within a five-point nodal stencil from j - 2 to j + 2 as shown in Fig. E.48. Each candidate sub-stencil provides an independent evaluation of the interpolated value at j + 1/2 using Lagrange interpolation.

$$f_{j+\frac{1}{2}}^{I}[S_0] = \frac{1}{8} \left( 3f_{j-2} - 10f_{j-1} + 15f_j \right)$$
 (E.9)

$$f_{j+\frac{1}{2}}^{I}[S_1] = \frac{1}{8} \left( -f_{j-1} + 6f_j + 3f_{j+1} \right)$$
(E.10)

$$f_{j+\frac{1}{2}}^{I}[S_2] = \frac{1}{8} \left( 3f_j + 6f_{j+1} - f_{j+2} \right)$$
 (E.11)

where  $f_{j+\frac{1}{2}}^{I}[S_k]$  denotes the numerically-interpolated value evaluated using the candidate sub-stencil  $S_k$ . Optimally, a convex superposition of the interpolated results from all three sub-stencils can form a fifth-order upwind-biased Lagrange interpolation.

$$d_0f_{j+\frac{1}{2}}^I[S_0] + d_1f_{j+\frac{1}{2}}^I[S_1] + d_2f_{j+\frac{1}{2}}^I[S_2] = \frac{1}{128} \left(3f_{j-2} - 20f_{j-1} + 90f_j + 60f_{j+1} - 5f_{j+2}\right) \tag{E.12}$$

where  $d_0 = 1/16$ ,  $d_1 = 5/8$ , and  $d_2 = 5/16$  are known as the linear or optimal weights. In practice, the convex combination may not use the linear weights, especially when the interpolated function is not smooth within the stencil, so a set of nonlinear weights are used to determine the interpolated values.

$$f_{j+\frac{1}{2}}^{I} = \omega_0 f_{j+\frac{1}{2}}^{I}[S_0] + \omega_1 f_{j+\frac{1}{2}}^{I}[S_1] + \omega_2 f_{j+\frac{1}{2}}^{I}[S_2]$$
 (E.13)

where the nonlinear weights,  $\omega_0,\,\omega_1,\,$  and  $\omega_2,\,$  are calculated as

$$\alpha_k = \frac{\alpha_k d_k}{\alpha_0 d_0 + \alpha_1 d_1 + \alpha_2 d_2} \quad \text{for} \quad k = 0, 1, 2$$
(E.14)

 $\alpha_k$  can be interpreted as a weighting score indicating the quality of the interpolated result from each candidate sub-stencil and is calculated as

$$\alpha_k = \left(\beta_k + \varepsilon\right)^{-p} \tag{E.15}$$

where  $\varepsilon$  and p are model parameters. In the demonstrations,  $\varepsilon = 1 \times 10^{-6}$  and p = 2 are used.  $\beta_k$  is known as the smoothness indicator measuring the non-smoothness of the discrete profile within the candidate sub-stencil  $S_k$  and is defined as

$$\beta_k = \sum_{l=1}^2 \Delta x^{2l-1} \int_{x_j - \frac{1}{2} \Delta x}^{x_j + \frac{1}{2} \Delta x} \left( \frac{\partial^l f[S_k]}{\partial x^l} \right)^2 dx \tag{E.16}$$

The smooth function  $f\left[S_k\right]$  is the Lagrange polynomial constructed using all the nodal values within the candidate sub-stencil  $S_k$ . For WENO5-JS interpolation, the smoothness indicator of each sub-stencil specified in Fig. E.48 is calculated as follows:

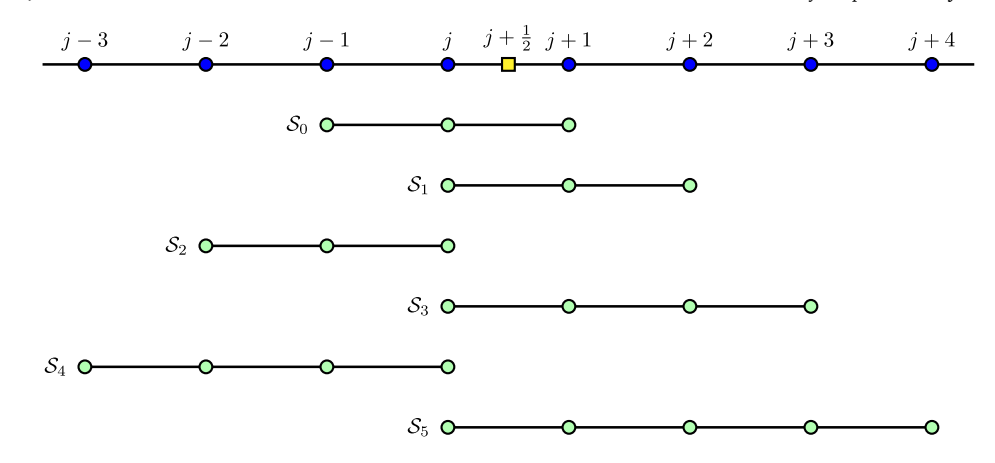


Fig. E.49. Candidate sub-stencils of the TENO8-A interpolation scheme using nodal-point values within the stencil to approximate the edge-staggered value at j + 1/2.

$$\beta_0 = \frac{13}{12} \left( f_{j-2} - 2f_{j-1} + f_j \right)^2 + \frac{1}{4} \left( f_{j-2} - 4f_{j-1} + 3f_j \right)^2 \tag{E.17}$$

$$\beta_1 = \frac{13}{12} \left( f_{j-1} - 2f_j + f_{j+1} \right)^2 + \frac{1}{4} \left( f_{j+1} - f_{j-1} \right)^2 \tag{E.18}$$

$$\beta_2 = \frac{13}{12} \left( f_j - 2f_{j+1} + f_{j+2} \right)^2 + \frac{1}{4} \left( f_{j+2} - 4f_{j+1} + 3f_j \right)^2 \tag{E.19}$$

The targeted essentially non-oscillatory (TENO) method is originally introduced in Ref. [78] and extended from classic WENO schemes. The method generalizes the design of candidate sub-stencils for higher-order methods and calculation of nonlinear weights. Additionally, the interpolation at optimal weights is consistent with central interpolation. These improvements successfully reduce undesirable dissipation and maintain robustness for strong shock capturing in higher-order simulations. Further improvements on the adaptive criterion while calculating nonlinear weights are provided in Ref. [60] for flux reconstruction in a high-order finite volume framework. The coefficients for interpolation are derived in the following context, and the evaluations of some model coefficients are slightly different from those described in Ref. [60].

In this work, the eighth-order adaptive TENO scheme is used and is referred to as the TENO8-A scheme. The scheme contains six candidate sub-stencils from  $S_0$  to  $S_5$  to interpolate the nodal values within an overall 8-point stencil to the edge-staggered point at j + 1/2 as shown in Fig. E.49. The individual Lagrange interpolation for each candidate sub-stencil is

$$f_{j+\frac{1}{2}}^{I}[S_0] = \frac{1}{8} \left( -f_{j-1} + 6f_j + 3f_{j+1} \right)$$
 (E.20)

$$f_{j+\frac{1}{2}}^{I}[S_1] = \frac{1}{8} \left( 3f_j + 6f_{j+1} - f_{j+2} \right)$$
 (E.21)

$$f_{j+\frac{1}{2}}^{I}[S_2] = \frac{1}{8} \left( 3f_{j-2} - 10f_{j-1} + 15f_j \right)$$
 (E.22)

$$f_{j+\frac{1}{3}}^{I}[S_3] = \frac{1}{16} \left( 5f_j + 15f_{j+1} - 5f_{j+2} + f_{j+3} \right)$$
 (E.23)

$$f_{j+\frac{1}{2}}^{I}[S_4] = \frac{1}{16} \left( -5f_{j-3} + 21f_{j-2} - 35f_{j-1} + 35f_j \right)$$
 (E.24)

$$f_{j+\frac{1}{2}}^{I}[S_{5}] = \frac{1}{128} \left( 35f_{j} + 140f_{j+1} - 70f_{j+2} + 28f_{j+3} - 5f_{j+4} \right)$$
 (E.25)

At optimal weights, the convex combination of the interpolated results from the sub-stencils equals the sixth-order central interpolation.

$$\sum_{k=0}^{5} d_k f_{j+\frac{1}{2}}^I [S_k] = \frac{1225}{2048} (f_j + f_{j+1}) - \frac{245}{2048} (f_{j-1} + f_{j+2}) + \frac{49}{2048} (f_{j-2} + f_{j+3}) - \frac{5}{2048} (f_{j-3} + f_{j+4})$$
 (E.26)

where the optimal weights are  $d_0=175/384$ ,  $d_1=105/384$ ,  $d_2=14/384$ ,  $d_3=63/384$ ,  $d_4=3/384$ , and  $d_5=24/384$ . The weighting score,  $\alpha_k$ , of each candidate sub-stencil  $S_k$  is calculated in the same way as formulated in Eq. (E.15) with  $\varepsilon=1\times 10^{-40}$  and p=6. Unlike the WENO method, TENO schemes further normalize  $\alpha_k$  to determine a binary pick-up mask function,  $\delta_k$ , for each candidate sub-stencil.

$$\delta_k = \mathcal{H}\left(\overline{\alpha}_k - C_T\right) \tag{E.27}$$

where  $\mathcal{H}(\cdot)$  denotes the Heaviside step function,  $\overline{\alpha}_k = \alpha_k / \left(\sum_{l=0}^5 \alpha_l\right)$  is a normalized weighting score, and  $C_T$  is a cut-off threshold which is dynamically determined for the adaptive method. The nonlinear weights  $\omega_k$  are determined as

$$\omega_k = \frac{\delta_k d_k}{\sum_{l=0}^5 \delta_l d_l} \tag{E.28}$$

and the nonlinear interpolated result is calculated as

$$f_{j+\frac{1}{2}}^{I} = \sum_{k=0}^{5} \omega_k f_{j+\frac{1}{2}}^{I} [S_k]$$
 (E.29)

The smoothness indicator,  $\beta_k$ , needed for calculation of  $\alpha_k$  for each candidate sub-stencil in the TENO8-A scheme is calculated as follows:

$$\beta_0 = \frac{1}{4}(f_{j+1} - f_{j-1})^2 + \frac{13}{12}(f_{j-1} - 2f_j + f_{j+1})^2$$
(E.30)

$$\beta_1 = \frac{1}{4}(3f_j - 4f_{j+1} + f_{j+2})^2 + \frac{13}{12}(f_j - 2f_{j+1} + f_{j+2})^2$$
(E.31)

$$\beta_2 = \frac{1}{4}(3f_j - 4f_{j-1} + f_{j-2})^2 + \frac{13}{12}(f_j - 2f_{j-1} + f_{j-2})^2$$
(E.32)

$$\beta_3 = \frac{1}{64} (15f_j - 25f_{j+1} + 13f_{j+2} - 3f_{j+3})^2 + \frac{13}{12} (2f_j - 5f_{j+1} + 4f_{j+2} - f_{j+3})^2$$
(E.33)

$$+\frac{61}{720}(f_j - 3f_{j+1} + 3f_{j+2} - f_{j+3})^2$$

$$\beta_4 = \frac{1}{64} (15f_j - 25f_{j-1} + 13f_{j-2} - 3f_{j-3})^2 + \frac{13}{12} (2f_j - 5f_{j-1} + 4f_{j-2} - f_{j-3})^2$$
(E.34)

$$+\frac{61}{720}(f_j-3f_{j-1}+3f_{j-2}-f_{j-3})^2$$

$$\beta_5 = \frac{1}{256} (35f_j - 70f_{j+1} + 56f_{j+2} - 26f_{j+3} + 5f_{j+4})^2$$
(E.35)

$$+\frac{1}{2246400}(4613f_j - 13772f_{j+1} + 15198f_{j+2} - 7532f_{j+3} + 1493f_{j+4})^2$$

$$+\frac{61}{2880}(5f_{j}-18f_{j+1}+24f_{j+2}-14f_{j+3}+3f_{j+4})^{2}+\frac{1861}{1310400}(f_{j}-4f_{j+1}+6f_{j+2}-4f_{j+3}+f_{j+4})^{2}$$

The cut-off threshold,  $C_T$ , in Eq. (E.27) is calculated based on the definition of the local nodal smoothness indicator,  $\mu_j$ , which is defined as

$$\mu_{j} = \frac{2\left| (f_{j+1} - f_{j})(f_{j} - f_{j-1}) \right| + \varepsilon_{\mu}}{\left( f_{j+1} - f_{j} \right)^{2} + \left( f_{j} - f_{j-1} \right)^{2} + \varepsilon_{\mu}} \tag{E.36}$$

where the numerical regularization factor,  $\varepsilon_{\mu}$ , is determined as

$$\varepsilon_{\mu} = \frac{0.9c_r}{1 - 0.9c} \varepsilon_{\mu,0} \tag{E.37}$$

 $\varepsilon_{\mu}$  is statically calculated with tunable model constants  $c_r$  and  $\varepsilon_{\mu,0}$ . As suggested in Ref. [60],  $c_r = 0.23$  and  $\varepsilon_{\mu,0} = 1 \times 10^{-6}$  are used, which leads to  $\varepsilon_{\mu} = (207/793) \times 10^{-6}$ . A complementary indicator,  $\sigma$ , is defined using  $\mu_i$  in a narrower stencil.

$$\sigma = 1 - \min \left\{ 1, \min \left\{ \mu_{i-1}, \mu_i, \mu_{i+1}, \mu_{i+2} \right\} / c_r \right\}$$
 (E.38)

Finally, the cut-off threshold,  $C_T$ , is calculated as

$$C_T = 10^{-\lfloor c_1 - c_2(1 - g(\sigma)) \rfloor}$$
 (E.39)

where  $c_1 = 10.5$  and  $c_2 = 3.5$  are model constants suggested in Ref. [60], and  $g(\cdot)$  is a nonlinear mapping defined as

$$g(\sigma) = (1 - \sigma)^4 (1 + 4\sigma)$$
 (E.40)

#### E.3. Characteristic decomposition on curvilinear meshes and approximate Riemann solver

The use of nonlinear interpolation schemes is combined with the characteristic decomposition for a linearized decoupled system. Considering the inviscid fluxes only, the Navier-Stokes system reduces to an Euler system as follows.

$$\frac{\partial JW}{\partial t} + \frac{\partial \hat{F}_{\xi}}{\partial \xi} + \frac{\partial \hat{F}_{\eta}}{\partial \eta} + \frac{\partial \hat{F}_{\zeta}}{\partial \zeta} = \mathbf{0}$$
(E.41)

where W is the vector of conservative variables, and  $\hat{F}_{\xi}$ ,  $\hat{F}_{\eta}$ , and  $\hat{F}_{\zeta}$  are the vectors of inviscid contravariant fluxes in  $\xi$ ,  $\eta$ , and  $\zeta$  directions respectively. The expressions for W,  $\hat{F}_{\xi}$ ,  $\hat{F}_{\eta}$ , and  $\hat{F}_{\zeta}$  are given as

$$\boldsymbol{W} = \begin{pmatrix} \rho \\ \rho u \\ \rho v \\ \rho w \\ \rho e \end{pmatrix} \quad \hat{\boldsymbol{F}}_{\boldsymbol{\xi}} = \begin{pmatrix} \rho \widehat{\boldsymbol{U}}_{\boldsymbol{\xi}} \\ \rho u \widehat{\boldsymbol{U}}_{\boldsymbol{\xi}} + p \widetilde{\boldsymbol{g}}_{\boldsymbol{x}\boldsymbol{\xi}}^{\mathrm{T}} \\ \rho v \widehat{\boldsymbol{U}}_{\boldsymbol{\xi}} + p \widetilde{\boldsymbol{g}}_{\boldsymbol{x}\boldsymbol{\xi}}^{\mathrm{T}} \\ \rho w \widehat{\boldsymbol{U}}_{\boldsymbol{\xi}} + p \widetilde{\boldsymbol{g}}_{\boldsymbol{x}\boldsymbol{\xi}}^{\mathrm{T}} \\ \rho w \widehat{\boldsymbol{U}}_{\boldsymbol{\xi}} + p \widetilde{\boldsymbol{g}}_{\boldsymbol{x}\boldsymbol{\xi}}^{\mathrm{T}} \\ \rho w \widehat{\boldsymbol{U}}_{\boldsymbol{\xi}} + p \widetilde{\boldsymbol{g}}_{\boldsymbol{x}\boldsymbol{\xi}}^{\mathrm{T}} \\ \rho h \widehat{\boldsymbol{U}}_{\boldsymbol{\xi}} \end{pmatrix} \quad \hat{\boldsymbol{F}}_{\boldsymbol{\eta}} = \begin{pmatrix} \rho \widehat{\boldsymbol{U}}_{\boldsymbol{\eta}} \\ \rho u \widehat{\boldsymbol{U}}_{\boldsymbol{\eta}} + p \widetilde{\boldsymbol{g}}_{\boldsymbol{x}\boldsymbol{\eta}}^{\mathrm{T}} \\ \rho w \widehat{\boldsymbol{U}}_{\boldsymbol{\eta}} + p \widetilde{\boldsymbol{g}}_{\boldsymbol{x}\boldsymbol{\eta}}^{\mathrm{T}} \\ \rho w \widehat{\boldsymbol{U}}_{\boldsymbol{\eta}} + p \widetilde{\boldsymbol{g}}_{\boldsymbol{x}\boldsymbol{\eta}}^{\mathrm{T}} \\ \rho h \widehat{\boldsymbol{U}}_{\boldsymbol{\eta}} \end{pmatrix} \quad \hat{\boldsymbol{F}}_{\boldsymbol{\zeta}} = \begin{pmatrix} \rho \widehat{\boldsymbol{U}}_{\boldsymbol{\zeta}} \\ \rho u \widehat{\boldsymbol{U}}_{\boldsymbol{\zeta}} + p \widetilde{\boldsymbol{g}}_{\boldsymbol{x}\boldsymbol{\zeta}}^{\mathrm{T}} \\ \rho w \widehat{\boldsymbol{U}}_{\boldsymbol{\zeta}} + p \widetilde{\boldsymbol{g}}_{\boldsymbol{x}\boldsymbol{\zeta}}^{\mathrm{T}} \\ \rho h \widehat{\boldsymbol{U}}_{\boldsymbol{\zeta}} \end{pmatrix}$$

where the components in vector and tensor quantities are explicitly expressed as individual quantities, and the matrix-vector notation denotes the Euler equation system. u, v, and w are the three-components of the velocity vector in physical space in the x-, y-, and z-directions respectively. Other notation is consistent with that defined in Sec. 3.1 and Sec. 3.3.

The characteristic decomposition of the contravariant flux Jacobian in the  $\xi$ -dimension can be denoted as

$$\frac{\partial \hat{F}_{\xi}}{\partial \mathbf{W}} = \mathbf{R}_{\xi} \Lambda_{\xi} \mathbf{L}_{\xi}^{\mathrm{T}} \tag{E.42}$$

where  $\Lambda_{\xi}$  is a diagonal matrix storing the eigenvalues, and the columns in  $R_{\xi}$  and  $L_{\xi}$  are the right and left eigenvectors respectively associated with the eigenvalues stored in  $\Lambda_{\xi}$ . A form of characteristic decomposition is provided as follows.

$$\mathbf{R}_{\xi} = \begin{pmatrix}
1 & 0 & 1 & 0 & 1 \\
u - c\overline{g}_{x\xi}^{T} & \overline{l}_{x\xi} & u & \overline{m}_{x\xi} & u + c\overline{g}_{x\xi}^{T} \\
v - c\overline{g}_{y\xi}^{T} & \overline{l}_{y\xi} & v & \overline{m}_{y\xi} & v + c\overline{g}_{y\xi}^{T} \\
w - c\overline{g}_{z\xi}^{T} & \overline{l}_{z\xi} & w & \overline{m}_{z\xi} & w + c\overline{g}_{z\xi}^{T} \\
h - c\overline{U}_{\xi} & \overline{U}_{I(\xi)} & e_{k} & \overline{U}_{m(\xi)} & h + c\overline{U}_{\xi}
\end{pmatrix}$$
(E.43)

$$\Lambda_{\xi} = \begin{pmatrix}
\hat{U}_{\xi} - c\tilde{g}_{n\xi}^{T} & 0 & 0 & 0 & 0 \\
0 & \hat{U}_{\xi} & 0 & 0 & 0 \\
0 & 0 & \hat{U}_{\xi} & 0 & 0 & 0 \\
0 & 0 & 0 & \hat{U}_{\xi} & 0 & 0 \\
0 & 0 & 0 & \hat{U}_{\xi} & 0 & 0 \\
0 & 0 & 0 & 0 & \hat{U}_{\xi} + c\tilde{g}_{n\xi}^{T}
\end{pmatrix}$$
(E.44)

$$L_{\xi}^{T} = \begin{pmatrix} \frac{\gamma - 1}{2c^{2}} e_{k} + \frac{\overline{U}_{\xi}}{2c} & -\frac{\overline{g}_{x\xi}^{T}}{2c} - \frac{\gamma - 1}{2c^{2}} u & -\frac{\overline{g}_{y\xi}^{T}}{2c} - \frac{\gamma - 1}{2c^{2}} v & -\frac{\overline{g}_{z\xi}^{T}}{2c} - \frac{\gamma - 1}{2c^{2}} w & \frac{\gamma - 1}{2c^{2}} \\ -\overline{U}_{I(\xi)} & \overline{I}_{x\xi} & \overline{I}_{y\xi} & \overline{I}_{z\xi} & 0 \\ 1 - \frac{\gamma - 1}{c^{2}} e_{k} & \frac{\gamma - 1}{c^{2}} u & \frac{\gamma - 1}{c^{2}} v & \frac{\gamma - 1}{c^{2}} w & -\frac{\gamma - 1}{c^{2}} \\ -\overline{U}_{m(\xi)} & \overline{m}_{x\xi} & \overline{m}_{y\xi} & \overline{m}_{z\xi} & 0 \\ \frac{\gamma - 1}{2c^{2}} e_{k} - \frac{\overline{U}_{\xi}}{2c} & \frac{\overline{g}_{x\xi}^{T}}{2c} - \frac{\gamma - 1}{2c^{2}} u & \frac{\overline{g}_{x\xi}^{T}}{2c} - \frac{\gamma - 1}{2c^{2}} v & \frac{\overline{g}_{z\xi}^{T}}{2c} - \frac{\gamma - 1}{2c^{2}} w & \frac{\gamma - 1}{2c^{2}} \end{pmatrix}$$

$$(E.45)$$

where  $\widetilde{g}_{n\xi}^{\mathrm{T}} = \sqrt{\left(\widetilde{g}_{x\xi}^{\mathrm{T}}\right)^2 + \left(\widetilde{g}_{y\xi}^{\mathrm{T}}\right)^2 + \left(\widetilde{g}_{z\xi}^{\mathrm{T}}\right)^2}$  is the magnitude of the metrics in  $\xi$  dimension.  $\overline{g}_{x\xi}^{\mathrm{T}}$ ,  $\overline{g}_{y\xi}^{\mathrm{T}}$ , and  $\overline{g}_{z\xi}^{\mathrm{T}}$  are the normalized metric components defined as  $\overline{g}_{x\xi}^{\mathrm{T}} = \widetilde{g}_{x\xi}^{\mathrm{T}}/\widetilde{g}_{n\xi}^{\mathrm{T}}$ ,  $\overline{g}_{y\xi}^{\mathrm{T}} = \widetilde{g}_{y\xi}^{\mathrm{T}}/\widetilde{g}_{n\xi}^{\mathrm{T}}$ , and  $\overline{g}_{z\xi}^{\mathrm{T}} = \widetilde{g}_{z\xi}^{\mathrm{T}}/\widetilde{g}_{n\xi}^{\mathrm{T}}$ , and  $\overline{g}_{z\xi}^{\mathrm{T}} = \widetilde{g}_{z\xi}^{\mathrm{T}}/\widetilde{g}_{n\xi}^{\mathrm{T}}$ ,  $\overline{g}_{z\xi}^{\mathrm{T}} = \widetilde{g}_{z\xi}^{\mathrm{T}}/\widetilde{g}_{n\xi}^{\mathrm{T}}$ , and  $\overline{g}_{z\xi}^{\mathrm{T}} = \widetilde{g}_{z\xi}^{\mathrm{T}}/\widetilde{g}_{n\xi}^{\mathrm{T}}$ ,  $\overline{g}_{z\xi}^{\mathrm{T}} = \widetilde{g}_{z\xi}^{\mathrm{T}}/\widetilde{g}_{n\xi}^{\mathrm{T}}$ , and  $\overline{g}_{z\xi}^{\mathrm{T}} = \widetilde{g}_{z\xi}^{\mathrm{T}}/\widetilde{g}_{n\xi}^{\mathrm{T}}$ ,  $\overline{g}_{z\xi}^{\mathrm{T}} = \widetilde{g}_{z\xi}^{\mathrm{T}}/\widetilde{g}_{n\xi}^{\mathrm{T}}$ , and  $\overline{g}_{z\xi}^{\mathrm{T}} = \widetilde{g}_{z\xi}^{\mathrm{T}}/\widetilde{g}_{n\xi}^{\mathrm{T}}$ ,  $\overline{g}_{z\xi}^{\mathrm{T}} = \widetilde{g}_{z\xi}^{\mathrm{T}}/\widetilde{g}_{z\xi}^{\mathrm{T}}$  are two unit vectors that form a set of orthonormal basis vectors in three-dimensional physical space together with  $[\overline{g}_{x\xi}^{\mathrm{T}}, \overline{g}_{z\xi}^{\mathrm{T}}, \overline{g}_{z\xi}^{\mathrm{T}}]^{\mathrm{T}}$ .  $e_{k} = (u^2 + v^2 + w^2)/2$  is the specific kinetic energy.  $\overline{U}_{\xi}$ ,  $\overline{U}_{I(\xi)}$ , and  $\overline{U}_{m(\xi)}$  are defined as  $\overline{U}_{\xi} = u\overline{g}_{x\xi}^{\mathrm{T}} + v\overline{g}_{y\xi}^{\mathrm{T}} + w\overline{g}_{z\xi}^{\mathrm{T}}$ ,  $\overline{U}_{I(\xi)} = u\overline{u}_{x\xi} + v\overline{u}_{z\xi}$ , and  $\overline{U}_{m(\xi)} = u\overline{u}_{x\xi} + v\overline{u}_{z\xi}$  respectively. Due to the symmetry of the contravariant flux formulations in different dimensions in the reference domain, the characteristic decompositions in  $\eta$ - and  $\zeta$ -dimensions are not provided.

During the numerical solution process, the Euler system is locally linearized in each dimension so that the flux Jacobian is frozen within an interpolation stencil. Based on this assumption, the characteristic variables within a stencil can be calculated as

$$Q_{\xi} = \left\langle L_{\xi}^{\mathrm{T}} \right\rangle W \tag{E.46}$$

where  $Q_{\xi}$  is the vector of characteristic variables in the locally linearized Euler system in the  $\xi$ -dimension, and the operator  $\langle (\cdot) \rangle$  denotes that the quantity remains constant within a stencil. The nonlinear shock-capturing schemes will be applied to interpolate Q to the edge-point using a stencil of nodal points. The nonlinear interpolation scheme is not statically symmetric about the stencil, providing upwind-biased numerical dissipation in the non-smooth region. For shock-capturing, the nonlinear interpolation needs to

be applied using both backward-biased and forward-biased stencils to obtain the characteristic variables that are potentially carried by the "right-" traveling waves,  $Q_{\xi}^+$ , interpolated from the "left" side (which is commonly denoted by "L") and the "left-" traveling waves,  $Q_{\xi}^-$ , interpolated from the "right" side (which is commonly denoted by "R") respectively. After interpolation, the characteristic variables obtained on the edge-point are converted back to the conservative variables using the right eigenvectors.

$$\boldsymbol{W}_{\varepsilon}^{+} = \langle \boldsymbol{R}_{\xi} \rangle \boldsymbol{Q}_{\varepsilon}^{+} \text{ and } \boldsymbol{W}_{\varepsilon}^{-} = \langle \boldsymbol{R}_{\xi} \rangle \boldsymbol{Q}_{\varepsilon}^{-}$$
 (E.47, E.48)

where  $W_{\xi}^{+}$  and  $W_{\xi}^{-}$  are the volume weighted conservative variables converted from the interpolated characteristic variables,  $Q_{\xi}^{+}$  and  $Q_{\xi}^{-}$ . In this work, the elements in the locally averaged eigenvectors,  $\langle L_{\xi}^{\rm T} \rangle$  and  $\langle R_{\xi} \rangle$ , are assembled by the Roe-Pike averaged quantities [79,80] which are calculated using the first nodal values on both sides of each targeted edge-point location.

With  $W_{\varepsilon}^{+}$  and  $W_{\varepsilon}^{-}$  obtained, the approximate Riemann flux can be calculated. In this work, the Rusanov flux [61,55] is used.

$$\widehat{\boldsymbol{F}}_{\xi}^{\text{Riemann}} = \frac{1}{2} \left( \widehat{\boldsymbol{F}}_{\xi}^{-} + \widehat{\boldsymbol{F}}_{\xi}^{+} \right) - \frac{1}{2} S \left( \boldsymbol{W}_{\xi}^{-} - \boldsymbol{W}_{\xi}^{+} \right)$$
(E.49)

where  $\hat{F}_{\xi}^{\text{Riemann}}$  is the Rusanov type of approximate Riemann flux,  $\hat{F}_{\xi}^{-}$  and  $\hat{F}_{\xi}^{+}$  are the contravariant fluxes assembled by  $W_{\xi}^{-}$  and  $W_{\xi}^{+}$  respectively, and S is an approximate wave speed calculated as

$$S = \max\left\{ \left| \hat{U}_{\xi}^{+} \right| + c_{\xi}^{+} \widetilde{g}_{n\xi}^{\mathrm{T}}, \left| \hat{U}_{\xi}^{-} \right| + c_{\xi}^{-} \widetilde{g}_{n\xi}^{\mathrm{T}} \right\}$$
 (E.50)

where  $c_{\xi}^+$  and  $c_{\xi}^-$  are the speeds of sound calculated using  $\boldsymbol{W}_{\xi}^+$  and  $\boldsymbol{W}_{\xi}^-$  respectively. For hybrid central-Riemann flux assembly, the hybridization is applied in constructing the primitive variables after the calculation of  $\boldsymbol{W}_{\xi}^+$  and  $\boldsymbol{W}_{\xi}^-$ , and the volume weighted conservative variables and contravariant fluxes are calculated using blended primitive variables. If only primitive variables that are interpolated using central compact schemes are used,  $\boldsymbol{W}_{\xi}^+ = \boldsymbol{W}_{\xi}^-$  and  $\hat{\boldsymbol{F}}_{\xi}^+ = \hat{\boldsymbol{F}}_{\xi}^-$ . In this scenario,  $\hat{\boldsymbol{F}}_{\xi}^{\rm Riemann}$  is same as the central flux.

#### References

- [1] D.J. Bodony, S.K. Lele, On using large-eddy simulation for the prediction of noise from cold and heated turbulent jets, Phys. Fluids 17 (8) (2005) 085103.
- [2] T. Suzuki, S.K. Lele, Shock leakage through an unsteady vortex-laden mixing layer: application to jet screech, J. Fluid Mech. 490 (2003) 139-167.
- [3] S. Lee, S.K. Lele, P. Moin, Eddy shocklets in decaying compressible turbulence, Phys. Fluids A, Fluid Dyn. 3 (4) (1991) 657-664.
- [4] H. Foysi, S. Sarkar, R. Friedrich, Compressibility effects and turbulence scalings in supersonic channel flow, J. Fluid Mech. 509 (2004) 207-216.
- [5] D. Modesti, S. Pirozzoli, Reynolds and Mach number effects in compressible turbulent channel flow, Int. J. Heat Fluid Flow 59 (2016) 33-49.
- [6] A.N. Kolmogorov, The local structure of turbulence in incompressible viscous fluid for very large Reynolds numbers, C. R. Acad. Sci. URSS 30 (1941) 301–305.
- [7] P.-K. Yeung, S.B. Pope, Lagrangian statistics from direct numerical simulations of isotropic turbulence, J. Fluid Mech. 207 (1989) 531–586.
- [8] S. Jagannathan, D.A. Donzis, Reynolds and Mach number scaling in solenoidally-forced compressible turbulence using high-resolution direct numerical simulations, J. Fluid Mech. 789 (2016) 669–707.
- [9] M. Yu, C.-X. Xu, S. Pirozzoli, Genuine compressibility effects in wall-bounded turbulence, Phys. Rev. Fluids 4 (12) (2019) 123402.
- [10] S. Pirozzoli, P. Orlandi, Natural grid stretching for DNS of wall-bounded flows, J. Comput. Phys. 439 (2021) 110408.
- [11] A. Ceci, S. Pirozzoli, Natural grid stretching for DNS of compressible wall-bounded flows, J. Comput. Phys. X 17 (2023) 100128.
- [12] J. Smagorinsky, General circulation experiments with the primitive equations: I. The basic experiment, Mon. Weather Rev. 91 (3) (1963) 99-164.
- [13] P. Moin, K. Squires, W. Cabot, S. Lee, A dynamic subgrid-scale model for compressible turbulence and scalar transport, Phys. Fluids A, Fluid Dyn. 3 (11) (1991) 2746–2757.
- [14] A. Vreman, An eddy-viscosity subgrid-scale model for turbulent shear flow: algebraic theory and applications, Phys. Fluids 16 (10) (2004) 3670-3681.
- [15] F. Nicoud, H.B. Toda, O. Cabrit, S. Bose, J. Lee, Using singular values to build a subgrid-scale model for large eddy simulations, Phys. Fluids 23 (8) (2011) 085106.
- [16] J. Boussinesq, Essai sur la théorie des eaux courantes, in: Mémoires Présentés par Divers Savants à l'Académie des Sciences, 1877, pp. 1–680.
- [17] M.Y. Hussaini, T.A. Zang, Spectral methods in fluid dynamics, Annu. Rev. Fluid Mech. 19 (1) (1987) 339-367.
- [18] S.A. Orszag, Comparison of pseudospectral and spectral approximation, Stud. Appl. Math. 51 (3) (1972) 253–259.
- [19] S.K. Lele, Compact finite difference schemes with spectral-like resolution, J. Comput. Phys. 103 (1) (1992) 16–42
- [20] S. Laizet, E. Lamballais, High-order compact schemes for incompressible flows: a simple and efficient method with quasi-spectral accuracy, J. Comput. Phys. 228 (16) (2009) 5989–6015.
- [21] A.S. Ghate, S.K. Lele, Subfilter-scale enrichment of planetary boundary layer large eddy simulation using discrete Fourier-Gabor modes, J. Fluid Mech. 819 (2017) 494-539.
- [22] D.P. Rizzetta, M.R. Visbal, P.E. Morgan, A high-order compact finite-difference scheme for large-eddy simulation of active flow control, Prog. Aerosp. Sci. 44 (6) (2008) 397–426.
- [23] T. Colonius, S.K. Lele, P. Moin, Sound generation in a mixing layer, J. Fluid Mech. 330 (1997) 375-409.
- [24] N.S. Ghaisas, A. Subramaniam, S.K. Lele, A unified high-order Eulerian method for continuum simulations of fluid flow and of elastic-plastic deformations in solids, J. Comput. Phys. 371 (2018) 452–482.
- [25] J. Shang, High-order compact-difference schemes for time-dependent Maxwell equations, J. Comput. Phys. 153 (2) (1999) 312-333.
- [26] A. Kravchenko, P. Moin, On the effect of numerical errors in large eddy simulations of turbulent flows, J. Comput. Phys. 131 (2) (1997) 310-322.
- [27] G.A. Blaisdell, Numerical simulation of compressible homogeneous turbulence, Ph.D. thesis, Stanford University, 1991.
- [28] G. Blaisdell, E. Spyropoulos, J. Qin, The effect of the formulation of nonlinear terms on aliasing errors in spectral methods, Appl. Numer. Math. 21 (3) (1996) 207–219.
- [29] F. Ducros, F. Laporte, T. Soulères, V. Guinot, P. Moinat, B. Caruelle, High-order fluxes for conservative skew-symmetric-like schemes in structured meshes: application to compressible flows, J. Comput. Phys. 161 (1) (2000) 114–139.
- [30] S. Pirozzoli, Stabilized non-dissipative approximations of Euler equations in generalized curvilinear coordinates, J. Comput. Phys. 230 (8) (2011) 2997–3014.
- [31] J. Brouwer, J. Reiss, J. Sesterhenn, Conservative time integrators of arbitrary order for skew-symmetric finite-difference discretizations of compressible flow, Comput. Fluids 100 (2014) 1–12.
- [32] S. Pirozzoli, Numerical methods for high-speed flows, Annu. Rev. Fluid Mech. 43 (1) (2011) 163–194.

- [33] G. Patterson Jr, S.A. Orszag, Spectral calculations of isotropic turbulence: efficient removal of aliasing interactions, Phys. Fluids 14 (11) (1971) 2538-2541.
- [34] S.A. Orszag, On the elimination of aliasing in finite-difference schemes by filtering high-wavenumber components, J. Atmos. Sci. 28 (6) (1971) 1074.
- [35] C. Lui, S. Lele, Direct numerical simulation of spatially developing, compressible, turbulent mixing layers, in: 39th Aerospace Sciences Meeting and Exhibit, 2001. p. 291.
- [36] V.M. Deshpande, R. Bhattacharya, D.A. Donzis, A unified framework to generate optimized compact finite difference schemes, J. Comput. Phys. 432 (2021) 110157.
- [37] S. Kawai, S.K. Shankar, S.K. Lele, Assessment of localized artificial diffusivity scheme for large-eddy simulation of compressible turbulent flows, J. Comput. Phys. 229 (5) (2010) 1739–1762.
- [38] S.T. Bose, P. Moin, D. You, Grid-independent large-eddy simulation using explicit filtering, Phys. Fluids 22 (10) (2010) 105103.
- [39] A.W. Cook, Artificial fluid properties for large-eddy simulation of compressible turbulent mixing, Phys. Fluids 19 (5) (2007) 055103.
- [40] E. Johnsen, J. Larsson, A.V. Bhagatwala, W.H. Cabot, P. Moin, B.J. Olson, P.S. Rawat, S.K. Shankar, B. Sjögreen, H.C. Yee, et al., Assessment of high-resolution methods for numerical simulations of compressible turbulence with shock waves, J. Comput. Phys. 229 (4) (2010) 1213–1237.
- [41] F.H. Harlow, J.E. Welch, Numerical calculation of time-dependent viscous incompressible flow of fluid with free surface, Phys. Fluids 8 (12) (1965) 2182-2189.
- [42] S. Patankar, D. Spalding, A calculation procedure for heat, mass and momentum transfer in three-dimensional parabolic flows, Int. J. Heat Mass Transf. 15 (10) (1972) 1787–1806.
- [43] S. Nagarajan, S.K. Lele, J.H. Ferziger, A robust high-order compact method for large eddy simulation, J. Comput. Phys. 191 (2) (2003) 392-419.
- [44] T. Pulliam, J. Steger, On implicit finite-difference simulations of three-dimensional flow, in: 16th Aerospace Sciences Meeting, 1978, p. 10.
- [45] P. Thomas, C. Lombard, Geometric conservation law and its application to flow computations on moving grids, AIAA J. 17 (10) (1979) 1030-1037.
- [46] M.R. Visbal, D.V. Gaitonde, On the use of higher-order finite-difference schemes on curvilinear and deforming meshes, J. Comput. Phys. 181 (1) (2002) 155-185.
- [47] T. Nonomura, N. Iizuka, K. Fujii, Freestream and vortex preservation properties of high-order WENO and WCNS on curvilinear grids, Comput. Fluids 39 (2) (2010) 197–214.
- [48] H. Song, K.V. Matsuno, J.R. West, A. Subramaniam, A.S. Ghate, S.K. Lele, Scalable parallel linear solver for compact banded systems on heterogeneous architectures, J. Comput. Phys. 468 (2022) 111443.
- [49] N. Mansour, P. Moin, W. Reynolds, J. Ferziger, Improved methods for large eddy simulations of turbulence, in: Turbulent Shear Flows I: Selected Papers from the First International Symposium on Turbulent Shear Flows, The Pennsylvania State University, University Park, Pennsylvania, USA, April 18–20, 1977, Springer, 1979, pp. 386–401.
- [50] A. Einstein, Die Grundlage der allgemeinen Relativitätstheorie, in: Das Relativitätsprinzip, Springer, 1923, pp. 81-124.
- [51] G.A. Holzapfel, Nonlinear solid mechanics: a continuum approach for engineering science, Meccanica 37 (4) (2002) 489-490.
- [52] M.R. Visbal, D.V. Gaitonde, High-order-accurate methods for complex unsteady subsonic flows, AIAA J. 37 (10) (1999) 1231–1239.
- [53] Y. Abe, T. Nonomura, N. Iizuka, K. Fujii, Geometric interpretations and spatial symmetry property of metrics in the conservative form for high-order finite-difference schemes on moving and deforming grids, J. Comput. Phys. 260 (2014) 163–203.
- [54] C.-W. Shu, High order weighted essentially nonoscillatory schemes for convection dominated problems, SIAM Rev. 51 (1) (2009) 82-126.
- [55] E.F. Toro, Riemann Solvers and Numerical Methods for Fluid Dynamics: a Practical Introduction, Springer Science & Business Media, 2013.
- [56] S. Kawai, S.K. Lele, Localized artificial diffusivity scheme for discontinuity capturing on curvilinear meshes, J. Comput. Phys. 227 (22) (2008) 9498-9526.
- [57] C.-W. Shu, S. Osher, Efficient implementation of essentially non-oscillatory shock-capturing schemes, J. Comput. Phys. 77 (2) (1988) 439-471.
- [58] V. Eswaran, S.B. Pope, An examination of forcing in direct numerical simulations of turbulence, Comput. Fluids 16 (3) (1988) 257-278.
- [59] R. Liska, B. Wendroff, Comparison of several difference schemes on 1D and 2D test problems for the Euler equations, SIAM J. Sci. Comput. 25 (3) (2003) 995–1017.
- [60] L. Fu, X. Hu, N.A. Adams, A targeted ENO scheme as implicit model for turbulent and genuine subgrid scales, Commun. Comput. Phys. 26 (2) (2019) 311–345.
- [61] V.V. Rusanov, The calculation of the interaction of non-stationary shock waves with barriers, Ž. Vyčisl. Mat. Mat. Fiz. 1 (2) (1961) 267-279.
- [62] T. Von Karman, Progress in the statistical theory of turbulence, Proc. Natl. Acad. Sci. 34 (11) (1948) 530-539.
- [63] G.-S. Jiang, C.-W. Shu, Efficient implementation of weighted ENO schemes, J. Comput. Phys. 126 (1) (1996) 202-228.
- [64] C.E. Shannon, Communication in the presence of noise, Proc. IRE 37 (1) (1949) 10–21.
- [65] P. Moin, R. Verzicco, On the suitability of second-order accurate discretizations for turbulent flow simulations, Eur. J. Mech. B, Fluids 55 (2016) 242-245.
- [66] A. Mani, Analysis and optimization of numerical sponge layers as a nonreflective boundary treatment, J. Comput. Phys. 231 (2) (2012) 704-716.
- [67] A.G. Kravchenko, P. Moin, Numerical studies of flow over a circular cylinder at Re<sub>D</sub> = 3900, Phys. Fluids 12 (2) (2000) 403-417.
- [68] L. Ong, J. Wallace, The velocity field of the turbulent very near wake of a circular cylinder, Exp. Fluids 20 (6) (1996) 441-453.
- [69] V. Murthy, W. Rose, Detailed measurements on a circular cylinder in cross flow, AIAA J. 16 (6) (1978) 549–550.
- [70] L. Lourenco, C. Shin, Characteristics of the plate turbulent near wake of a circular cylinder. A particle image velocimetry study, in: Unpublished, Results Taken from Beaudan and Moin, 1994.
- [71] V. Molochnikov, N. Mikheev, A. Mikheev, A. Paereliy, N. Dushin, O. Dushina, Siv measurements of flow structure in the near wake of a circular cylinder at Re= 3900, Fluid Dyn. Res. 51 (5) (2019) 055505.
- [72] M. Van Dyke, An Album of Fluid Motion, vol. 176, Parabolic Press, Stanford, 1982.
- [73] A. Mani, J. Larsson, P. Moin, Suitability of artificial bulk viscosity for large-eddy simulation of turbulent flows with shocks, J. Comput. Phys. 228 (19) (2009) 7368–7374.
- [74] I. Bermejo-Moreno, J. Larsson, S.K. Lele, LES of canonical shock-turbulence interaction, in: Center for Turbulence Research Annual Research Briefs, 2010, pp. 209–222.
- [75] A. Favre, Turbulence: space-time statistical properties and behavior in supersonic flows, Phys. Fluids 26 (10) (1983) 2851–2863.
- [76] E. Garnier, N. Adams, P. Sagaut, Large Eddy Simulation for Compressible Flows, Springer Science & Business Media, 2009.
- [77] A.W. Cook, W.H. Cabot, A high-wavenumber viscosity for high-resolution numerical methods, J. Comput. Phys. 195 (2) (2004) 594-601.
- [78] L. Fu, X.Y. Hu, N.A. Adams, A family of high-order targeted ENO schemes for compressible-fluid simulations, J. Comput. Phys. 305 (2016) 333–359.
- [79] P. Roe, J. Pike, Efficient construction and utilisation of approximate Riemann solutions, in: Proc. of the Sixth Int'l. Symposium on Computing Methods in Applied Sciences and Engineering, VI, 1985, pp. 499–518.
- [80] P.L. Roe, Characteristic-based schemes for the Euler equations, Annu. Rev. Fluid Mech. 18 (1) (1986) 337–365.